A Pilot Survey for Astronomical Low Frequency Radio Transients

Derek E. Wilson

Thesis submitted to the Faculty of the
Virginia Polytechnic Institute and State University
in partial fulfillment of the requirements for the degree of

Master of Science
in
Electrical Engineering

Dr. Steve Ellingson, Chair
Dr. Gary Brown
Dr. Jeffrey Reed

August 23, 2005
Blacksburg, Virginia

Keywords: astronomical transients, radio astronomy, digital signal processing

A Pilot Survey for Astronomical Low Frequency Radio Transients

Derek Wilson

ABSTRACT

Dispersed low-frequency radio astronomical pulses may result from exploding primordial black holes, gamma ray bursts, supernovae, or mergers of exotic objects, but have not yet been detected. Detection would be of great scientific significance because such events must involve extreme physics. The transient nature of these events makes detection unlikely with traditional instruments due to lack of sensitivity to single pulses and narrow field of view. For this thesis, a low-frequency wide-bandwidth astronomical search instrument has been developed as an alternative approach. This instrument consists of a single dipole which yields all-sky field of view, albeit at reduced sensitivity. The spectrum from 37 - 55 MHz is coherently digitized at 200 million samples per second, recorded, and analyzed off-line for the presence of dispersed pulses. A preliminary survey has been made at a remote site in western North Carolina. In a 20 minute observation, 9 detections greater than 6.5σ occurred, corresponding to pulses of $\leq$ 20 ms duration and dispersion measures (DMs) ranging from 15 to 70 pc cm^{-3} . In addition, groups of pulses were detected ($\sim 5\sigma$) at DMs of 43.1, 52.1, and 52.2 pc cm^{-3} . The possibility of association with known pulsars is considered; however, it is also possible these are due simply to radio frequency interference. Improvements to this instrument and survey technique are suggested.

Acknowledgments

It is of great pleasure that I acknowledge those who have helped me both professionally and personally through these last 6 years at Virginia Tech. First and foremost, I would like to thank my advisor, Dr. Ellingson, for helping me to design, debug, and test an instrument unlike anything I'd ever worked on before. His unimaginable patience with me has helped me to learn more than I ever thought possible in just a year and a half. Also, I greatly appreciate his taking so much time to help me out during this entire process of designing, performing, and writing about this experiment. I know he put forth a considerable amount of effort just helping me to make my deadlines. I also thank him for putting astronomical literature into a perspective that I could understand more easily. Wading through all these papers has been a tough process, and I cannot imagine how it might have been without the help of someone who is so versed in such topics. Thanks to Dr. Brown, who pushed me to actually *understand* electromagnetics, as opposed to learning how to apply a few well-known equations. After five classes and several months of research under his wing, I gained an extraordinary appreciation for the field of EM; never before have I seen someone approach a topic with such enthusiasm. Thanks to Dr. Reed for taking time out of his busy schedule to enthusiastically offer to serve on my committee. Not only did he teach me the ideas behind software radios, but our after-class discussions gave me a whole new appreciation for the field of communication theory. I'm honored to have worked with those who are so renowned in their respective fields. And many thanks to all my professors who have helped to build me up and prepare me for pursuing a rewarding career in electrical engineering.

At PARI, I would like to thank Don Cline and Charles Osborne for their undying support in this project. While there were a number of pitfalls in dealing with remote access to the on-site computer, they were always straightened out quickly and efficiently, thanks to the immediate response by Mr. Osborne. Also, thanks for showing me around such a neat complex. One day I'd like to come back and get on 26 E or W and Smiley! Thanks to the NRL for providing us with the NLTA dipole and preamplifier. Without this support, this experiment would never have happened! Thanks to NASA for their development of the Astrophysics Data System (ADS). Without this extraordinary reference, finding related scientific material in the fields of Astronomy and Physics would have been... inordinate to say the least. (This research has made use of NASA's ADS[1]).

[1] http://www.adsabs.harvard.edu/

I would like to thank Grant Hampson for 'blazing the trail' on the development of support software for the AD9054 evaluation board. Without the great documentation, I'm not sure I ever would have learned how to use the board. The software gave me a jumpstart on relearning 'C' code, saving me countless hours pouring over my old C++ books and internet sites.

Also, I would like to thank a few students for their considerable effort to see me succeed. Tyler, thanks immensely for your support in the analysis of the antenna system. Long days at PARI, interesting car rides, and a well formed friendship... thanks for putting up with me! Thad, thanks for pushing me to learn how to use LaTeX. Without your advice, I would still be using Microsoft Word and equation editor; I cannot imagine having to write this thesis with constant auto-formatting, and non-standard supported files. Thanks for helping me to push through that initial learning curve and really start to get a grip on TeX. Scott, lunch breaks were always a welcomed respite from the grind of the workstation. Our discussions on ham radio, Bob and Tom, and LaTeXwere always enlightening, and there wasn't a day spent in the workstation that you didn't take time to come in and help me clear my head for a few minutes. :)

I would like to thank all my friends for dealing with me over the last several months. I am sure at times I have been a pain to deal with, especially with the amount of stress I have been under. Luke: good music, darts, and late nights at All Good, the Valley Center, hanging around campus, and wherever else we happened to end up - what a ride it has been! Floppy and James: good music, my first introduction to good beer, late nights at the bar playing pool, it's been a lot of fun! John and Gbus, what a great house: late nights watching TV, spinning records, playing pool, Hell's Kitchen, and a newly found love of artwork. To everyone I haven't mentioned: these years in Blacksburg will always hold a special place in my heart - it has been more fun than I ever thought college could be. Thanks, Everyone!

And to my **wonderful** family: Thanks for understanding my sometimes infrequent (or just plain lack of) communication. Your support over the last six years has taught me how to live so I don't have any regrets. I appreciate everything you all have done for me, and without your unending support, I don't know that I would have made it this far. I will never forget to look back on my college years and know that it was during this time I actually learned to create family relationships. Not only have you all always pushed me to work hard, you have never let me lose track of the vision that 'you will never fully appreciate something unless you put your all into it.' Thank you for all the love and kind words that I will never forget. I love you! Grandmother and Grandad: It has been thoroughly enjoyable to live so close and see you as much as I have been able to. Your incredible wisdom has taught me more than I will ever be able to show, and I continually look forward to your stories for years to come! Mom and Mark (and Dice and Sissy): Trips to Southern MD were *always* a welcomed weekend. Early mornings out rockfishing, late nights playing 66 and spades, or just relaxing in the hot tub, thanks for always having something for us to do! Dad and Jennifer (and Roxy): Where do I start...? While trips to Va. Beach may not have been as frequent as you would have liked, I always had great fun when I made it out. Strolls along the boardwalk,

frequent trips to all my favorite restaurants, and enjoyable evenings watching a good movie, thanks for all you have done and all the help you have given me!

Lizzy, these past two years have been divine! Every day you have made me feel more special, and your always increasing love has shown me joys I have never known before. I will always remember our fantastic vacations to NYC (Crobar and Avalon), Las Vegas, Snowshoe, All Good, Nation, Alexandria, Leonardtown, and Virginia Beach, not to mention relaxing weekends spent around the 'burg and Charlottesville or long days spent at Busch Gardens. Thank you for making our time together so exciting and rewarding. *You are the light of my life.* I Love You, Elizabeth!

Contents

List of Figures

List of Tables

Chapter 1

Introduction

1.1 Astronomical Radio Transients

A variety of theorized yet still undetected astronomical phenomena are likely to produce pulses in the low-frequency radio spectrum. In this thesis, we refer to radio transients as pulses with durations at their point of origin of a few seconds or less. These transient pulses are likely to be dispersed due to propagation through the interstellar/intergalactic medium (ISM/IGM). A dispersed pulse is characteristic of a very distant source, as it is known that propagation through the free electrons present in the ISM/IGM causes low frequencies to arrive later in time with respect to high frequencies. If the pulse is also short (milliseconds), then it must be very compact (i.e., on the order of light-milliseconds across). Thus, a detected dispersed transient suggests the sudden release of a very large amount of energy from a compact region, and so these transients imply extreme physics at the point of origin.

For this reason, their discovery and continued detection would be of great importance to current physicists and astronomers. Detection and analysis of such transients could be very useful in revealing the true nature of these objects and could be readily used to probe the characteristics of the intervening ISM/IGM [1]. Possible sources of low-frequency transients include primordial black holes (PBHs) [2], supernovae [3], gamma ray bursts (GRBs) [4], and neutron star/neutron star (NS/NS) or neutron star/black hole (NS/BH) mergers [5]. The study of these objects, their host environments, and the intervening ISM/IGM would be greatly advanced by the discovery of any of their low-frequency emissions. In addition to these progenitors of low-frequency radio emission, there is always the possibility of previously unknown phenomena. One recent example of a serendipitous discovery was made by Hankins, et al. in their detection of 'nano-giant' pulses from the Crab pulsar [6]. After nearly 30 years of observations of the Crab pulsar, this phenomenon remained undiscovered despite being the brightest object in the universe for a few nanoseconds at a time!

Over the last 35 years, many radio transient surveys have been performed. While a handful

of these surveys have discovered new pulsars, radio transient emission due to PBHs, GRBs, and NS/NS or NS/BH merger events has still gone undetected [1]. Despite null results, each search has increased the understanding of what is needed for new surveys while suggesting improvements for future experiments. While each new experiment aims to open up new parameter space, a key factor contributing to the results of past transient surveys may be limited sky coverage. Recent surveys, including this one, seek to address this issue. After all, it would be nice to know what's going on in the 99.99...% of the sky that's not currently being observed!

1.2 A Pilot Survey for Astronomical Radio Transients

For this thesis, an all-sky low-frequency wide-bandwidth astronomical transient search instrument has been developed. Our instrument, the Pisgah Low Frequency Monitor (PLFM), was developed as a comparatively low cost solution which is suitable for a low-frequency transient survey. A dedispersed pulse sensitivity of ~ 1 MJy was achieved, with the ability to resolve pulses as brief as ~ 20 ms, all while continually surveying nearly $\sim \pi$ sr of the sky. Software has been developed and successfully tested for RFI mitigation, dedispersion, and pulse detection, and a pilot survey has been conducted at the Pisgah Astronomical Research Institute (PARI). During a ~ 20 minute observation window on October 23, 2004, 9 dispersed pulses were detected (6 possibly associated with known pulsars), and interesting detections at dispersion measures (DMs) of 43.1, 52.1, and 52.2 pc cm^{-3} have been made.

1.3 Organization of this thesis

Chapter 2 (*Astronomical Radio Transients*) presents astronomical transient theory and discusses past transient searches. We first consider a few classes of objects that could possibly be detected before moving on to consider how each class of objects might generate low frequency transients. After understanding the detection possibilities, we focus on some of the current research efforts relevant to this experiment. In Chapter 3 (*Instrument Design*), a new instrument designed to search for low-frequency transients is described. Chapter 4 (*Data Analysis*) presents the transient search software, in particular the RFI mitigation, dedispersion, and pulse detection algorithms. Chapter 5 (*RFI Threshold Setting, Instrument Stability, and Sensitivity*) then considers the experiment characteristics. We discuss the instrument sensitivity, stability, and RFI characteristics of the observation site. Chapter 6 (*Experimental Results*) presents the details of the observation taken for this experiment. A method is presented which helps examine the results of the dedispersion and pulse detection algorithms, helping us to narrow down the large number of possible detections to just 9 candidate transients. We associate 6 of these dispersed pulses with known pulsars. Interesting detections at DM ~ 43.1 and 52.1 pc cm^{-3} are also presented.

Chapter 2

Astronomical Radio Transients

This chapter presents the current theory and searches pertaining to possible sources of low-frequency transients. Section 2.1 considers the physics of such sources. Section 2.2 then presents current and recent transient search efforts relevant to our experiment while Section 2.3 gives the requirements for such an experiment.

2.1 Possible Sources of Low-Frequency Transients

2.1.1 GRB Prompt Emission and Supernovae

Usov and Katz [4] propose that GRBs may create short duration low frequency RF emission, known as the 'prompt emission', resulting from the interaction of relativistic electrons with quiescent magnetic fields. Most of the energy is thought to occupy from 0.1 to 1 MHz, which would probably be unobservable from terrestrial based sites due to the opacity of the ionosphere below $\sim$ 20 MHz. However, the high-frequency tail may be detectable up to tens of MHz in certain cases.

It has recently been shown that some GRBs may be attributable to supernovae. Supernovae have long been suspected to be a source of low-frequency transient emission [3], and recently Sagiv and Waxman have hypothesized that the resulting shock wave continuously accelerates electrons in the surrounding gas, producing a low-frequency maser emission [7].

2.1.2 Mergers of Exotic Objects

Black holes (BH) and neutron stars (NS) are both the result of a massive dying and collapsing star. A mechanism for the creation of a low-frequency transient emission is the interaction of magnetic fields accompanying the coalescence of neutron star binaries [5].

2.1.3 Primordial Black Holes (PBHs)

Primordial black holes are thought to be a by-product from the Big Bang. Their size is predicted to be anywhere from smaller than the nucleus of an atom to the size of our sun. PBH models predict that they explode after $\sim$ 10 Gyr, and so should be doing so in our present epoch [8]. In 1977, Rees offered theoretical evidence that these explosions could potentially generate radio pulses powerful enough to be detected from anywhere in our Galaxy with a single low-gain antenna [2]. An upper frequency limit implied from his derivation is near 300 MHz, while the lower limit is determined solely by the opacity of the ionosphere at frequencies below about $\sim$ 20 MHz.

2.1.4 Giant Pulses (GPs) from Pulsars

Another potential source of pulsed low-frequency emission is a 'giant pulse' from a pulsar. It is known that pulsars are spinning neutron stars, emitting periodic, extremely broadband electromagnetic pulses. Some pulsars are known to intermittently emit pulses in the radio regime which are orders of magnitude greater than the mean pulse intensity, known as giant pulses. As of 2005, 10 pulsars are known to emit giant pulses: in order of giant pulse initial detection, the Crab pulsar (PSR B0531+21) [9], B1937+21 [10], B1821-24 [11], B0540-69 in the Large Magellanic Cloud[12], B0031-07 [13], B1112+50 [14], J1752+2359 [15], B1957+20 [16], J0218+4232 [16], and J1823-3021A [17].

On average, in one hour of observation time the Crab pulsar will emit a pulse which is 10,000 times stronger than the mean pulse intensity, and no upper limit has yet been set on its strongest pulses [18]. In fact, the Crab pulsar until recently was believed to exhibit the strongest radio transients in the observable universe, with brightness temperatures up to 10^{37} K having been detected at nanosecond resolution [6]. These 'nano-giant' pulses were not discovered until 2003, simply because the possibility of such pulses was not even anticipated. In late 2004, nano-giant pulses from PSR B1937+21 were discovered by Soglasnov, et al. [19], registering brightness temperatures of 5×10^{39} K, the brightest ever observed in the universe. Even though extremely bright, these nano-giant pulses were not detected in conventional observations due to their dispersed, very brief, and non-periodic nature. Ironically, it appears they are easy to detect, but only at high time resolution.

2.2 Recent Radio Transient Searches

Searches for radio transients have been performed intermittently in the past [1]. Here we report on two which are closest to what is attempted in this work. Table 2.1 compares the characteristics of two of the experiments discussed here with that of the PLFM experiment.

2.2.1 Survey for Transient Astronomical Radio Emission (STARE)

Operating in a 4 MHz bandwidth at 611 MHz, Katz, et al. have searched for astronomical radio emission over the Northeastern United States [20]. Consisting of multiple geographically separated sites, the experiment has been in operation since March 1996. As of 2003, 3898 astronomical events have been discovered exceeding 27 kJy, all of which have been attributed to solar radio bursts. At least 173 GRBs have occurred during their observations, and 7 candidate astronomical radio bursts have been detected within ± 1 hr of a GRB; however, these 7 candidate radio counterparts have all been attributed to local radio interference.

2.2.2 Fallbrook Low-Frequency Immediate Response Telescope (FLIRT)

Operating in a 2.2 MHz bandwidth at 74 MHz, Balsano [21] performed a search for prompt emissions coincident with GRBs. A 12 element phased array was designed to quickly respond to notices by NASA's GRB Coordinates Network, which updates an online list of GRBs in real time, by pointing a $7^\circ \times 7^\circ$ antenna beam at the source. The radio emission from a GRB will be delayed in time with respect to higher frequencies (i.e. γ-rays, optical) due to dispersion in the ISM/IGM. Thus, the resulting delay allows sufficient time for FLIRT to turn towards a GRB detected in γ-rays. During his observations, Balsano detected 1 radio transient emission possibly attributed to a prompt emission from GRB980329. The sun and other known astronomical objects were ruled out as the source of the emission. The frequency drift of the pulse indicated an astrophysical source with DM ~ 66 pc cm^{-3} , but *a posteriori* arguments suggest a very small chance of coincidence between the GRB and detected radio emission. On the other hand, the observed emission was spectrally narrowband while a second, longer duration pulse drifted *up* in frequency, unexplainable 'without invoking spectral evolution at the source', indicating a less convincing detection. While the detected transient was eventually ruled out as possibly due to terrestrial interference, it is still a very tantalizing detection.

2.2.3 GRB All-sky Spectrometer Experiment (GASE)

A planned experiment, dubbed GASE, is currently being organized. Very little information is available about the experiment, thought it is known the experiment is being designed to search for the prompt emission coincident with GRBs.

Table 2.1: Comparison of Related Experimental Efforts

	STARE	**FLIRT**	**PLFM**
center frequency (MHz)	611	74	46
bandwidth (MHz)	4	2.2	18
mode	continuum	spectrometer	spectrometer
$\Delta\nu$ (kHz)	4000	400	12
Δt (ms)	125	2	20
T_{sys} (K)	150	7000[1]	627
A_e (m^2)	0.2	650	~ 10
Ω	~ 1.4 sr	$7^\circ \times 7^\circ$	$\sim \pi$ sr
Remarks	3 antennas separated by 100s of km	12 elements phased array (1 element=8 dipoles)	single dipole
	[1] T_{sys} includes all non-astronomical sources of noise including RFI		

2.3 Inferred requirements for transient searches

We now consider the desirable features for further searches specifically for low-frequency dispersed astronomical transients.

2.3.1 Low Frequency and Wide Bandwidth

The frequency range between ~ 30 and ~ 60 MHz is attractive for the following reasons:

- Predictions by Sagiv and Waxman as well as Usov and Katz predict detectable levels from GRB prompt emissions in this frequency range [7, 4], while predictions by Hansen and Lyutikov place the high end of NS/NS and NS/BH merger event radio emissions in this frequency range [5].
- Most known sources of transient emission (e.g. pulsars) exhibit flux densities with ν^α ($\alpha \sim [-3.5, -1.4]$) spectral dependence, turning over in the 30 - 150 MHz range.
- Due to the opacity of the atmosphere, it becomes very difficult to observe from terrestrial based sites at frequencies less than ~ 20 MHz.
- The effective aperture of an antenna is proportional to λ^2, where λ is wavelength, so fewer antennas are required to achieve the same collecting area at lower frequencies.

- International shortwave and amateur radio transmissions cause strong radio frequency interference (RFI) below 30 MHz; whereas, domestic TV broadcast creates strong RFI above 55 MHz.
- Since sensitivity scales with bandwidth, motivation exists for the widest possible bandwidth.

2.3.2 Wide field of view

To date, most transient searches have been performed with very narrow fields of view (FOV), a consequence of very high gain antennas. While the use of large antennas and interferometers add orders of magnitude to sensitivity as well as the ability to localize sources, they are only able to search very small regions of the sky at a time. This is a strong disadvantage as no a priori knowledge of direction is generally available.

2.3.3 Sky-Noise Dominated Observation

An important consideration is that the sensitivity of the antenna and receiver system in this experiment be limited only by the noise of the Galactic background, as opposed to that associated with the system electronics. With total system noise defined as the noise powers resulting from the preamplifier, feedline and receiver, and Galactic noise defined as the sky temperature available at the antenna terminals (see Section 3.2.4 and Appendix A), we wish to ensure that the Galactic noise power spectral density (PSD) is greater than the total system noise PSD over the chosen bandwidth.

2.3.4 Terrestrial Interference Mitigation

A factor which has become steadily worse since the first radio transient searches began is the difficulty in discriminating against radio-frequency interference (RFI). While new methods for mitigation are continually being developed [22], RFI still tends to be the limiting factor in low frequency radio astronomy, thus effective countermeasures are essential.

2.3.5 Dedispersion

Dispersion is a phenomenon in which low frequencies propagate more slowly than high frequencies due to the presence of free electrons in the medium. In radio astronomy, dispersion is commonly quantified in terms of its dispersion measure (DM), which is defined as the

integrated column density of free electrons along the line of sight, i.e.:

$$\mathrm{DM} \equiv \int_0^L n_e(z)\, dz \tag{2.1}$$

and is generally expressed in units of pc cm^{-3} [23] where 1 pc = 3.26 light years. For propagation over relatively short distances, DM$\sim$ 0 pc cm^{-3} . Through the plane of the galaxy, the maximum DM is about 3400 pc cm^{-3} and looking out normal to the plane of the Galaxy, the maximum DM is about 200 pc cm^{-3} [24]. To detect weak pulses with DM$>$ 0, a scheme for dedispersion of the received time series must be developed. Section 4.2 presents this development, and Appendix B presents a complete derivation of dispersion theory.

Chapter 3

Instrument Design

3.1 Introduction

In this chapter, we present the details of the instrument which was designed for this thesis. Section 2.3 presented the requirements for a low-frequency transient search instrument, and here we present the considerations for reaching those requirements. The instrument description is divided into three sections: 1.) The hardware prior to the receiver, (the antenna, preamplifier, and feedline), 2.) The receiver, (consisting of automatic gain control (AGC), an anti-aliasing filter, high-power amplifier, analog-digital converter (ADC), data capture board, and personal computer), and 3.) Supporting software (that necessary to operate the instrument and analyze the data). Figure 3.1 shows the signal path of the instrument.

3.2 Antenna System

3.2.1 Antenna

The purpose of the antenna is to deliver the received Galactic + man-made noise as well as astronomical transient signals to the preamplifier. The antenna is a dipole with a large thickness-length ratio, also known as a 'fat' dipole. Using a fat dipole helps to increase the impedance bandwidth, i.e. the bandwidth over which the terminal impedance is nearly constant [25]. This dipole was donated by the Naval Research Lab (NRL) and is identical to the elements used in the NRL Low-frequency Test Array (NLTA) [26]. Figure 3.2 shows the antenna dimensions and Figure 3.3 shows a picture of the antenna.

One requirement for the antenna was that it have a very broad beamwidth, such that the effective aperture is nearly constant over the entire sky. Let $G = \epsilon_A D$ be the gain of the antenna, where $D = \frac{4\pi}{\Omega}$ is directivity, ϵ_A is efficiency (accounting for the loss due to non-

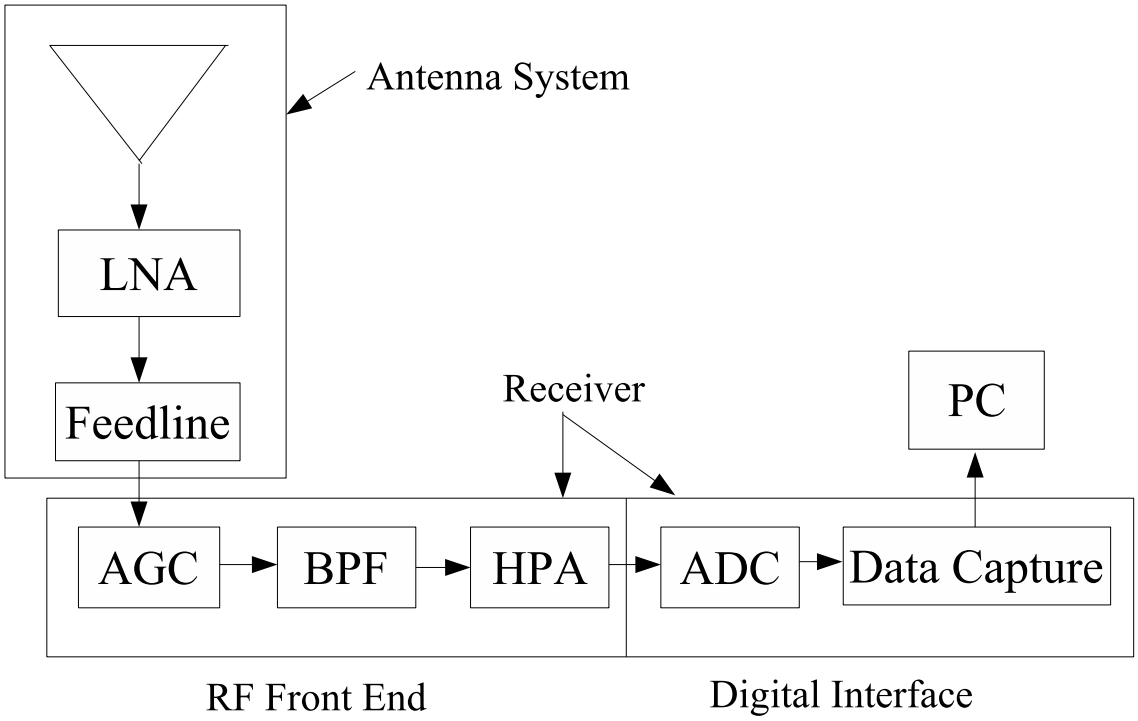

Figure 3.1: Signal Path for the PLFM Instrument

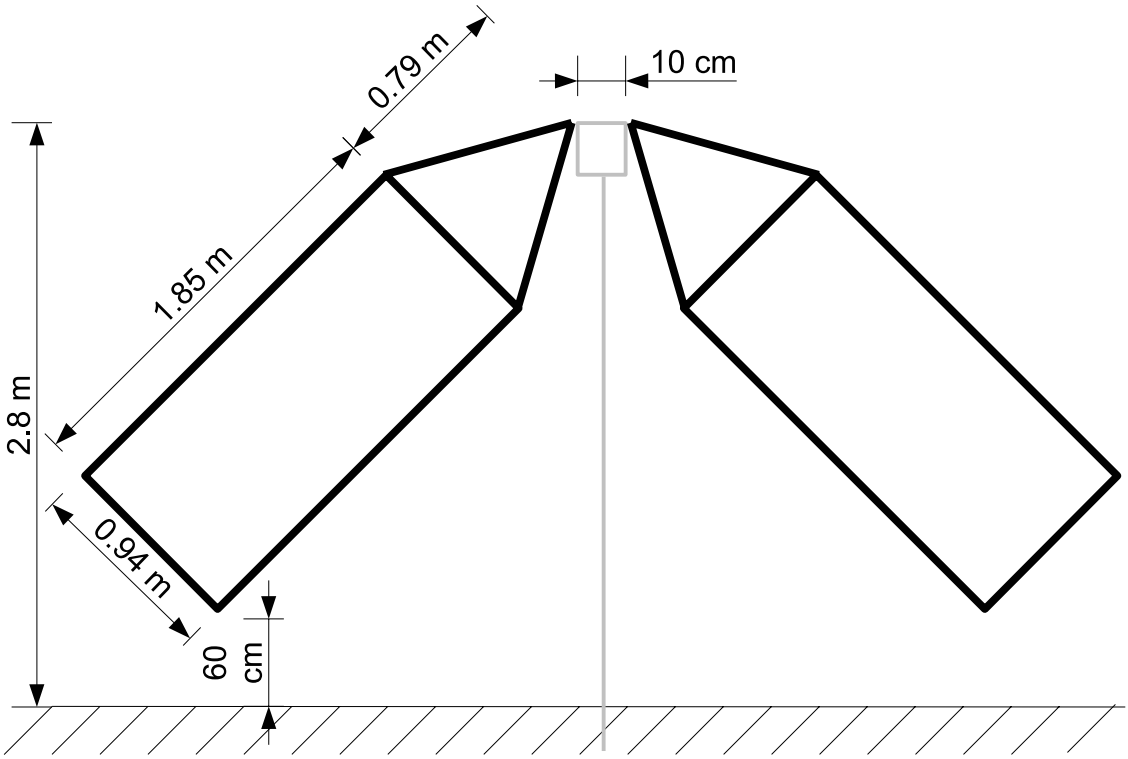

Figure 3.2: The NLTA dipole used in this experiment [27]. Copper tubing is shown in bold.

Figure 3.3: Picture of the dipole used in this experiment.

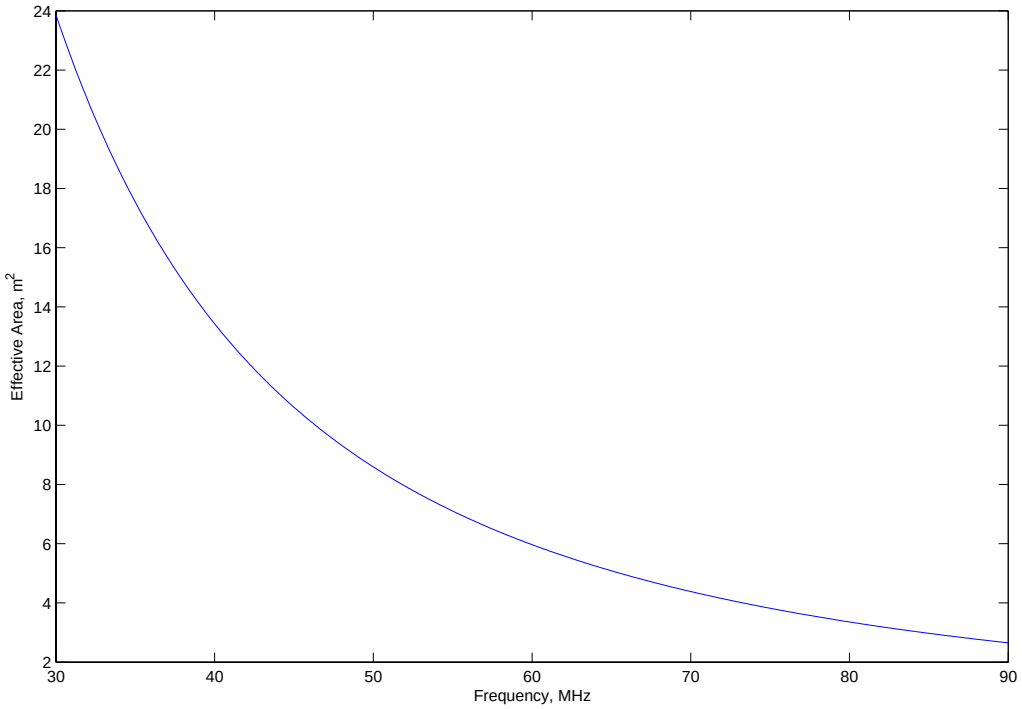

Figure 3.4: Effective Aperture, A_e, for PLFM Antenna

perfectly-conducting copper and ground), and Ω is beam solid angle in steradians. Then we can write

$$A_e = \frac{\lambda^2}{4\pi} \cdot G \tag{3.1}$$

where A_e is effective aperture. Figure 3.4 plots A_e for this antenna, assuming $\Omega \sim \pi$ sr ($D \sim 4$) and $\epsilon_A = 0.75$ due to imperfect lossy ground (Ellingson and Kramer derive $\epsilon_A \sim 0.95$ for realistic earth ground with conductivity $\sigma = 5 \times 10^{-3}$ S/m [28]). A_e is approximately proportional to *cos* θ, where θ is an elevation angle such that $\theta = 0$ is the zenith.

Another requirement of this experiment is a large bandwidth, to improve sensitivity. The antenna impedance over the frequency range of interest is shown in Figure 3.5, obtained from a *NEC-2* based method-of-moments code. Ellingson [27] notes that Galactic noise can easily dominate over the associated electronics of an antenna/receiver system and that the performance of the antenna is degraded beyond usability only if the impedance mismatch between the antenna terminals and subsequent electronics is so large to cause the receiver system to no longer be Galactic noise dominated. Further, once an antenna is Galactic noise-dominated, improving this match does not significantly improve the system sensitivity.

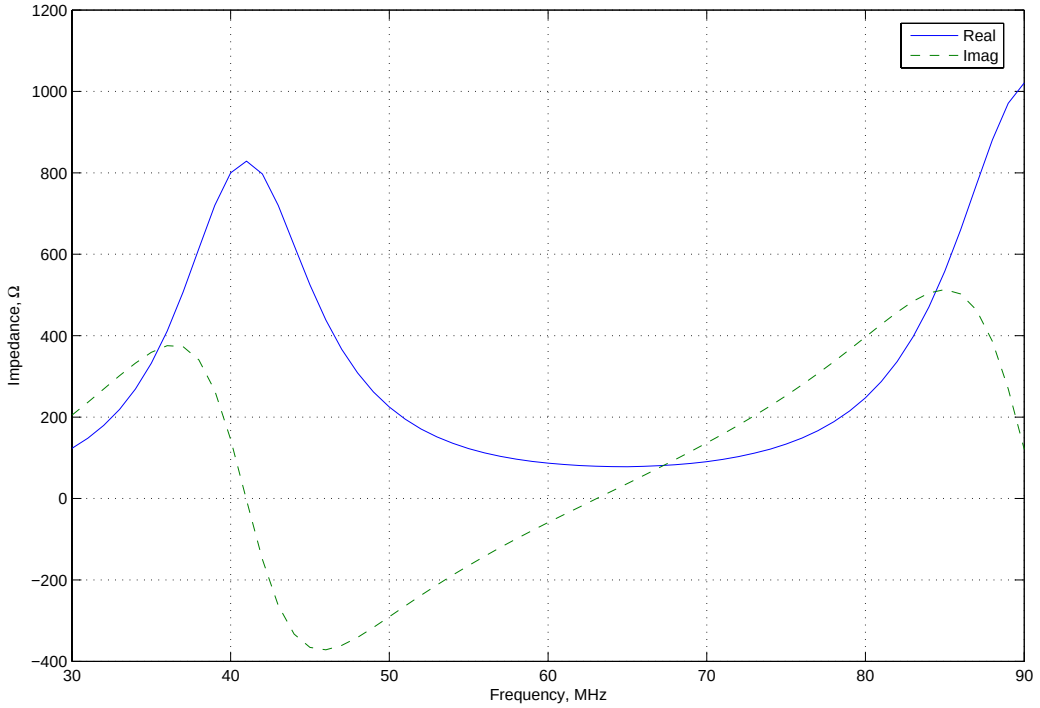

Figure 3.5: Real and imaginary component of the PLFM antenna impedance

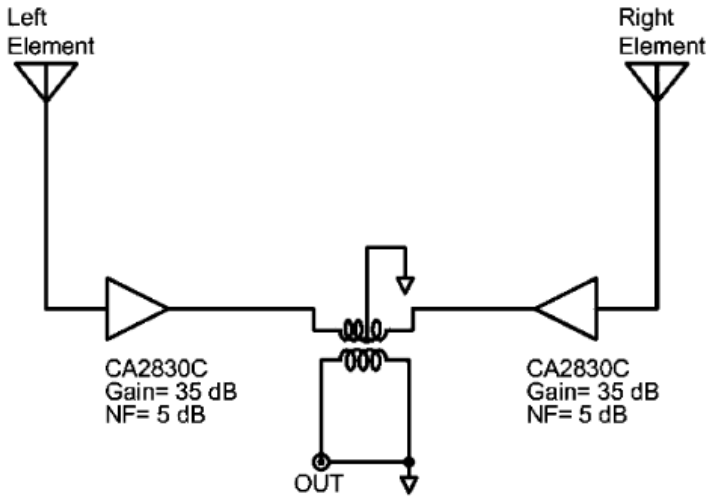

Figure 3.6: Schematic diagram of the preamplifier, taken from [26]. The transformer provides a 2:1 step-down in impedance [26].

3.2.2 Preamplifier

The preamplifier is defined as the instrumentation connected directly to the antenna terminals and its purpose is many fold.

- The preamplifier contributes sufficient gain to set the noise temperature of the system.
- The antenna in this instrument is a balanced dipole; whereas, the feedline is an unbalanced coaxial cable. Our preamplifier acts as a balun.
- As the antenna's terminal impedance varies significantly over its tuning range, the preamplifier acts as an impedance buffer from the feedline. This helps to reduce standing waves on the feedline, mitigating undesired spectral ripple.

The preamplifier was also donated by the NRL and is the same design used in the NLTA [26]. It consists of a pair of Motorola CA2830C wideband linear amplifiers, each connected to one of the dipole arms, with 5 dB noise figures and output third-order intercept points at +46 dBm. Total power consumption by the preamplifier is 24V @ 0.42A $\sim$ 10 W. A schematic is shown in Figure 3.6, taken from [26]. A picture of the preamplifier installed at the antenna terminals is shown in Figure 3.7.

For analysis purposes, it is convenient to describe the preamplifier in terms of its input impedance Z_{pre}, its gain G_{pre}, and its noise figure, F_{pre}. These quantities typically exhibit a frequency dependence; however, this is assumed negligible relative to the effect caused by the variation of the antenna impedance [27]. The nominal impedance of the PLFM preamplifier

Figure 3.7: Picture of preamplifier installed at antenna terminals.

Figure 3.8: Impedance Mismatch Efficiency using $Z_{pre} = 100\Omega$

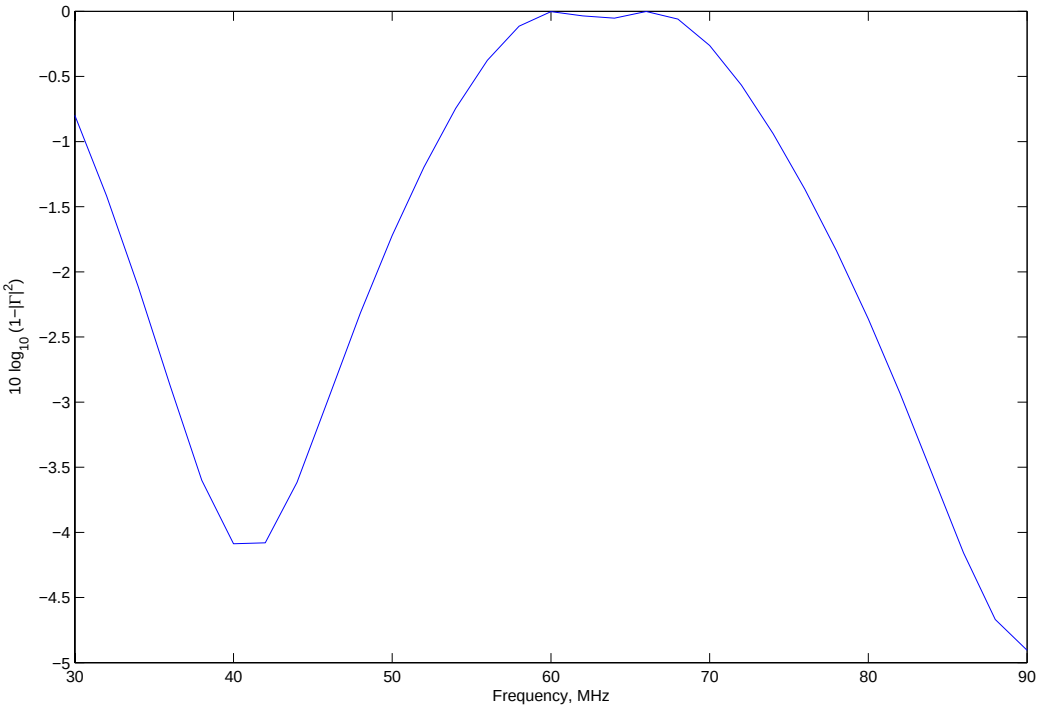

is $Z_{pre} = 100\Omega$, the gain is $G_{pre} = 33$ dB, and the noise figure is $F_{pre} = 5$ dB [26]. From the preamplifier's noise figure, we can determine its noise temperature (3.2).

$$T_{pre} = T_0(F_{pre} - 1) = 627 \text{ K} \tag{3.2}$$

where $T_0 \approx 290$ K is the reference temperature for which F_{pre} is calculated. We find that the power spectral density due to preamplifer noise is $N_{pre} = kT_{pre}G_{pre} \approx -126.8$ dBW/Hz, where $k = 1.3807 \times 10^{-23}$ J K^{-1} is Boltzmann's constant.

As the terminal impedance of the antenna is not matched to that of the preamplifier, there will be less than 100% power transfer to the feedline. The amount of transferred power is quantified by the reflection coefficient between preamplifier and antenna, given by (3.3), and the mismatch efficiency is shown in Figure 3.8.

$$\Gamma = \frac{Z_{pre} - Z_a}{Z_{pre} + Z_a} \tag{3.3}$$

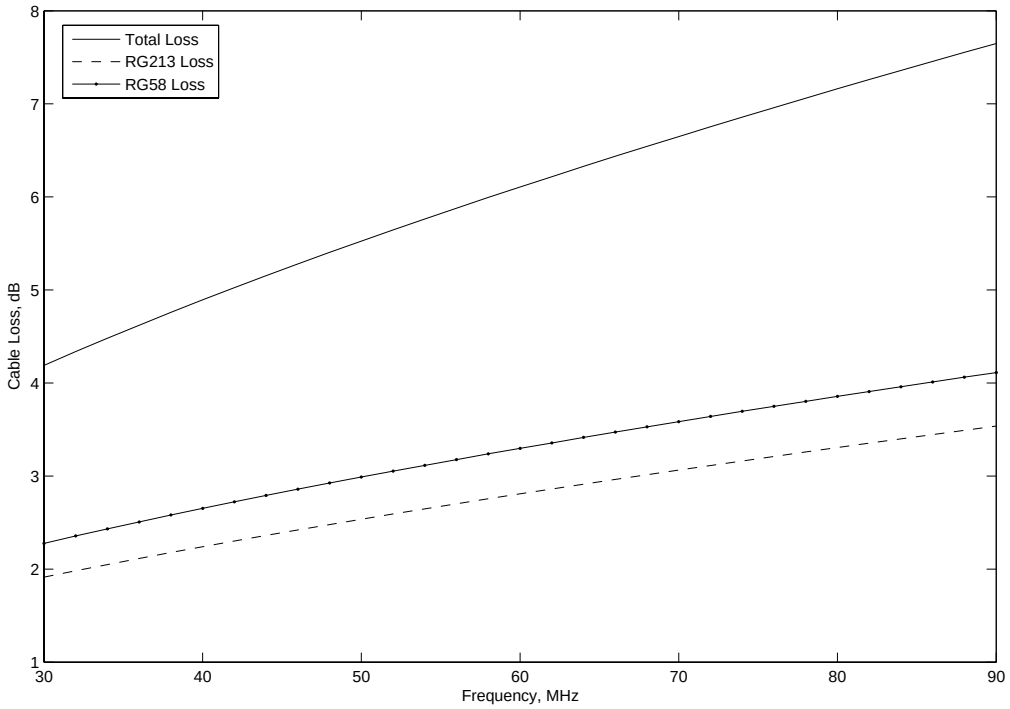

Figure 3.9: Feedline Loss vs. Frequency

3.2.3 Feedline

The antenna is located a short distance away from the building housing the receiver. The feedline connecting the preamplifier to the receiver consists of 62.8 m (206 ft) of RG-213 coaxial cable plus 21.3 m (70 ft) of RG-58 coaxial cable. Total cable losses at 20 MHz are near 4.5 dB increasing to near 7.3 dB at 100 MHz. Figure 3.9 shows cable loss vs. frequency.

The noise associated with the cable loss delivered to the end of the feedline is [27]

$$N_f(\nu) = kT_{phys}\left[1 - G_f(\nu)\right] \tag{3.4}$$

where k is Boltzmann's constant, and G_f corresponds to the feedline *gain*, with $G_f = 1$ corresponding to a lossless line. $T_{phys} \approx 300$ K is the physical temperature of the feedline.

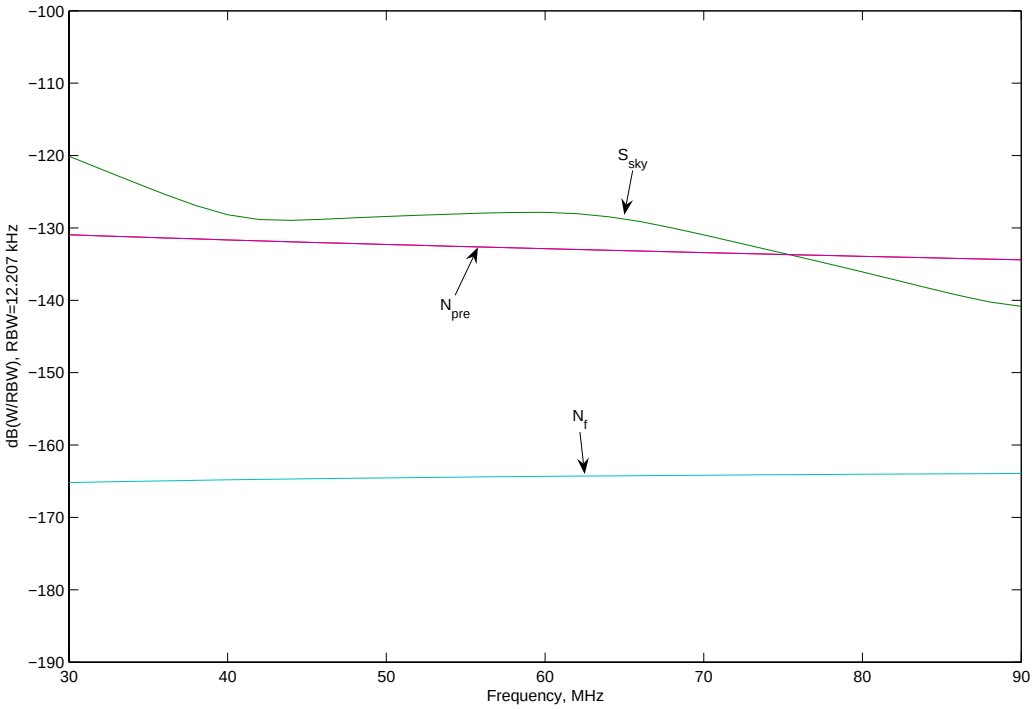

Figure 3.10: Power spectral density of Galactic background and receiver components referenced to feedline output.

3.2.4 Noise Analysis of the Antenna System

At the output of the feedline, the Galactic noise power spectral density is

$$S_{sky} = \epsilon_A k T_{sky}(\nu) G_{pre} G_f \tag{3.5}$$

where T_{sky} is the temperature associated with the Galactic background, ranging from 2.8×10^4 K at 30 MHz to 1×10^3 K at 90 MHz (for details, see Appendix A). The noise power spectral density is $N_{pre} + N_f$ where

$$N_{pre}(\nu) = k T_{pre} G_{pre} G_f(\nu) \ . \tag{3.6}$$

Figure 3.10 shows both the desired Galactic PSD and the undesired noise PSDs due to the feedline and preamplifier. Note that the antenna system is Galactic noise-dominated by at least 4 dB in the range 30 MHz to 70 MHz.

3.3 RF Front End

Now we explain the RF front end, consisting of AGC, an anti-aliasing filter, and a high power amplifier (HPA). The RF front end components are labeled in Figure 3.11. Each component is described in further detail next.

3.3.1 AGC

The first section of the RF front end is a computer-controlled programmable attenuator, which provides AGC. We use a Mini-Circuits ZFAT-4816. As the total power at the input to the receiver drifts due to time-varying RFI, the gain control adjusts the attenuation so as to maintain a constant level to the analog-digital converter (ADC). The attenuator has three-bit control, corresponding to 8 levels of attenuation ranging from 3 dB to 31 dB (see Table 3.1). Section 3.6 gives the details of the AGC algorithm.

3.3.2 Anti-Aliasing Filter

The anti-aliasing filter consists of a Mini-Circuits 50 MHz low pass filter SLP-50 cascaded with a Mini-Circuits 50 MHz high pass filter SHP-50 meant to suppress strong RFI below $\sim$ 30 MHz and above $\sim$ 60 MHz. The low pass filter has a -3 dB point at 37 MHz while the high pass filter has a -3 dB point at 55 MHz. The filter chain has 1 dB insertion loss, and the cascaded response is shown in Figure 3.12.

3.3.3 HPA

After the anti-aliasing filter, a HPA is required to elevate the Galactic noise power above that of the ADC quantization noise power. The HPA is a Mini-Circuits ZFL-2500VH. The amplifier gain is $G_{HPA} = 21$ dB, noise figure $\sim$ 5.3 dB, output IP3 at $\sim$ 18.5 dBm, output 1 dB compression point at $\sim$ 9 dBm, and at 15V the current rating is 80 mA [29].

3.4 Digital Interface

The digital interface consists of the portion of the receiver which converts the analog voltages taken from the antenna into digital samples and the hardware associated with storing these samples on a computer.

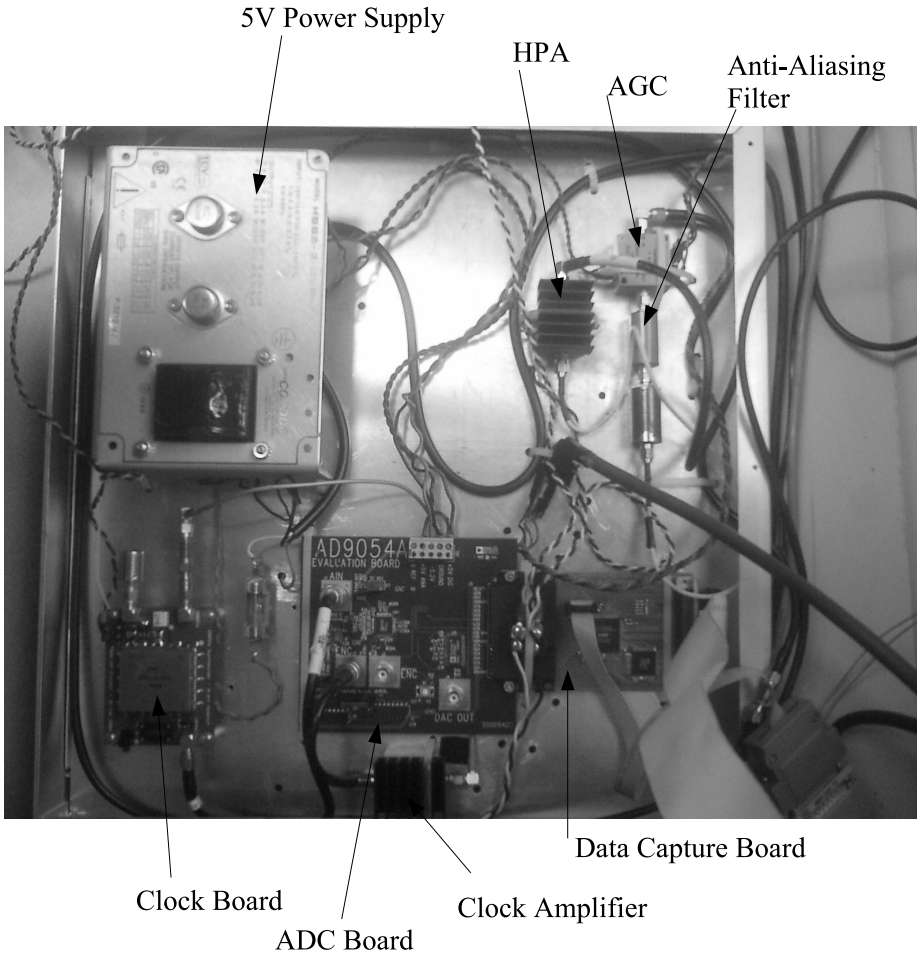

Figure 3.11: Picture of designed receiver, labeling each component.

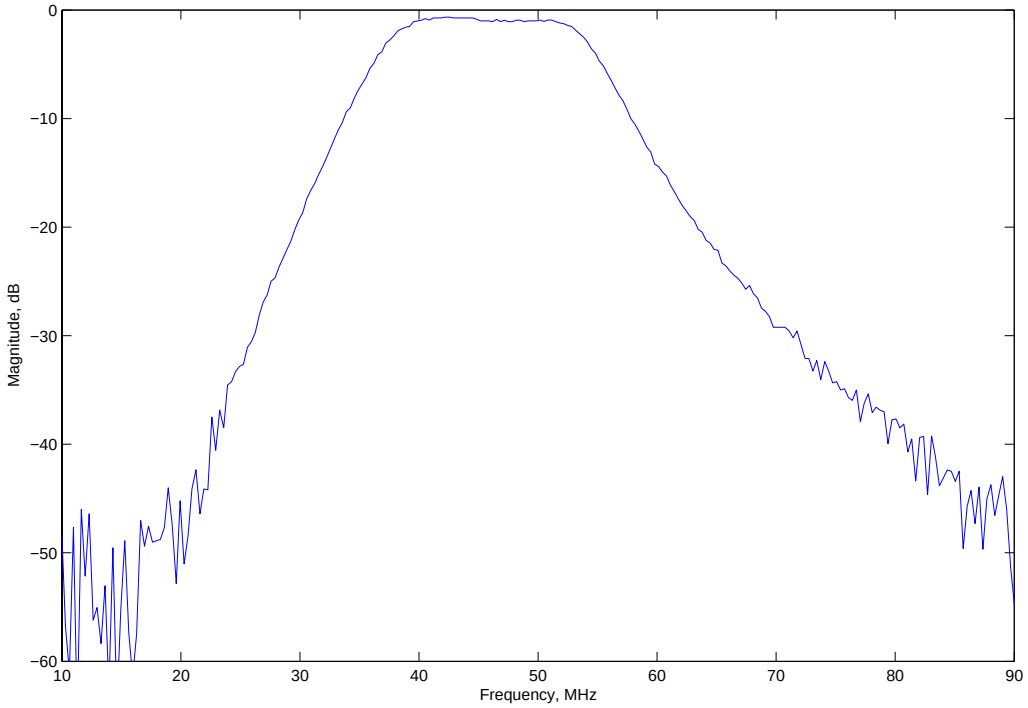

Figure 3.12: Measured response for the front-end anti-aliasing filter.

3.4.1 ADC

The ADC is an Analog Devices 8-bit AD9054 200 MSPS converter. This ADC can be purchased separately or as part of an Analog Devices evaluation board. We use the AD9054A-200 (Model No. AD9054A/PCB) evaluation board, which includes the AD9054 and some peripheral circuitry. The maximum input power to the board is $P_{clip} = 5.5$ dBm. Further information on the specific configuration of the board for our instrument can be found in Appendix C.2.

The analog-digital converter introduces noise into the system through quantization error. Quantization noise power is conveniently described in terms of an ADC's quantization dynamic range (QDR), defined as the maximum (unclipped) input power divided by the quantization noise power. We have measured the QDR of our ADC board to be $\sim$ 43 dB. Using these values for dynamic range and P_{clip}, the quantization noise power, referenced to the board input, is -37.5 dBm, corresponding to a power spectral density of ~ -120.5 dBm/Hz. The result in terms of system performance is shown in Figure 3.13. Figure 3.13 plots the undesired component noise powers along with the desired Galactic background. $N_{q,avg}$ is average quantization noise power over the usable bandwidth. It can be seen that the Galactic noise dominates over all other instrument noise sources from $\sim$ 36 to 56 MHz, achieving the requirement of Galactic noise-dominated observations.

The quantization noise power spectral density is often referred to as a 'noise floor'. This noise floor is irreducible, so if we input a signal which is, for example, 0 dBm, the signal's dynamic range after quantization is only 35.5 dB. For this reason, we would ideally like to operate the ADC with the maximum input power which remains safely below the clipping level. The signal input to the ADC consists of the desired Galactic background and undesired noise powers, which vary only slowly over a few dB at most, plus interference intercepted by the antenna, which can vary by tens of dB. The AGC helps to mitigate this problem by providing additional attenuation when strong interference is present and less attenuation when strong interference is absent.

3.4.2 Sampling Clock

The ADC clock is generated by a clock board developed at the Ohio State University by Grant Hampson for a previous project. The primary component on this board is a Synergy Microwave Corporation OPL-S-200 (Model No. 0403) synthesizer module, which requires 12V and a 10 MHz reference tone. The reference tone is provided by an arbitrary function generator, Stanford Research Systems DS345. Thus, this 'arb' is the ultimate frequency reference for the system. At 12V, the clock output is 3.6 dBm. The clock output is further amplified by 11 dB through the use of a 10 dB attenuator followed by a 21 dB amplifier identical to the HPA in the RF front end.

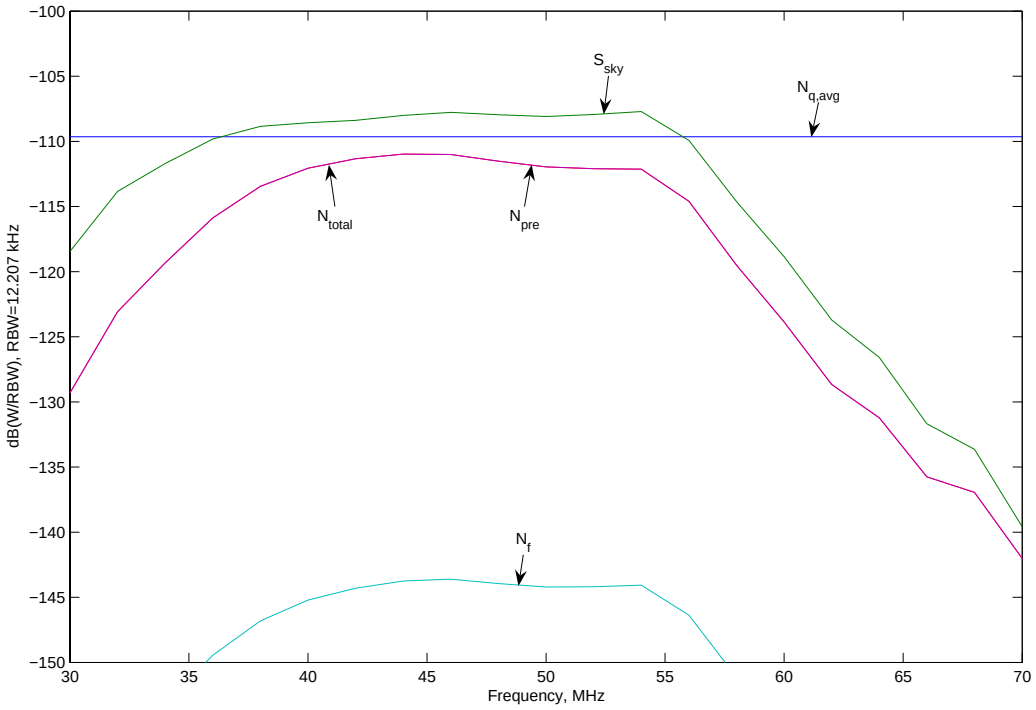

Figure 3.13: Power spectral density of Galactic background and receiver components referenced to the ADC input. Comparing to Figure 3.10, the anti-aliasing filter response and HPA gain can be seen. *Note that the total noise power curve lies nearly on top of that of the preamplifier noise.*

3.4.3 Data Capture Board

The data capture board is a printed circuit board consisting of an Altera ACEX-class field programmable gate array (FPGA) and an IDT 72V295 128K × 18 bit first-in-first-out (FIFO) buffer. The board captures samples from the ADC board output and allows asynchronous parallel transfer to the PC. The ADC synchronously outputs 8 bit samples to the FIFO until the buffer is full, precisely 256K samples. The FIFO asynchronously outputs the requested number of samples via a 68-pin SCSI3 ribbon cable to the computer on request. The transfer request is initiated by the FPGA. The board also uses an Altera ACEX EP1K30TC144-3 FPGA to set up transfers between the FIFO and PC. Source code is written in Quartus II Web Edition, and is programmed onto the FPGA via an IEEE Std. 1149.1 (JTAG) connector and a ByteBlaster MV cable. The programming cable plugs into the personal computer's parallel port. The FPGA firmware is found in Appendix D.1. This board was developed at the Ohio State University by Grant Hampson, Steve Ellingson, and Joel Johnson. More information on the board can be found in Appendix C.3

3.5 Personal Computer

A National Instruments PCI-DIO-32HS PCI board is used to transfer digitized data to the PC. This board provides a high speed (up to 76 MB/s) × 32 bit digital parallel interface with the PC. The board is controlled with C code using extensions provided by the National Instruments LabWindows/CVI development environment (Section 3.6). The reader is referred to Appendix C.1 for additional configuration details. The PCI-DIO-32HS is installed in a personal computer with an AMD Athlon 1.53 GHz processor and 128 MB RAM running Windows XP Professional.

3.6 Instrumentation Software

The instrumentation software used in this experiment was modified from that written by Grant Hampson for evaluation of the performance of the AD9054A evaluation board [30]. In the 'Capture Spectra' program, data is output to files containing a user-defined number of samples. In the 'Capture Time Series' program, data is output to files containing 16K samples each (128 KB). Each filename is comprised of the date and time of the acquisition, as well as the value of a counter. The counter ensures that two files captured within the same second do not have the same name. Appendix D.2 contains the C code for the two programs.

Capture Spectra

This program was written to facilitate initial diagnostic tests of the receiver. The graphical user interface (GUI) allows the user to specify number of samples per acquisition, integration time, and whether or not to write the individual data files to disk. As the program acquires data samples from the receiver, it plots the time series, as well as instantaneous and integrated spectra, obtained using an N-point FFT, where N is the number of samples in each acquisition. Using 16K samples/acquisition, integrating for 17 seconds, and writing to file only the integrated spectra, the duty cycle is $\sim 0.15\%$, for an effective integration time of ~ 0.025 seconds per file.

Capture Time Series

This program was written to capture and store raw data as quickly as possible (spectra are not computed). There is no GUI, as all parameters are set in the main program loop; the user simply has the option to start and stop the acquisitions. Acquisition length is fixed at 16K samples (81.92 μs). This code writes 8 to 12 files per second, resulting in a duty cycle $\sim 0.1\%$.

AGC

As part of both of the above programs, this subroutine calculates and sets the attenuation at the AGC. The subroutine calculates the power in the current acquisition and determines if it is near the clipping power of the ADC. If it detects that 100 consecutive acquistions are clipped, it steps up the attenuation by one level. If 10 acquisitions in a row are below the clipping power of the ADC, and if stepping down the attenuation still allows the acquisitions to remain below clipping, the attenuation is stepped down one level. The level is written to the parallel port and subsequently to the gain controller. Based on a three pin reference, there are eight levels of attenuation, from 3 dB to 31 dB, shown in Table 3.1.

3.7 Summary

In this section, we summarize the characteristics of the instrument. Table 3.2 shows the specifications of the designed instrument. Also, since Galactic noise-dominance is an important consideration, Figure 3.14 shows by how much we are Galactic noise-dominated. The ratio of Galactic noise, S_{sky}, to total instrument noise, $N_{pre} + N_f$, is defined as $\gamma = \frac{S_{sky}}{N_{pre}+N_f}$. Since we are minimally dominated by Galactic noise, it would be helpful in future experiments to provide more front end gain. If we provided more gain in this instrument, the interference would have saturated the ADC, extending it into nonlinear operation. More of the spectrum

Table 3.1: Gain Controller Response

Written to Port	**Pin Levels**	**Attenuation (dB)**
0	000	-2.9
1	001	-6.8
2	010	-11.0
3	011	-14.9
4	100	-18.8
5	101	-22.8
6	110	-26.8
7	111	-30.7

could have been filtered out, however a necessary requirement was as large a bandwidth as possible.

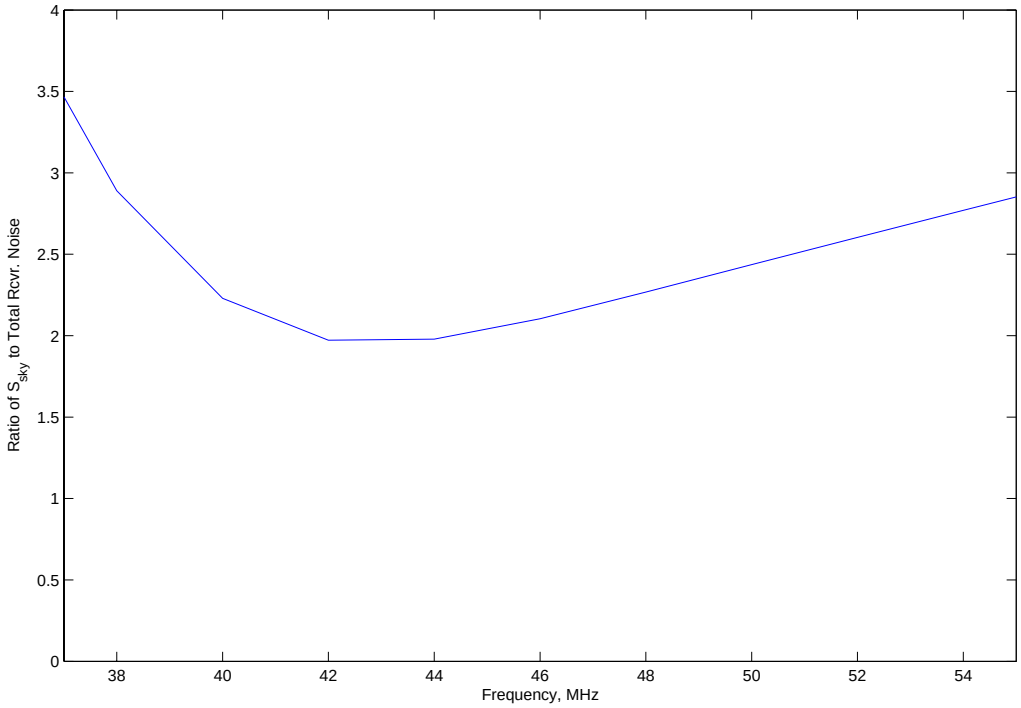

Figure 3.14: Ratio of Galactic noise to Instrument noise, γ

Table 3.2: As Built Receiver Specifications

		Remarks
Center Frequency Gain	54 dB	46 MHz
Observing Frequencies	37-55 MHz	Half-power points
Galactic Noise Dominated Bandwidth	18 MHz	
$\Delta\nu$	12.2 kHz	16K FFT
Δt	81.92 μs	16384 samples @ 200 MSPS
Duty Cycle	$\sim 0.1\%$	16K samples/acquisition)
IIP3	-16 dBm	
System Temperature	~ 627 K	
System Stability	~ 17 s	determined experimentally (Section 5.2.1)
System Sensitivity	~ 0.98 MJy	determined experimentally (Section 5.2.2)
Effective Aperture	~ 11 m^2	at zenith, 46 MHz
Field of View	$\sim \pi$ sr	

Chapter 4

Data Analysis

This chapter describes the software developed for data analysis in this experiment. Data analysis includes RFI mitigation, correction for instrumental effects (spectral ripple removal), and the search for dispersed pulses. All data analysis is performed offline from stored data files. A flowchart describing the data acquisition and analysis is shown in Figure 4.1.

4.1 RFI Mitigation and Baseline Correction

RFI degrades sensitivity by saturating the dedispersion algorithm and creates spurious detections. To mitigate the effects of RFI, a frequency bin blanking procedure is implemented. In addition to RFI, there is a spectral ripple attributed to reflections along the feedline since the feedline sections are tens of meters long. This ripple masks weak spectral features, so to obtain as much sensitivity as possible, a baseline correction is performed. Also, because the ripple complicates RFI excision, an iterative procedure is required. The RFI mitigation and baseline removal procedure follows.

1. Obtain the power spectral density of each acquisition.

$$S = E\left[XX^*\right] \text{ W bin}^{-1} \tag{4.1}$$

   where $X = F[x]$, the Fourier transform of the time series, and X^* denotes the complex conjugate. The transform is implemented as a triangle-windowed 16K FFT.

2. The anti-aliasing filter response shown in Figure 3.12 is divided out.

3. Each frequency bin is examined. Any bin which is greater than σ_1 standard deviations above the mean is considered RFI, and the bin is set equal to the mean PSD for that spectrum. σ_1 is somewhat site dependent, representing a tradeoff between excessive blanking and low sensitivity. In Section 5.1.2, we show $\sigma_1 = 9\sigma$ is an appropriate value.

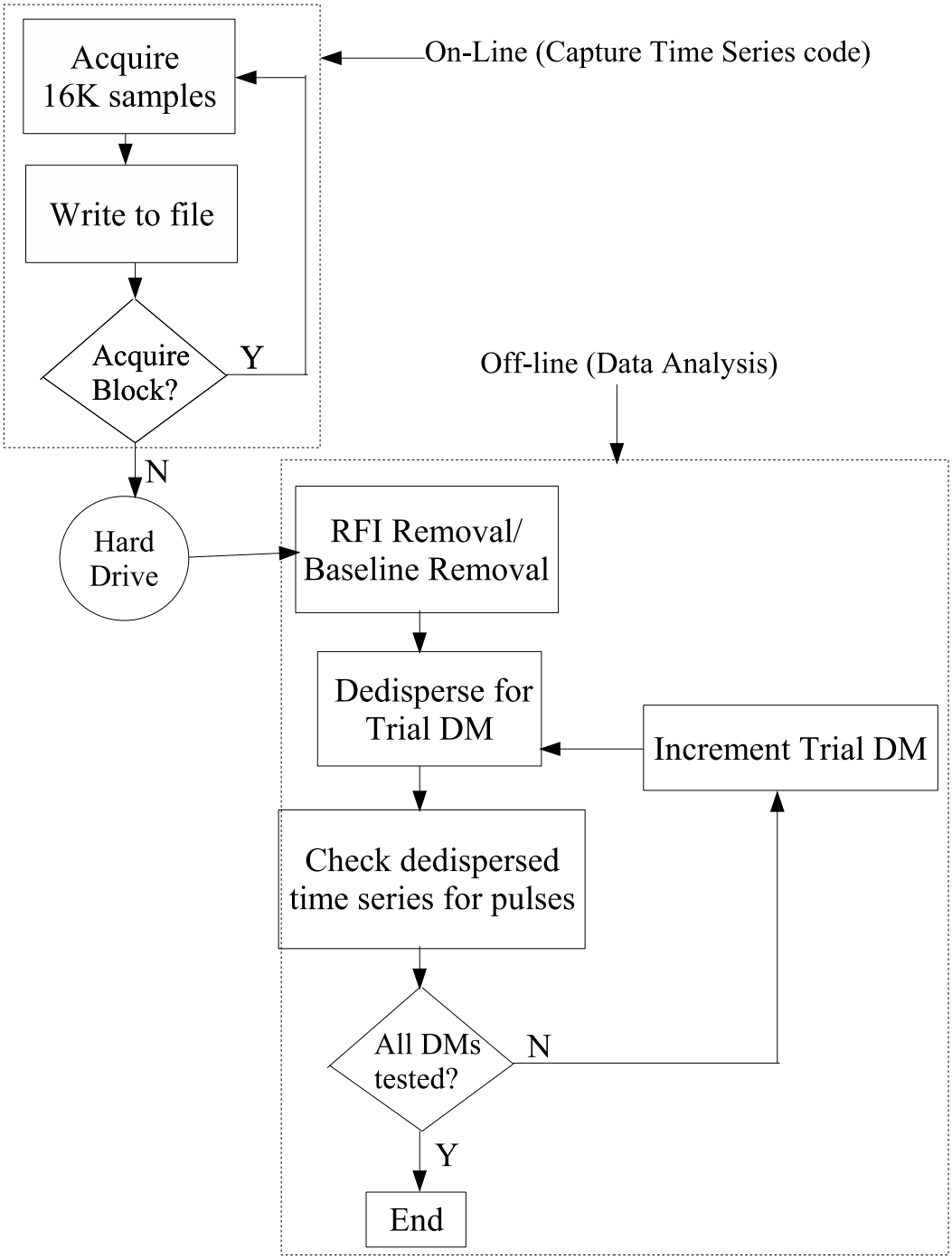

Figure 4.1: Data acquisition and analysis flowchart

4. After the first RFI removal step, a first estimate of the noise baseline is performed in the spectral domain using a simple moving average. The estimate is obtained by using a box-car filter, the output of which is the average of the previous 25 bins ($\sim$ 300 kHz). The number of bins to average together was chosen based on a trial and error study to see which choice best resolved the baseline without being affected by the interference. As most man-made interference is narrowband ($\leq$ 25 kHz), it thus resides in only a few bins, so the choice is appropriate.

5. A second RFI excision step is now performed by stepping through each frequency bin searching for any bins which are greater than σ_2 standard deviations above the smoothed baseline determined previously. These bins are set to the value of the baseline in that bin. Note that RFI detection can now be significantly more sensitive, since the reduced noise baseline ripple reveals weaker RFI, thus we choose $\sigma_2 < \sigma_1$, causing more RFI to be excised. We have used $\sigma_2 = 6\sigma$ (Section 5.1.2).

6. After the second RFI removal, an improved estimate of the baseline is obtained and subtracted out. This baseline estimate is performed in the same manner as before.

7. It is known that without RFI, the total power on the antenna should vary only slightly and slowly, due primarily to solar flares and diurnal variations. Any fast transient will cause very little change in total power. Thus, we mitigate the effects of unexcised RFI by normalizing the total power in each spectrum over time intervals of $\sim$ 15 minutes. Another potential source of problems is solar flares, which would cause spurious detections if received during observation, though we are able to easily discriminate against these since they are very broadband and occur on short time intervals. During our observations, it was determined that no solar flares occurred by examining the Green Bank Solar Radio Burst Spectrometer (GBSRBS) webpage[1].

4.2 Dedispersion

Dedispersion can be performed coherently or incoherently from captured data. Coherent dedispersion is a rigorous (exact) 'de-chirping' of the received signal, using all available phase information. Equation 4.2 gives the relationship between received and emitted electric fields, where the received field has had a phase introduced through dispersion.

$$E_{rcvd}(t) = \int E_{rcvd}(\nu)\, d\nu = \int E_{emitted}(\nu) e^{jk(\nu)z}\, d\nu \tag{4.2}$$

It is noted that $\hat{z}$ represents the line of sight direction, while the frequency term $k(\nu)$ can be determined using a model for the galactic distribution of free electrons [24]. Coherent dedispersion requires multiplication of the Fourier amplitudes by the inverse phase function,

[1] http://www.astro.umd.edu/~white/gb/

$e^{-jk(\omega)z}$. In previous experiments, this has been implemented using Fourier transforms [31] and finite impulse-response filtering [32]. While coherent dedispersion is generally superior to an incoherent method, it has very high computational burden which is further escalated by the presence of RFI, which must be concurrently mitigated.

Incoherent dedispersion operates directly on the power spectrum magnitude (Equation 4.1). This is done by collecting a spectrogram of contiguous short-term power spectra and 'manually' dedispersing by shifting frequency 'columns' (all bins representing a single frequency across all spectra) in time to account for the dispersion. The time delay due to dispersion for a frequency channel is given by

$$\delta t = \frac{DM}{\alpha_d \nu^2} \tag{4.3}$$

where $\alpha_d = 2.41 \times 10^{-16}$ [23] and ν is frequency in Hz. By delaying each frequency channel the appropriate time, the dedispersed time series can be obtained simply by summing across frequency columns. The accuracy of the incoherent dedispersion technique is limited by the frequency channel bandwidth, as there is a delay to cross that bandwidth which never gets removed. Further, there is a penalty associated with the failure to use available phase information; however, the baseline/RFI removal algorithms described in Section 4.1 already assume this. The computational burden of incoherent dedispersion is dramatically less. For these reasons, incoherent dedispersion is used in this experiment.

Generally helpful is the time required for an impulse to traverse two frequencies, ν_1 and ν_2:

$$\Delta t_{2\to1} = \frac{DM}{\alpha_d}\left(\frac{1}{\nu_{1,Hz}^2} - \frac{1}{\nu_{2,Hz}^2}\right) \tag{4.4}$$

Thus the time required for an impulse to traverse the PLFM system bandwidth ($\nu_1 = 37$ MHz and $\nu_2 = 55$ MHz) is $\Delta t \approx 1.7 \cdot DM$ sec. So, for example, a Crab GP (DM = 56.8 pc cm^{-3}) requires ~ 95 s to traverse the passband.

Also, using (4.4) the minimum time resolution possible for a given DM can be determined. The lowest frequency bin represents from 37 to 37.012207 MHz, indicating $\Delta t_{2\to1} = 19.99$ ms for DM = 10 pc cm^{-3} . The highest frequency bin represents from 54.987793 to 55 MHz, indicating $\Delta t_{2\to1} = 6.091$ ms. Thus the shortest pulse resolvable by our dedispersion algorithm for DM = 10 pc cm^{-3} is ~ 6 ms.

The dedispersion procedure detailed below operates on a time-frequency matrix of captured data. The times of each acquisition are known prior to the procedure, so the fact that the acquisitions are not contiguous is not a serious problem. In the case of the PLFM instrument, there are between 8 and ~ 12 81.92 μs acquisitions per second.

1. Choose a trial DM.
2. Determine the minimum time resolution possible for each frequency channel using (4.4); this will give the times represented by each bin of the dedispersed time series.

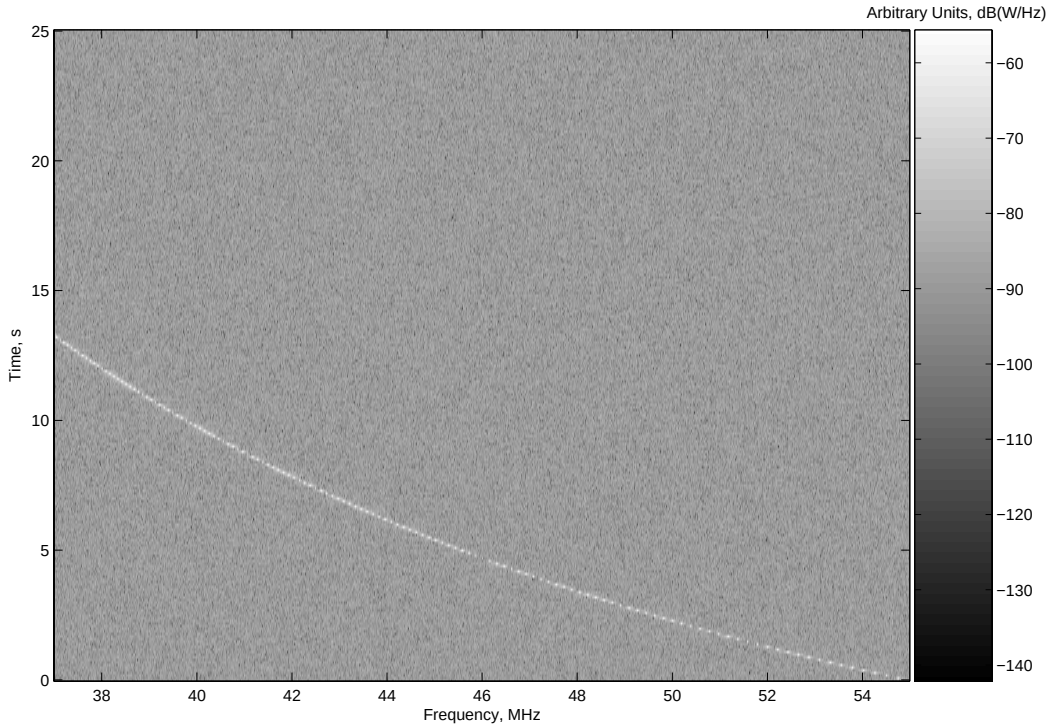

Figure 4.2: Time-frequency matrix for a pulse with DM= 8 pc cm^{-3}

3. Step through each frequency channel, and introduce the appropriate lag. Each frequency channel is made up of a series of time-frequency pixels, and the dedispersed time of each pixel is determined using 2 steps. The time at which the pixel was received is known prior to the algorithm. The time lag which is introduced to compensate for dispersion is given by (4.3).

4. It should be noted that the lag is rarely an integer number of time steps. Instead, the times of each bin in the dedispersed time series are known from step 2. Each time-frequency pixel will have a time associated with it after the appropriate lag has been introduced. This pixel is added to the dedispersed time series bin whose time is closest to that of the pixel.

To demonstrate the procedure, consider the following simulation. Figure 4.2 shows a time-frequency matrix for a simulated pulse with DM = 8 pc cm^{-3}, and Figure 4.3 shows the time-frequency matrix after dedispersion. The simulated pulse is shown in Figure 4.3 by a gray streak at time $\sim$ 13.5s. Figure 4.4 shows the output of the dedispersion algorithm checking for DM = 8 pc cm^{-3} . The dedispersed time-frequency matrix in Figure 4.3 helps to illustrate why there is a curved noise floor in the dedispersed time series of Figure 4.4:

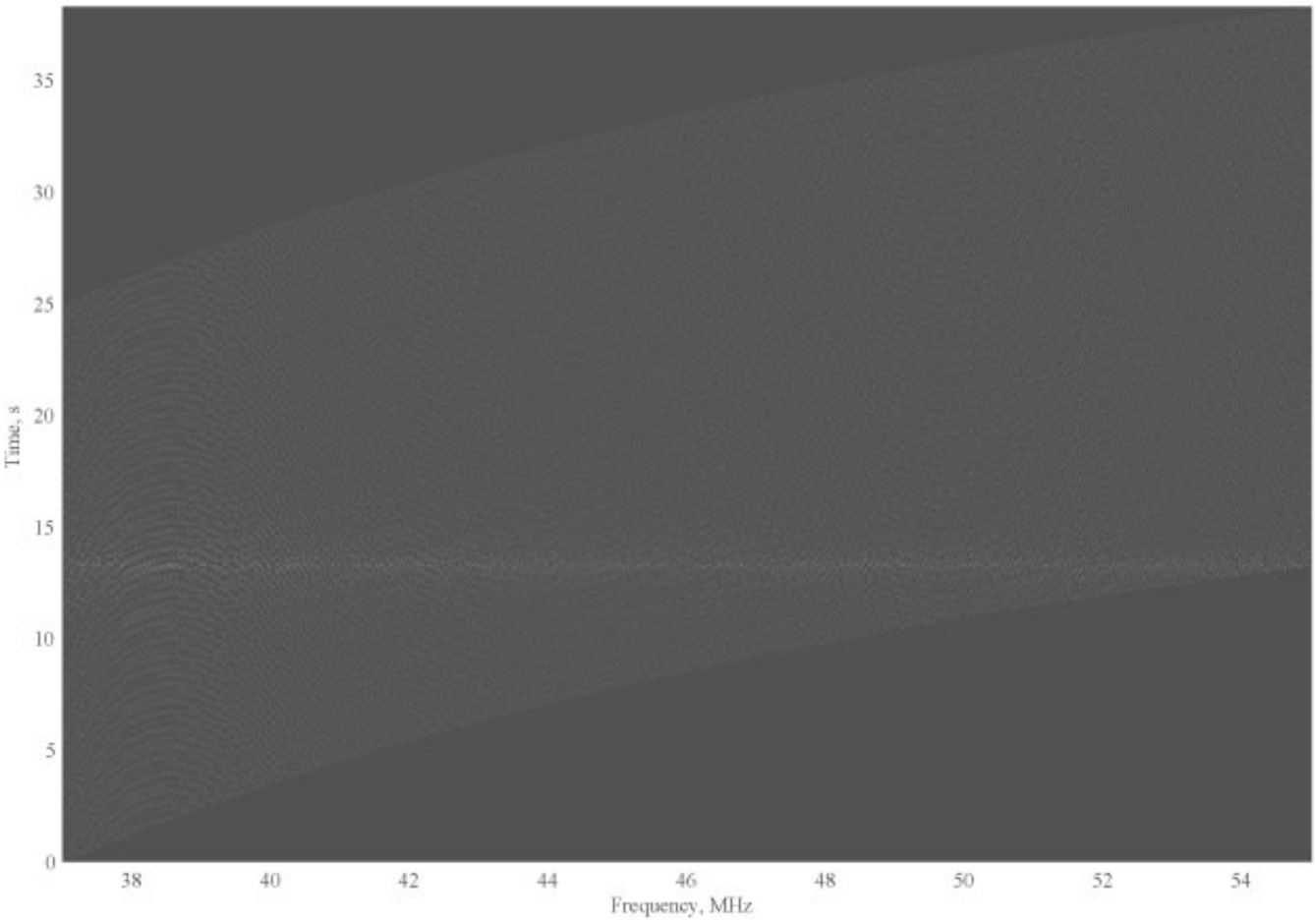

Figure 4.3: Time-frequency matrix for a pulse with DM= 8 pc cm^{-3} after dedispersion

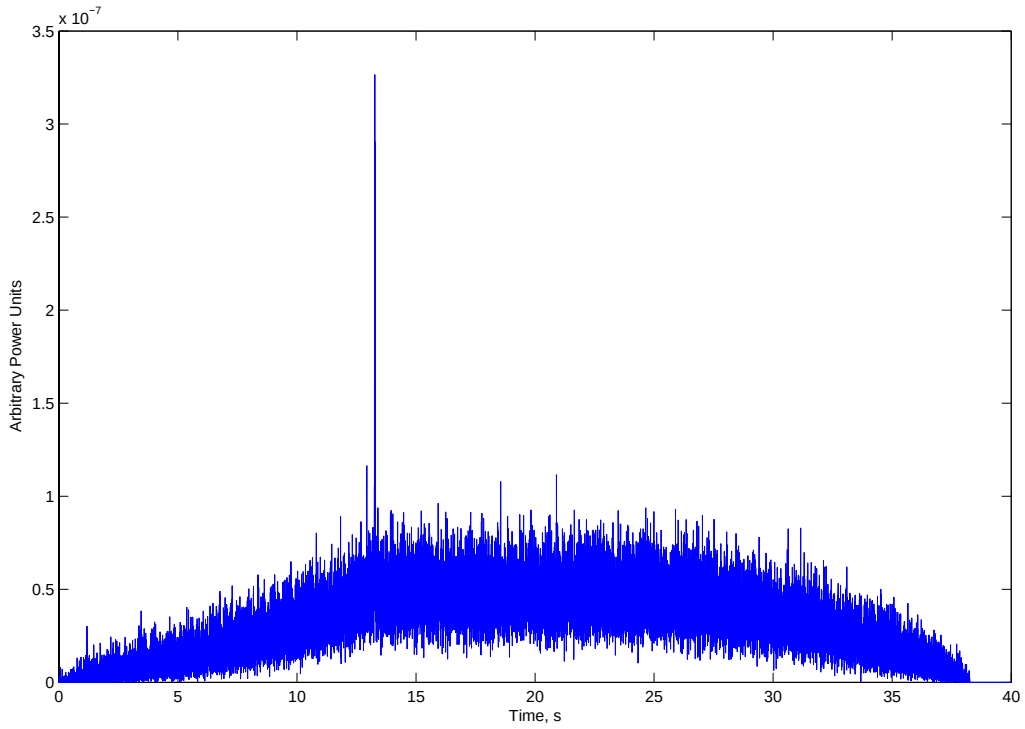

Figure 4.4: Dedispersion output for pulse shown in Figure 4.2

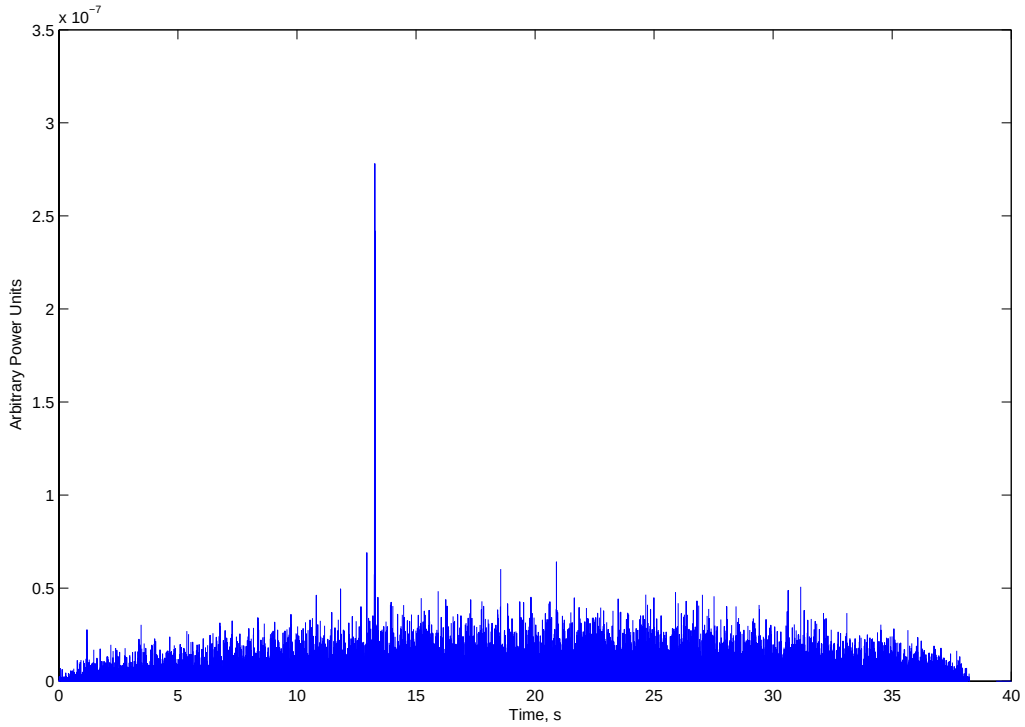

Figure 4.5: Baseline corrected dedispersion output for pulse shown in Figure 4.2

The dark black portions near the beginning and end of the time axis represent zeros due to lack of data, while near the middle of the time axis, more nonzeros elements are added together. The large amount of black throughout the spectrogram is due to non-contiguous acquisitions (due to the low duty cycle acquisitions). In order to compensate for the curved noise baseline bias, we perform a moving average with approximately $N/20$ taps, where N is the number of samples in the dedispersed time series. The factor of 20 is used because this causes the moving average to move smoothly along the baseline, without much affect by the short pulses. This moving average is subtracted out from the dedispersed time series, and the result is shown in Figure 4.5.

4.2.1 Dispersion Measure Range

As mentioned previously, the DM of a received transient is generally not known *a priori*. The amount of dispersion is determined primarily by the path through the Galactic plane through which the transient propagates. Cordes and Lazio [24] have developed a model for the Galactic distribution of free electrons, and they give the maximum DM at a galactic

longitude of 0° (looking through the plane of the Galaxy) as ~ 1800 pc cm^{-3}. This increases to ~ 3400 pc cm^{-3} looking directly into the galactic center. Looking out through the poles of the Galaxy, the maximum dispersion measure decreases to ~ 200 pc cm^{-3}.

It is known from pulsar surveys that detection above ~ 1200 pc cm^{-3} is unlikely because of pulse broadening due to dispersion smearing and interstellar scattering [24]. Thus it makes sense to focus data processing time on DMs less than ~ 1200 pc cm^{-3}, with more time devoted to smaller DMs. For deciding upon a *minimum* dispersion measure to check, the level of the RFI is the biggest factor. Most RFI has an 'effective' DM of zero, and therefore detection of pulses at low DMs is very difficult in the presence of RFI due to an increased false alarm rate, even at detection thresholds as high as 7 or 8σ. At high enough DMs, most interference is 'smeared' out into the noise floor.

4.2.2 DM Resolution

For test sensitivity, it makes sense to check for dispersion measures on as fine a grid as possible. In practice, the optimal grid size requires a tradeoff between sensitivity and computational time. If the spacing between trial DMs is too sparse then sensitivity to untested DMs is lost, while if it is too dense, computational time is wasted. We define the detection metric as the power in the dedispersed time series. Our choice is to have the trial DM spacing chosen such that the 3 dB points of detection metrics overlap. To illustrate this, the detection metric for DMs between 7 and 9 pc cm^{-3} due to the simulated pulse at DM = 8 pc cm^{-3} from Section 4.2 is shown in Figure 4.6. The 3 dB points are at DM = 8.0 and 8.4 pc cm^{-3} . Note that the pulse appears to have a DM of 8.02 indicating an error in the algorithm by +0.02 pc cm^{-3} . In this case, the trial DMs should be set at 8.0, 8.02, and 8.04 pc cm^{-3} . Using this same procedure, the trial spacing for the range 0 to 1000 pc cm^{-3} is shown in Figure 4.7. This is well approximated by a 4th-order polynomial:

$$y = -7.26 \times 10^{-8}x^3 + 1.83 \times 10^{-4}x^2 - 1.29 \times 10^{-2}x + 0.605; \tag{4.5}$$

where y is the chosen DM spacing, and x is DM in pc cm^{-3} .

4.3 Pulse Detection

The procedure for detecting pulses in the dedispersed time series is given below.

1. Find the mean, m_t, and variance, σ_t^2 of the time series.
2. Find the largest sample, x_{max}, in the time series. The detection metric for this sample is defined as
$$\sigma_p = \frac{x_{max} - m_t}{\sigma_t^2}\sigma \tag{4.6}$$

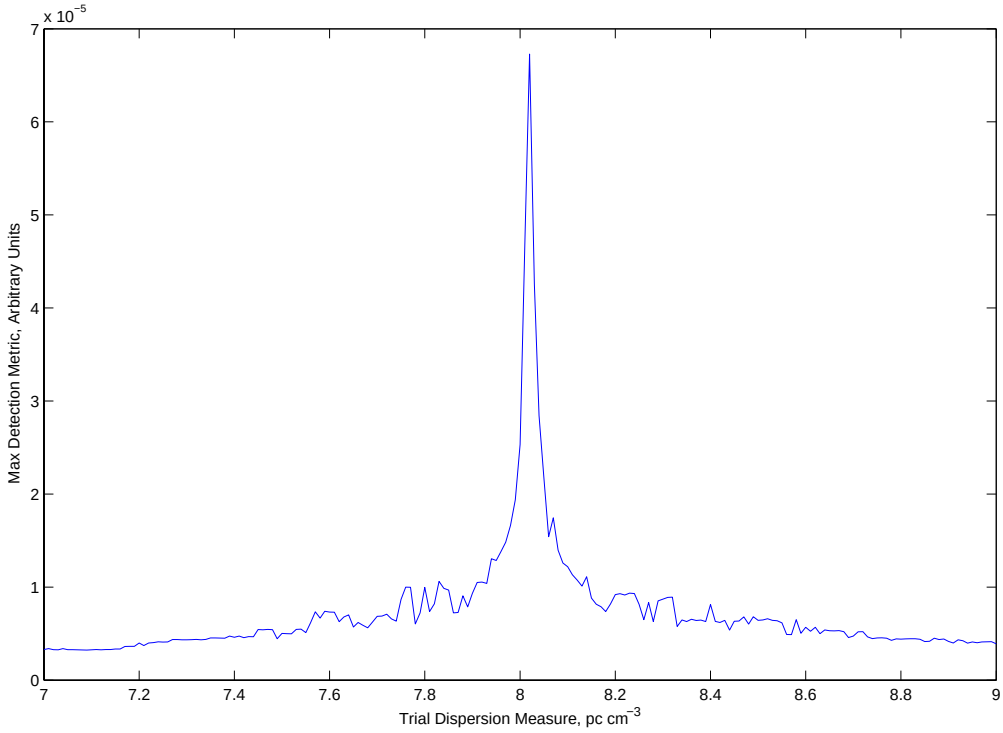

Figure 4.6: The detection metric for trial DMs between 7 and 9 pc cm^{-3} with a pulse at DM = 8 pc cm^{-3}

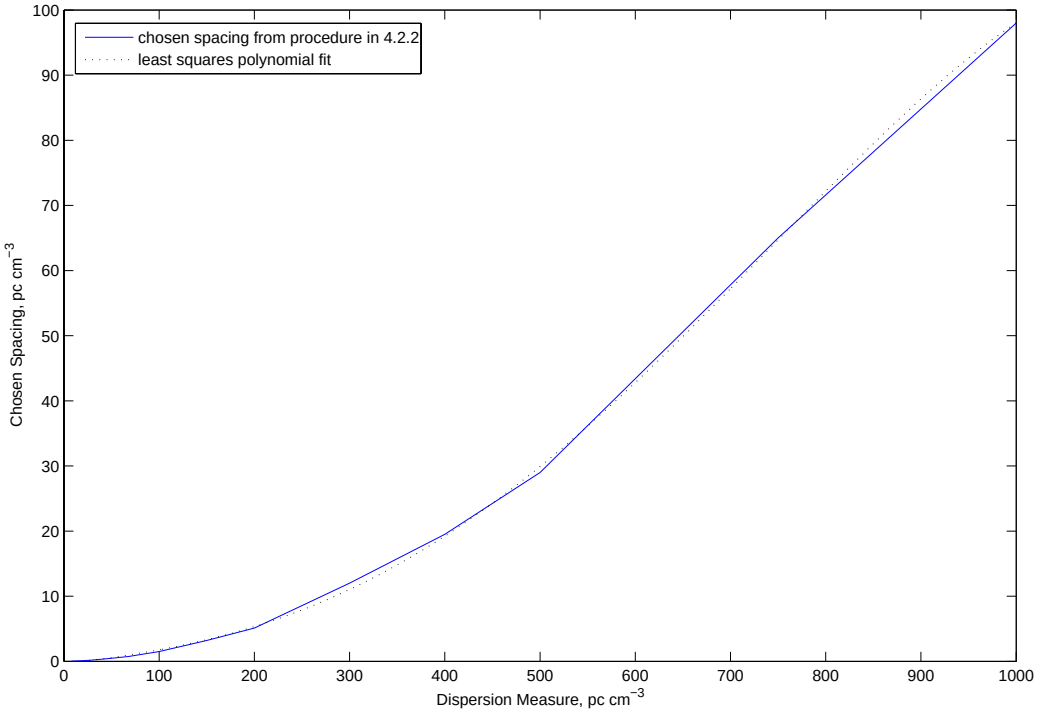

Figure 4.7: Calculated DM spacings in the range 8 to 1000 pc cm^{-3}

i.e. the number of standard deviations above the mean.

3. Note the time and detection metric for this time sample, and temporarily set the time sample to zero.

4. Repeat Steps 1-3 until all samples exceeding some threshold are recorded. For our observations, all samples which exceeded 3σ were found and recorded.

4.4 Detection Threshold Setting

In order to determine a threshold for further review of detected pulses and to confirm the dedispersion and pulse detection algorithms, we simulate a white Gaussian noise (WGN) time-frequency matrix and dedisperse it for trial DMs in the range 10 to 75 pc cm^{-3} . The fraction of pulses detected in a bin 0.25σ wide vs. the detection metric is shown in Figure 4.8. On top of this curve, the same calculation taken from the WGN time series (without dedispersion) is plotted. It is noted that where the detector output deviates significantly from that expected for Gaussian noise would be a good selection of detection thresholds. The plot shows that dedispersion does not significantly affect the detection statistics, as expected.

The same procedure was used to characterize actual field data (discussed further in Chapters 5 and 6), shown in Figure 4.9. Note that detections deviate from that expected for WGN between 6 and 7σ. The threshold for further review of detected pulses is ultimately based on a desired false alarm rate (FAR), and for somewhat aggressive detection at an elevated FAR, a threshold of 6.5σ appears reasonable. For WGN, this gives a FAR $<< 5 \times 10^{-8}$ or less than 1 throughout the duration of the observation.

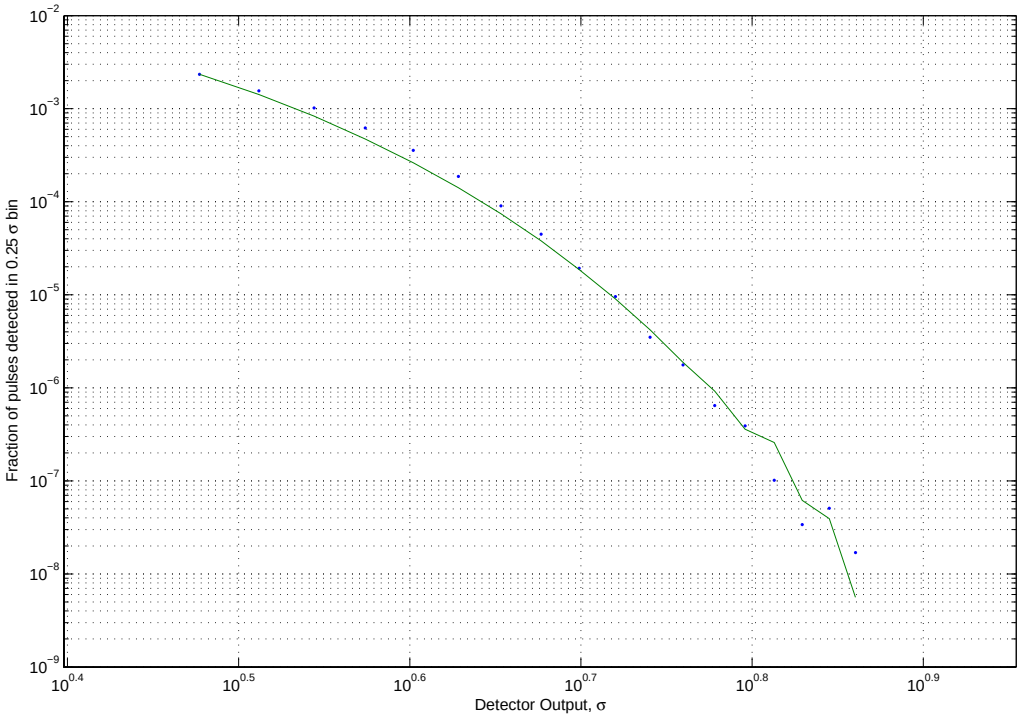

Figure 4.8: Analysis of simulated WGN data. *Dots:* Fraction of all pulses detected above 3σ in bins 0.25σ wide for DMs between ~ 3 and 75 pc cm^{-3}. *Line:* Same result for perfect white Gaussian noise input taken from actual time series (without dedispersion).

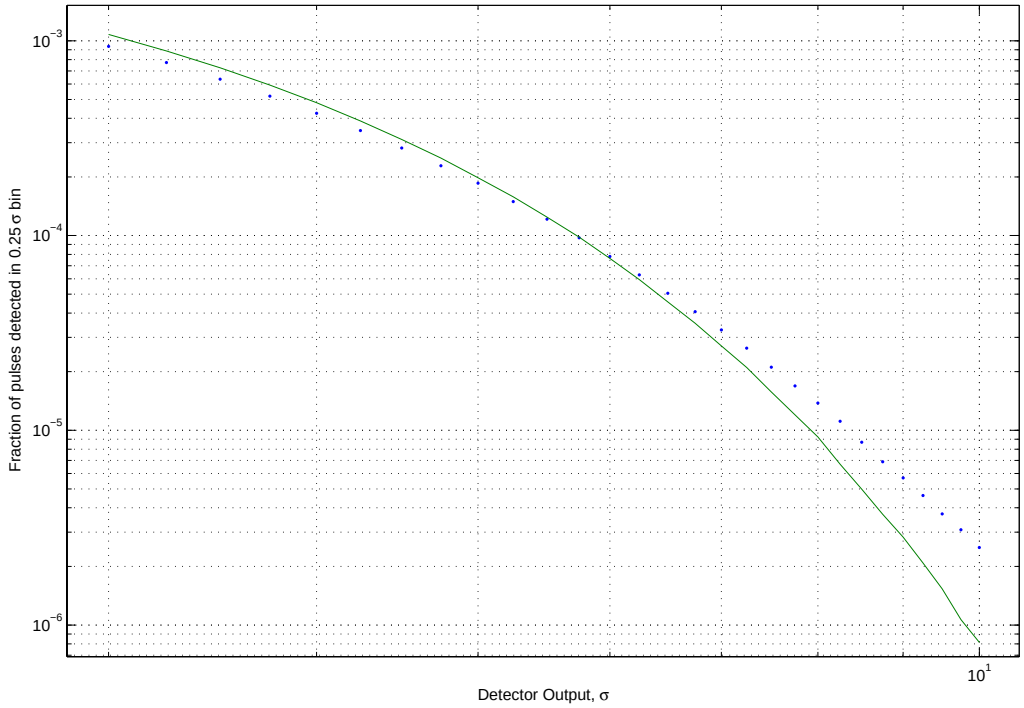

Figure 4.9: Analysis of actual field data. *Dots:* Fraction of all pulses detected above 3σ at the output of the threshold detector in 0.25σ bins for dispersion measures between ~ 3 and 75 pc cm^{-3}. *Line:* Same result for perfect white Gaussian noise input.

Chapter 5

RFI Threshold Setting, Instrument Stability, and Sensitivity

In the previous chapter, we described the data analysis algorithms to be used, but left undetermined the parameters σ_1 (the threshold used for the 1st RFI excision) and σ_2 (the threshold used for the 2nd RFI excision), because they are site-specific. In this chapter we set these parameters using an analysis of actual field data collected at the experiment site. In Section 5.2.1 we consider the stability of the instrument, to make sure that sensitivity is not significantly affected. In Section 5.2.2, we compute an estimate of the experiment pulse detection sensitivity.

5.1 RFI Threshold Setting

5.1.1 RFI Characterization

Figure 5.1 shows an integrated spectrum obtained October 23, 2004 from $\sim$ 21:36 to 21:53 UT (about 1 second effective integration time), and the RFI can be easily seen.

The sources of RFI can be obtained from an FCC frequency allocations table [1]. Note the onerous signal at 42.62 MHz. This signal is due to a state police radio and is intermittent[2]. Figure 5.2 shows the total power in 37-55 MHz vs. time. It was determined that the large jumps are due to the police radio communication by examining the individual spectra and noting that a strong signal at $\sim$ 42.6 MHz was present.

In addition to the state police radio signal, there are at least 13 other noticeable interference signals. Of these, 5 are fixed US/local government communications, 5 are land mobile

[1] http://www.ntia.doc.gov/osmhome/allochrt.pdf
[2] http://www.suhfars.com/scanners.htm

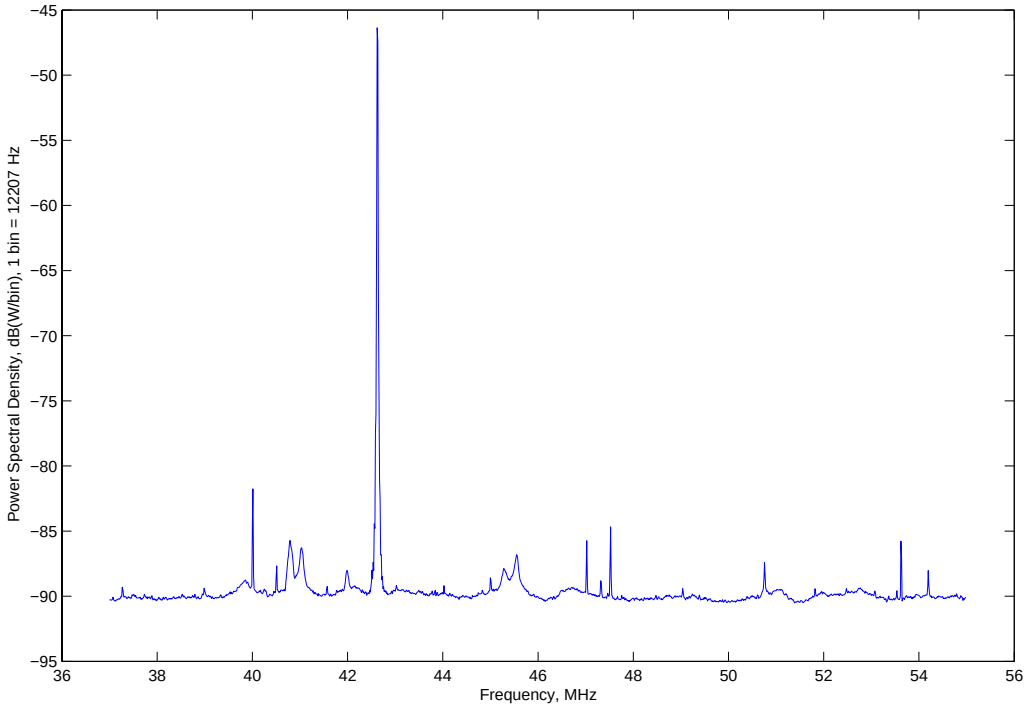

Figure 5.1: Integrated spectrum from a 20 minute observation window

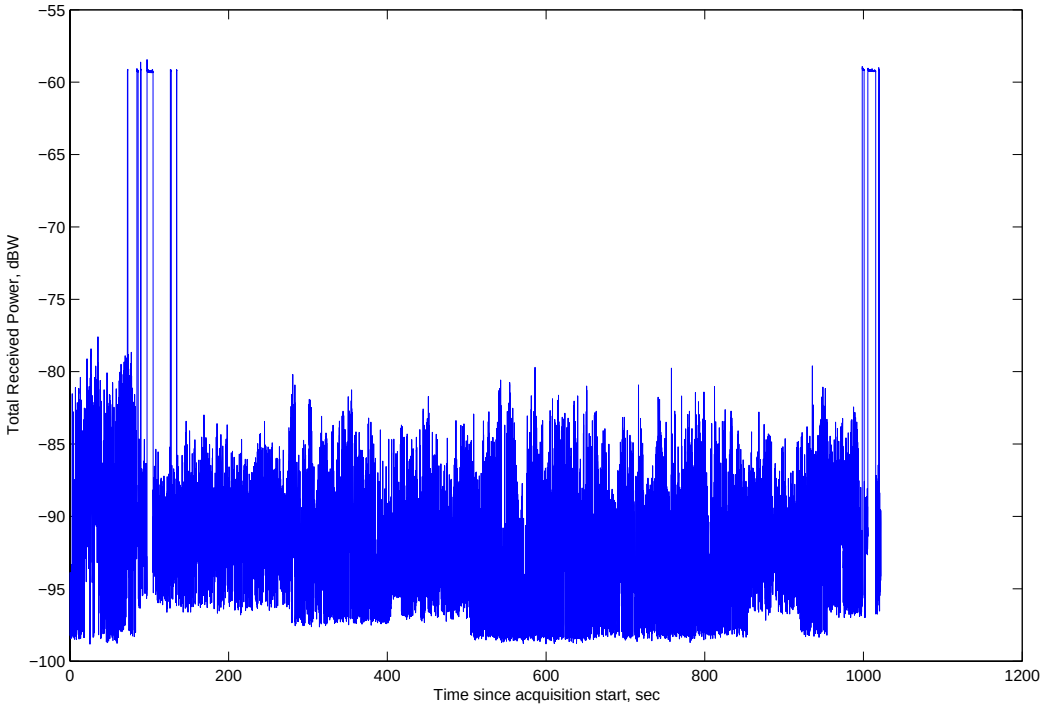

Figure 5.2: Total power in 37 to 55 MHz vs. time for $\sim$ 20 minute observation window. Note the large jumps in power due to the state police radio

Table 5.1: Radio-frequency interference in the system bandwidth

frequency (MHz)	Observed peak PSD (dBW/12.21 kHz)	source from alloc. chart
40.012	−81.76	US Government
40.512	−87.68	US Government
40.793	−85.72	US Government
41.035	−86.28	US Government
41.988	−88.03	US Government
42.622	−46.37	State Police
45.280	−87.88	Police/Local Gov't/Hwy Maint
45.548	−86.81	Police/Local Gov't/Hwy Maint
47.024	−85.74	Hwy Maint
47.317	−88.82	Hwy Maint
47.524	−84.68	Industry/Emergency
50.756	−87.39	Amateur 6 m Radio
53.622	−85.77	Amateur 6 m Radio
54.195	−88.03	Broadcast TV Ch. 2 Video

highway maintenance communications, 2 are amateur radio communications, and 1 is a broadcast TV station. Table 5.1 summarizes the interference frequencies, observed max power spectral densities, and the sources.

5.1.2 Selection of σ_1 and σ_2

While we want to be somewhat stringent on RFI mitigation, selection of the decision thresholds is heavily site dependent. On one hand, we don't want to preclude detection of a strong transient due to its unintentional excision by RFI mitigation, and on the other hand, we don't want so much RFI that the false alarm rate increases to an unmanageable level.

Figure 5.3 shows an integrated spectrum after the RFI excision in Step 3 of Section 4.1, using a threshold $\sigma_1 = 9\sigma$. The state police radio is almost completely blanked, leaving only the lower level interference. On the average, 0.44% of frequency bins are blanked using this threshold in the first RFI excision step.

Figure 5.4 shows the result after Step 5 of Section 4.1, using a threshold $\sigma_2 = 6\sigma$. Note most interference is brought to within 1 dB above the noise floor, while a few remaining signals are within 2 dB of the noise floor. Figure 5.5 shows the result after Step 7 of Section 4.1. Note the spectral ripple is now effectively removed and only very low-level RFI remains. The results of Chapter 6 will confirm that the remaining RFI represents a manageable problem;

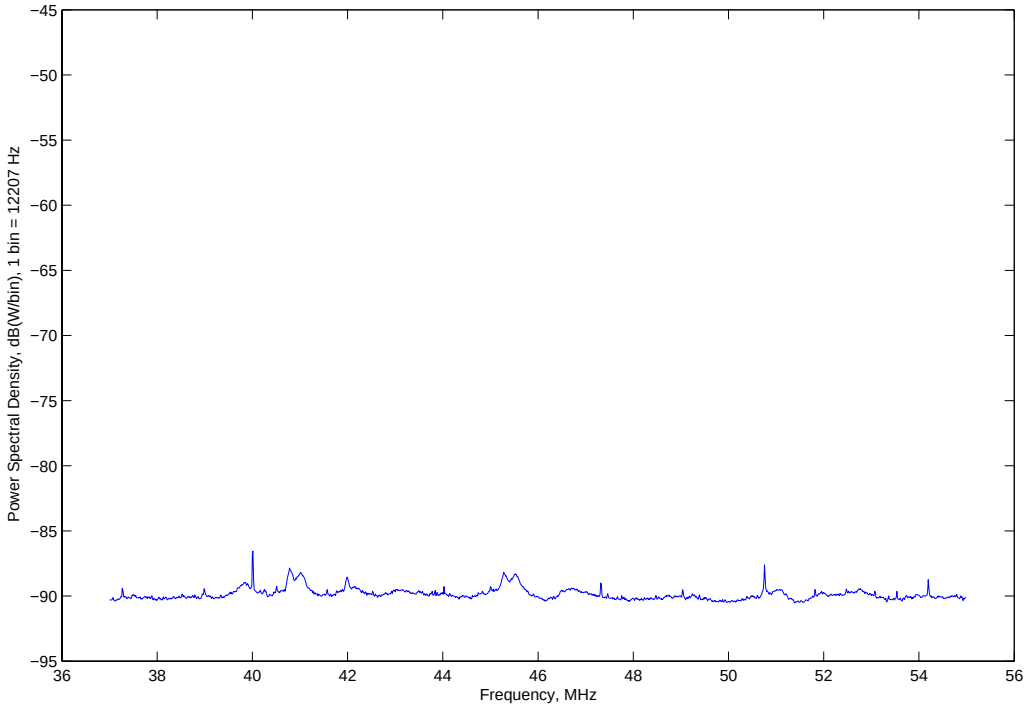

Figure 5.3: Integrated spectrum after 1st RFI removal. Note the lack of the strong interference at $\sim$ 42.6 MHz seen in Figure 5.1

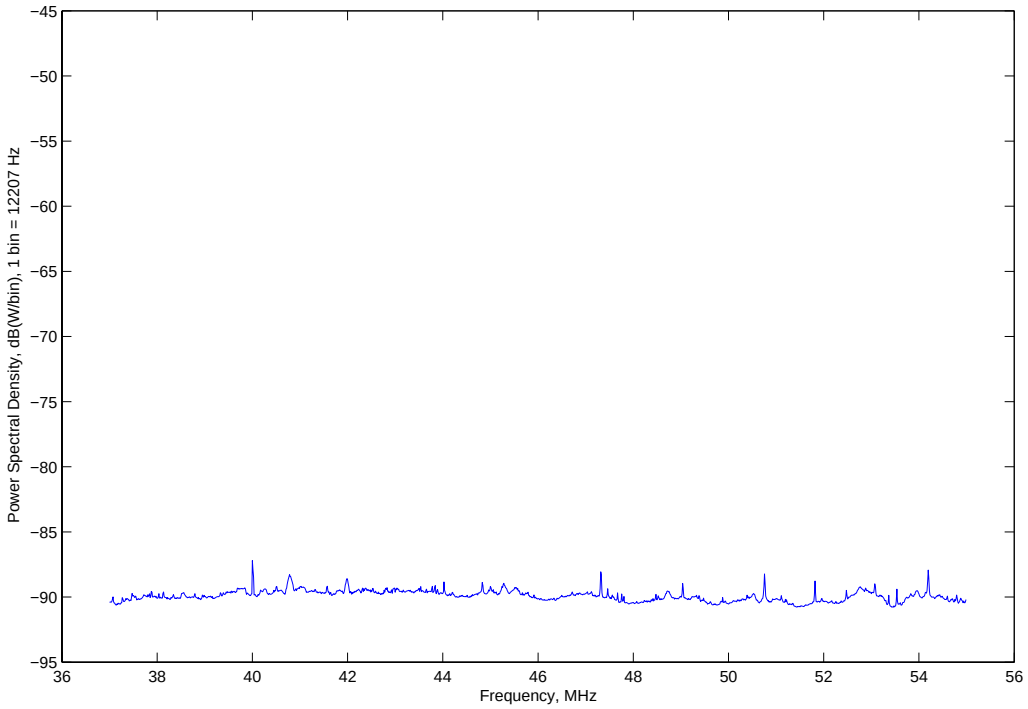

Figure 5.4: Integrated spectrum after 2nd RFI removal

after dedispersion smearing, the number of spurious detections is relatively small.

5.2 Instrument Characterization

5.2.1 Stability

All radiometric instruments have limited stability, due to unavoidable variations in gain over time. When gain variations dominate over reduction of variance by averaging, no further improvement in sensitivity is possible. Stability refers to the extent to which integration (averaging) of PSDs can improve sensitivity. Let us consider an ideal noise source whose samples are taken from the distribution

$$X = \sqrt{N_o}\frac{Z_1 + jZ_2}{\sqrt{2}} \tag{5.1}$$

where Z_1 and Z_2 are independent identically distributed Gaussian random variables. In radiometry, the central problem is to estimate N_o from L samples of the distribution. Since

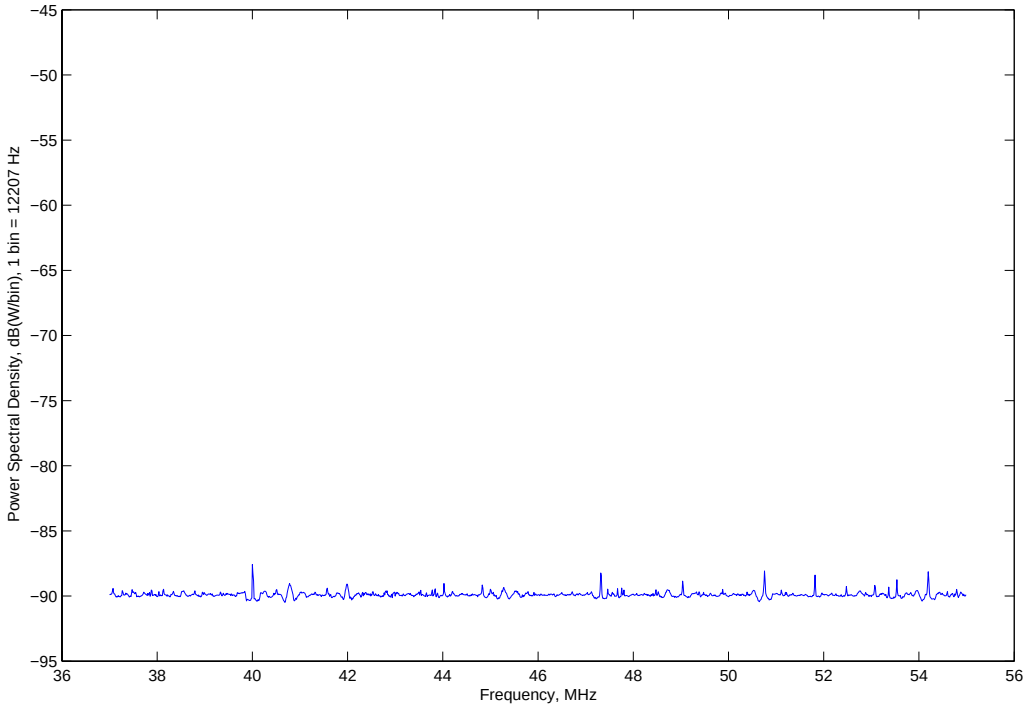

Figure 5.5: Integrated spectrum after baseline removal and normalizing individual spectrum powers

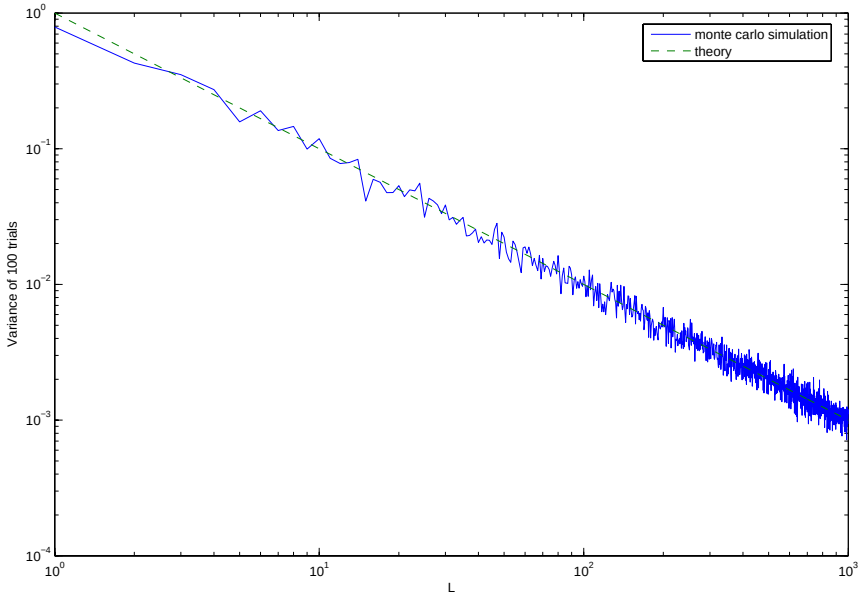

Figure 5.6: Variance of $\hat{N}_o$

Z_1 and Z_2 are zero mean, we find:

$$\hat{N}_o = \frac{1}{L}\sum_{l=0}^{L} |x[l]|^2 \tag{5.2}$$

and the variance of this estimate obviously decreases with increasing L. It is convenient to show this in a simulation with $N_o = 1$. For each L, we will create 100 trials of $x[l], l \in [0, L]$. We will find the mean power over those 100 trials for each L. Figure 5.6 shows the variance of $\hat{N}_o$ as a function of L. We expect the variance to decrease at a rate $1/L$, shown as a dashed line in the plot.

By terminating the input of the PLFM receiver in a matched load and taking continuous acquisitions, we wish to see for how long we can productively integrate before imperfect stability dominates. Figure 5.7 shows the variance vs. the number of acquisitions. It is apparent that the system stability is ~ 200 acquisitions ~ 17 s real time. It should be noted that the actual stability is probably somewhat worse than this, because the preamplifier was not included in this measurement. However, even if the actual sensitivity is an order of magnitude worse (~ 2 s), then this is still $>>$ 20 ms, which is the time resolution after dedispersion determined in Section 4.2. Thus, we suspect but are not confident that stability is not a limiting factor in this experiment.

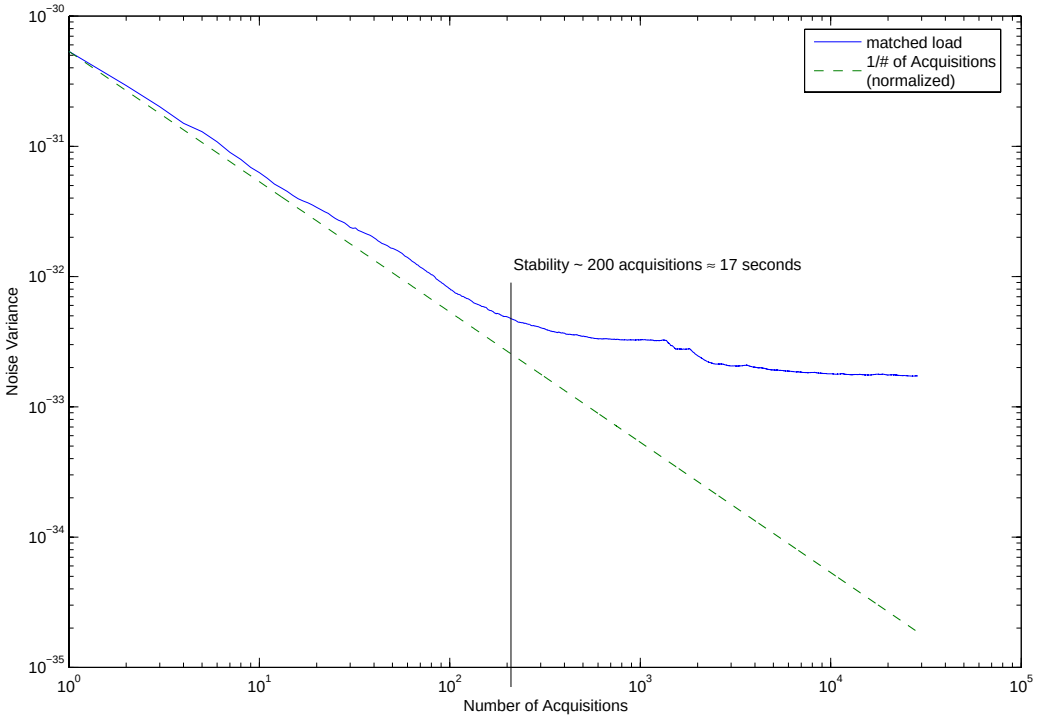

Figure 5.7: System noise variance integrating on a matched load

5.2.2 Sensitivity

In order to determine the system sensitivity, we first find the noise baseline in units of watts. After removing present RFI and compensating for the spectral baseline ripple, Figure 5.5 gives a mean noise baseline of $m_a = \sim 90$ dBW $= 10^{-9}$ W. Measuring the variance of a single acquisition, we find that $\sigma_a^2 = 1 \times 10^{-18}$ W. Using the fact that our effective collecting area is ~ 10 m^2, and that we are using $B = 18$ MHz bandwidth, we find the dedispersed pulse sensitivity before integration. The 5σ sensitivity is $S = m_a + 5\sigma_a^2 \sim 575362878.4$ Jy ~ 575 MJy. Dedispersion, a form of integration, serves to decrease noise variance. It is known from Section 4.2 that the time resolution to dispersed pulses can be as low as $\tau = 20$ ms. Now we find the pulse sensitivity after dedispersion is $\frac{S}{\sqrt{B\tau}} \sim 0.958$ MJy to 20 ms pulses. In checking for pulses which are longer than 20 ms, our sensitivity increases by $1/\sqrt{\beta}$ where the pulse length is $\beta * 20$ ms. Note that the pulse sensitivity will never decrease beyond the stability of the system.

Chapter 6

Experimental Results

In this thesis we consider a single observation made at PARI during the evening of October 23, 2004 between the times $\sim$ 21:36 and $\sim$ 21:53 UT (17:36 and 17:53 local time). PARI is located in southern North Carolina (approximately 40 miles SSW of Asheville), at 35°13'17" N and 82°18'34" W. At this time, the celestial coordinates directly overhead were right ascension 18h 14.8' and declination 35° 13.2', placing the galactic center nearly due South (Azimuth $\sim$ 182°) and $\sim$ 25° above the horizon. In Section 6.1 we consider the details of the observation. Section 6.2 presents the results of the analysis and considers the candidate detections.

6.1 Observation Details

The dataset has 13263 acquisitions at 16384 samples/acquisition, for a total acquisition time of $\sim$ 17 minutes and an effective observing time of $\sim$ 1.09 seconds. Each acquisition is written to file as a series of 8-bit samples, making each file size 128KB. The total size for all acquisitions is $\sim$ 1.62 GB.

A spectrogram which shows the time-frequency matrix of this observation is shown in Figure 6.1. Notice the streaks in both frequency and time caused by RFI. Transmissions of the state police radio are visible at $\sim$ 42.5 MHz at times $\sim$ 70 and $\sim$ 1000 seconds. The spectrogram shown in Figure 6.2 shows the result after RFI mitigation and baseline removal is performed.

6.1.1 Analysis of Results

Cordes and McLaughlin ([1],[33]) suggest a presentation of results, in the form of a 4-way plot, for interpreting the results of a dedispersion and pulse detection algorithm. Figure 6.3

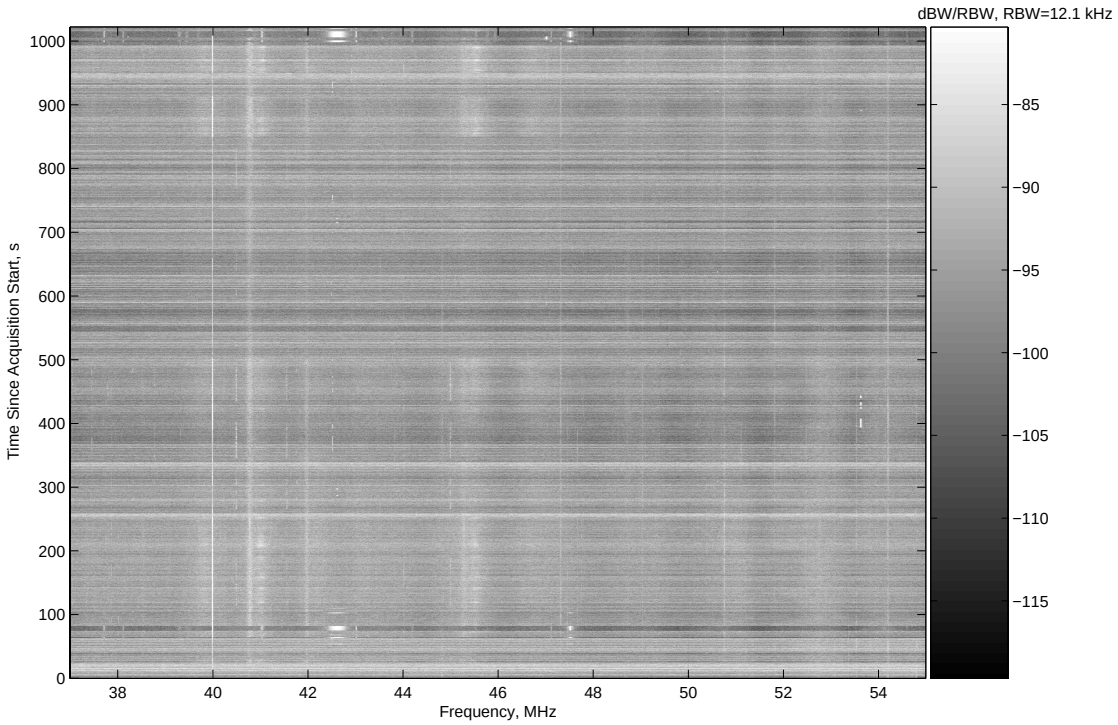

Figure 6.1: Spectrogram for observation with time-frequency resolution, 81.92μs $\times$12.21 kHz.

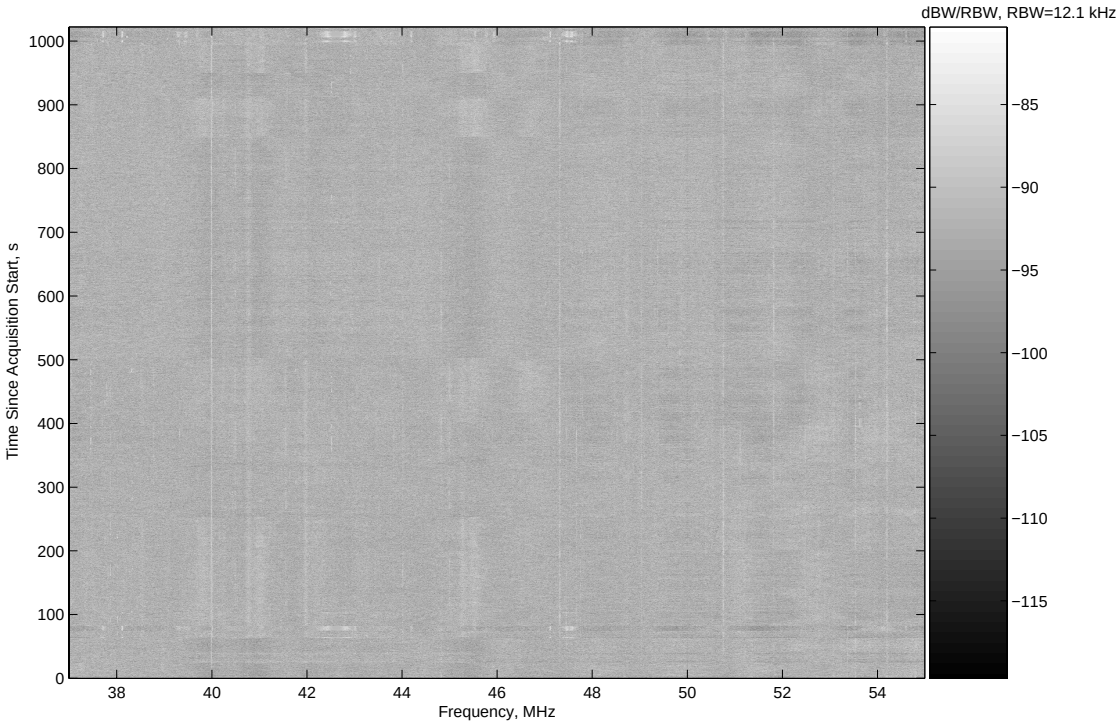

Figure 6.2: Spectrogram after RFI mitigation and baseline removal.

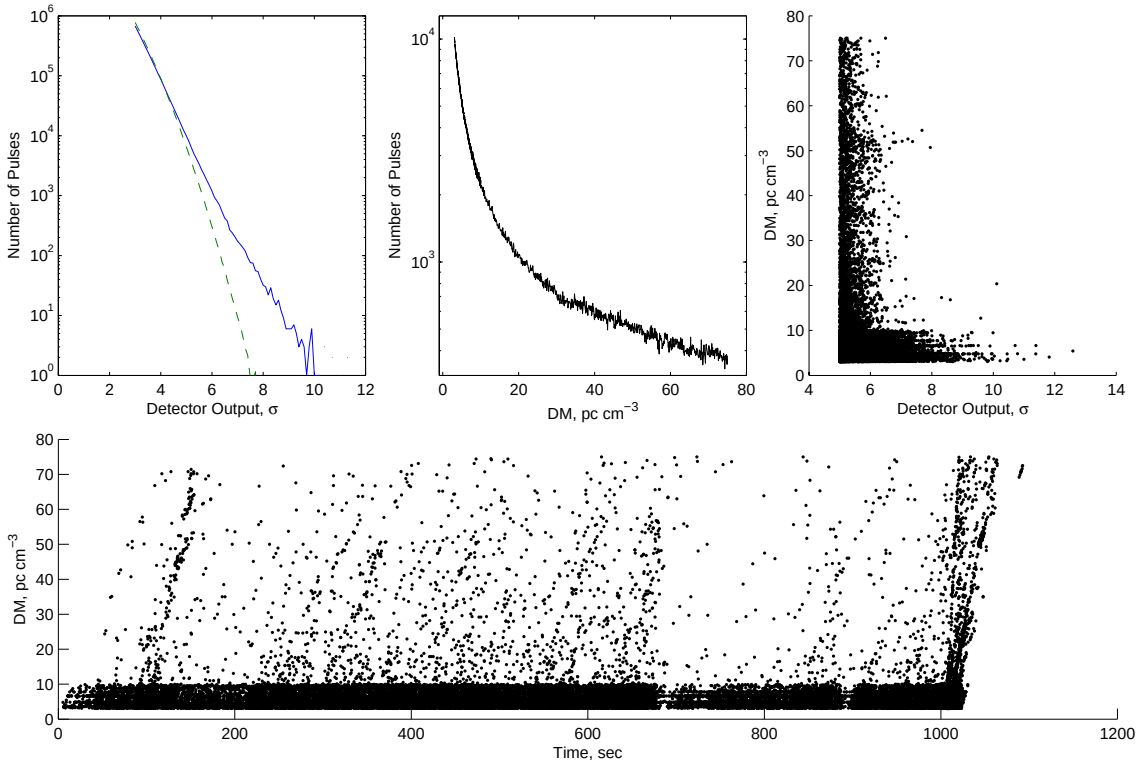

Figure 6.3: Initial analysis of observation: *Top Left Panel:* All pulses detected above 3σ vs. detector output in bins 0.1σ wide (*dashed line:* distribution based on WGN, *solid line:* distribution for this dataset), *Top Middle Panel:* all pulses detected above 3σ vs. DM in bins 0.1σ wide, *Top Right Panel:* detector output vs. DM in bins 0.1σ wide, *Bottom Panel:* all pulses detected above 5σ, time vs. DM

shows the presentation for the present dataset.

In the top left panel of Figure 6.3, the poor agreement above $\sim 4\sigma$ is attributed to increased false alarm detections at low DMs. At higher DMs, the RFI becomes 'smeared' into the noise floor; however, at low dispersion measures (in our situation $\lesssim$ 10 pc cm^{-3}), the RFI is not as thoroughly smeared and tends to cause an increased false alarm rate. The scatter of points uniformly across DM extending to $\sim 7\sigma$ in the top right panel is due to strong RFI at $\sim$ 90 and $\sim$ 1000 sec seen in the bottom panel time series. The bottom panel shows slanted streaks due to RFI at times 90, 300, 520, 600, 820, and $\sim$ 1000 sec. The streaks due to RFI are slanted because of the increased time lag introduced for increasing DM. Also evident is a greatly increased rate of detections below DM $\sim$10 pc cm^{-3}. As discussed above, much of this is attributable to RFI. This produces strong incentive to restrict attention to DM $>$ 10 pc cm^{-3} , so as to limit the number of detections for follow-up consideration to a manageable number. Figure 6.4 shows a 4 way plot for DMs $>$ 10 pc cm^{-3} . Notice in the top left panel,

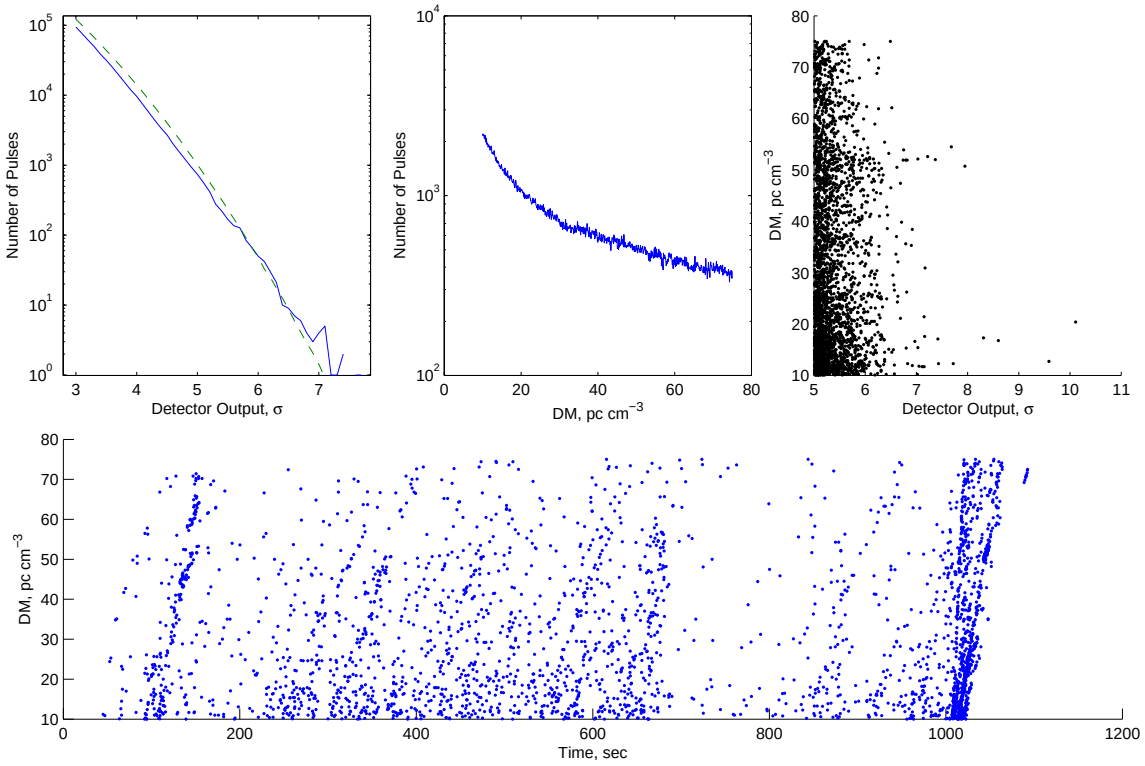

Figure 6.4: Analysis of observation with DM> 10 pc cm^{-3} : *Top Left Panel:* All pulses detected above 3σ vs. detector output in bins 0.1σ wide (*dashed line:* distribution based on WGN, *solid line:* distribution for this dataset), *Top Middle Panel:* all pulses detected above 3σ vs. DM in bins 0.1σ wide, *Top Right Panel:* detector output vs. DM in bins 0.1σ wide, *Bottom Panel:* all pulses detected above 5σ, time vs. DM

the number of pulses detected vs. the detector output is now nearly the same as that for WGN. This is another indication that the detections below DM = 10 pc cm^{-3} are the result of RFI.

Software Glitches

Another issue revealed in this stage of analysis was the presence of software glitches, leading to spurious zeroing of the data. Figure 6.5 shows the bottom panel of Figure 6.3 zoomed in showing DM $\leq$ 10 pc cm^{-3}. The glitch sympton is the horizontal streaks at a single DM. These are characteristic of a dispersed source, though upon further inspection were found to be software glitches. The problem was this: Throughout the course of data processing, there was a software issue in MATLAB which caused the dedispersed time series to be corrupted before being written to file. What happened was that for long datasets, the end of the file

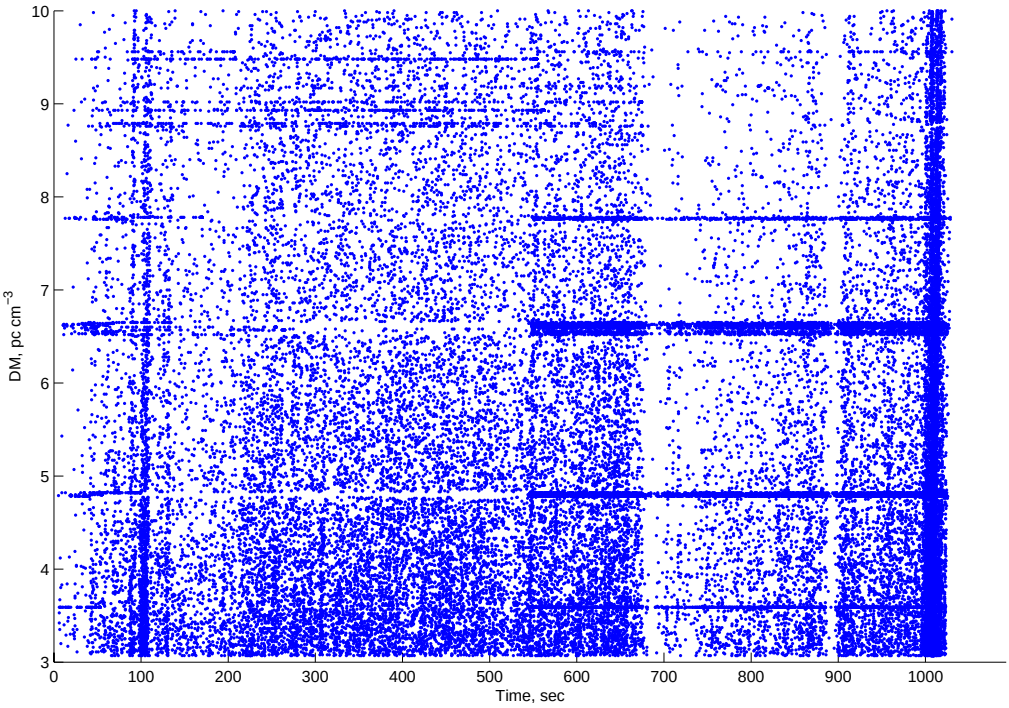

Figure 6.5: Time vs. DM for DM$<$ 10 pc cm^{-3}

would be corrupted and written as zeros. Fortunately, the glitches were readily identifiable as an anomalously large number of detections at a given DM. Because of the extraordinary computer time required to reprocess the data, as well as uncertainty in how to fix the bug, it was decided to use the 'glitchy' data but to implement an algorithm to detect and ignore affected data. The algorithm is as follows: If more than 100 detections greater than 5σ were observed at a specific DM, the dedispersed time series was inspected more closely. If the number of zeros in the time series was greater than 5% of the total number of samples, the corresponding dedispersed time series was thrown away and recomputed. Every inspected time series with greater than 100 5σ detections turned out to be a glitch. In the DM range from 3 to 10 pc cm^{-3}, glitching occurred on the average in $\sim$ 5% of the trial DMs; whereas, from 10 to 75 pc cm^{-3}, glitching occurred in less than 1% of the trial DMs. Beyond this loss of sensitivity, glitches did not cause a problem. All the figures in the remaining sections have had all glitches removed.

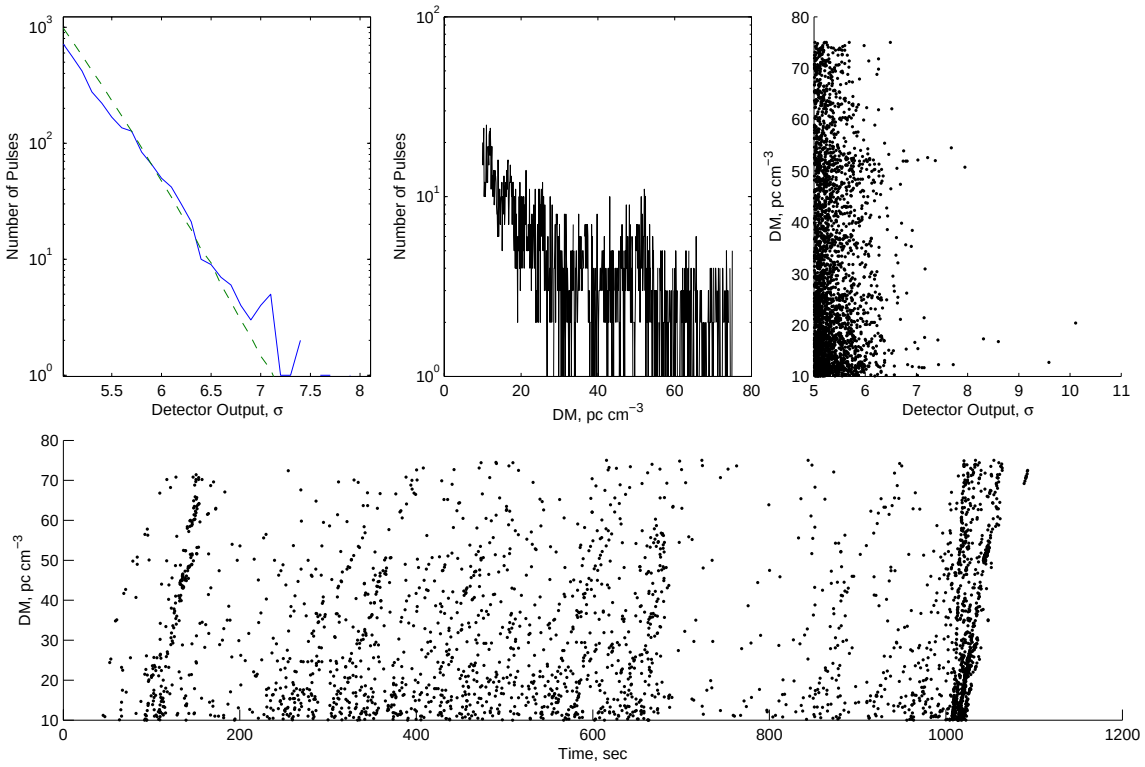

Figure 6.6: Analysis of detections $> 5\sigma$: *Top Left Panel:* All pulses detected above 5σ vs. detector output, (*dashed line:* distribution based on WGN, *solid line:* distribution for this dataset) *Top Middle Panel:* all pulses detected above 5σ vs. DM, *Top Right Panel:* detector output vs. DM, *Bottom Panel:* all pulses detected above 5σ, time vs. DM

6.2 Candidate Detections

The top two left panels of Figure 6.3 considered all detections greater than 3σ. Due to the large number of detections at this level ($\sim$ 2200), it is helpful to reconsider the 4-way plot this time plotting in the top two left panels those detections which exceed 5σ, as in Figure 6.6.

A few things are apparent in this new plot. First, note the peaks around DM= 52.1 pc cm^{-3} in the top right two panels. The peak in the top right panel corresponding to strong detections at DM$\sim$ 52 pc cm^{-3} are attributable to RFI, as will be seen in Section 6.2.4 and Figure 6.9. The peak in the middle panel, however is not so easily explainable and will be further addressed in Section 6.2.4. Also evident is a narrow peak in the middle panel at DM$\sim$ 43 pc cm^{-3} . This is further considered in Section 6.2.5. From about 200 to 700 seconds, there are a large number of detections across the range of dispersion measures. The

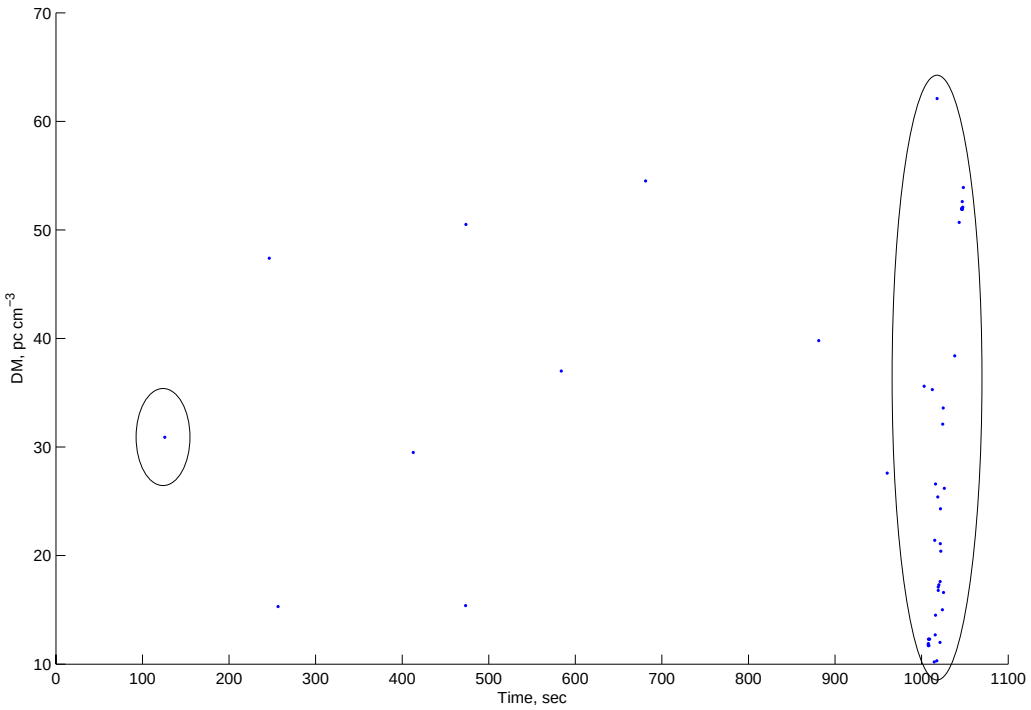

Figure 6.7: Dispersion measure vs. time for detections $> 6.5\sigma$

few slanted streaks attributable to RFI can still be seen; however, there are many detections in this realm which can't be readily attributed to interference. Section 6.2.1 considers those detections which register a detector output greater than 6.5σ, as addressed in Section 5.1.2.

Another interesting observation is along the time scale from ~ 675 to ~ 800 seconds. This section appears to be almost completely free from interference or other sources. While there are a few candidate detections above 5σ in this region, there are remarkably fewer than in other regions of time. This suggests that RFI accounts for most (if not all) of our detections. Clearly, more stringent criteria are needed to discriminate between RFI and astrophysical pulses.

6.2.1 Follow-up Analysis of Detected Pulses

An interesting result comes from reproducing the DM vs. time plot for different thresholds (i.e. plotting only the detections which register greater than some σ_t above the mean). In Section 5.1.2, a threshold for further consideration was set at 6.5σ. Figure 6.7 shows DM vs. time for this threshold.

Table 6.1: Summary of Detected Pulses $> 6.5\sigma$

Detector Output, σ	DM, pc cm^{-3}	Approx. Time, UT	Dedispersed Pulse Length (ms)
7.68	54.5 ± 0.7	21:48:15	22.0
7.03	15.4 ± 0.2	21:44:47	6.2
6.80	15.3 ± 0.2	21:41:10	6.2
6.71	39.8 ± 0.4	21:51:35	16.2
6.69	47.4 ± 0.5	21:41:00	19.2
6.62	50.5 ± 0.5	21:44:47	20.4
6.61	37.0 ± 0.4	21:46:37	15.0
6.56	27.6 ± 0.3	21:52:54	11.2
6.54	29.5 ± 0.4	21:43:46	12.0

There is still some strong interference left, but it is mostly isolated to > 1000 seconds. In the plot, those detections which are circled are attributed to RFI (or more precisely the police radio communication). A handful of possible detections are still left, and Table 6.1 summarizes the characteristics of these 9 detections. Note that all detections resided in only 1 time bin.

We wish to consider whether any of these detections can be attributed to known sources of transient RF emission (i.e. pulsars or GRBs). For this section, we consider sources which are located inside a circle centered at the zenith within a cone 70° (20° elevation with respect to the horizon at PARI), corresponding to the 3 dB beamwidth of the antenna.

6.2.2 Investigation of Possible GRB Associations

We would first like to consider the possibility of detection of a prompt emission coincident with a GRB. In his search for low-frequency emissions coincident with GRBs, Balsano [21] derives that the DM due to the intergalactic plasma (i.e. beyond the Milky Way Galaxy at asymptotic redshifts) is $DM_{IGP} \approx 600 \times z$ where z is redshift. It is known that all parts of the Universe are streaming away from each other (i.e. the Universe is expanding), and the consequent Doppler shift of a detected transient due to this expansion is quantified by the redshift. The higher the redshift, the more distant the source. Meszaros [34] indicates that emissions with redshifts as high as $z \sim 30$ may be detectable in x-rays and γ-rays. Using this value, an asymptotic intergalactic DM can be derived as $DM \sim 18000$. Thus, any detected GRB would correspond to a radio emission with DM < 18000. This places a constraint on the time delay due to dispersion for a detectable radio prompt emission from the GRB, using Equation 4.3. Consequently, at the PLFM center frequency of 46 MHz, the time delay for

the radio emission due to an asymptotic redshifted GRB is $\delta t <\sim 10$ hr.

In order to investigate the possibility of a GRB association with any of our detected dispersed pulses, we must determine if any GRBs were detected within ~ 10 hours of the observation window. NASA maintains the Gamma Ray Bursts Coordinates Network (GCN) which, upon detection of a GRB by one of the associated satellites, updates its online catalog in real time. The catalogs are found at the GCN webpage[1]. According to the GCN, no GRBs were detected within 10 hours of our observation window, so this is ruled out as the cause of any of our detections.

6.2.3 Investigation of Possible Pulsar Associations

The Australia Telescope National Facility (ATNF) maintains a database of all known pulsars[2] [35]. This catalog was used to identify pulsars which are within the DM error of each detection in Table 6.1, with results summarized in Tables 6.2 - 6.3 for each detection. Possible sources are given in order of decreasing elevation. Sources for which the 400 MHz flux density is not known are marked with a '$*$'.

As noted before, giant pulses (GPs) from several GP-emitting pulsars were discovered simply by accident. Due to these serendipitous discoveries, it is appropriate to consider pulsars which were within view during the time of observation, as it may turn out that one of these pulsars emits giant pulses. Above 20° elevation, 18 pulsars were in the field of view and correspond to the DM of a detection.

It is known that the radio spectra of slow-period pulsars generally have a low-frequency turn-over, with a break frequency, $\nu_{max} \sim 120P^{-0.36}$ [36], where ν_{max} is frequency in MHz and P is period in seconds. However, during 102 and 111 MHz observations of 30 pulsars with millisecond periods (all with break frequencies expected to be > 350 MHz), Kuzmin and Losovsky [37] note that only 1 of the pulsars exhibits a low-frequency spectral turn-over. Their observations indicate that the spectra of millisecond pulsars (MSPs) can be described without a break frequency by a single power law $\propto \nu^{\alpha}$ with the spectral index, α, ranging from -1.2 to -3.3 with a mean, $\bar{\alpha} = -1.7 \pm 0.3$. This is promising, as it would indicate a possibly significant flux at 46 MHz.

Knowing that *at least* 2 GP-emitting pulsars emit pulses which are greater than 10,000 to 100,000 times the mean pulse intensity (B0531+21, P_0=33.1 ms; B1937+21, P_0=1.6 ms), we can determine the likelihood that GPs from one of the MSPs in Tables 6.2 and 6.3 could be detectable. Table 6.4 considers the extrapolated 46 MHz flux using $\bar{\alpha} = -2$ as well as $\alpha = -3.5$ which is known to be the spectral index of PSR J1959+2048 ($\alpha = -3.5 \pm 0.5$, [38]). In addition, giant pulses from this MSP *have* been detected at 129 times the mean pulse intensity at 610 MHz [16]. It is entirely possible that the pulsar emits GPs which are

[1] http://gcn.gsfc.nasa.gov/burst_info.html/

[2] http://www.atnf.csiro.au/research/pulsar/psrcat/

Table 6.2: Possible Pulsar Associations

Detector Output (σ)	Possible Source PSRJ	DM (pc cm^{-3})	RA (hh:mm:ss)	Dec (dd:mm:ss)	Elevation (°)	400 MHz Flux (mJy)	Period (s)
6.71		39.80 ± 0.4					
-	J2046+1540	39.84	20:46:39	15:40:33	50.7	11.5	1.14
6.69		47.40 ± 0.5					
-	J1721-2457	47.76	17:21:05	-24:57:06	28.5	*	0.00350
6.62		50.50 ± 0.5					
-	J2040+1657	50.70	20:40:17	16:57:30	52.7	0.6	0.866
-	J1752-2806	50.37	17:52:58	-28:06:37	26.5	1100.0	0.563
-	J1941-2602	50.03	19:41:00	-26:02:05	25.4	13.0	0.403
-	J1823-3106	50.24	18:23:46	-31:06:49	23.6	36.0	0.284
6.61		37.00 ± 0.4					
-	J2205+1444	36.72	22:05:17	14:44:31	34.6	1.5	0.938

Table 6.3: Possible Pulsar Associations *(cont.)*

Detector Output (σ)	Possible Source PSRJ	DM (pc cm^{-3})	RA (hh:mm:ss)	Dec (dd:mm:ss)	Elevation (°)	400 MHz Flux (mJy)	Period, P_0 (s)
6.56		27.60 ± 0.4					
-	J1920+2650	27.62	19:20:38	26:50:38	73.5	6.0	0.786
-	J1918+1444	27.20	19:18:23	14:45:06	64.9	1.6	1.18
-	J1848+0647	27.90	18:48:56	06:47:31	60.5	2.3	0.506
-	J1641-2347	27.70	16:41:18	-23:47:36	27	*	1.09
6.54		29.50 ± 0.4					
-	J1741+2758	29.30	17:41:53	27:58:09	80.0	3.0	1.36
-	J1641+3627B	29.50	16:41:41	36:27	71.3	*	0.00350
-	J1959+2048	29.12	19:59:36	20:48:15	62.7	20.0	0.00161
-	J1518+0205B	29.47	15:18:31	02:05:15	37.6	0.5	0.00795
-	J1518+0205C	29.30	15:18:33	02:04:58	37.6	*	0.00248
-	J1518+0205D	29.30	15:18:33	02:04:58	37.6	*	0.00299
-	J1518+0205E	29.30	15:18:33	02:04:58	37.6	*	0.00318
-	J2215+1538	29.26	22:15:39	15:38:34	32.9	3.7	0.374
-	J2253+1516	29.18	22:53:14	15:16:37	25.1	2.4	0.792

Table 6.4: Possible GP flux for 2 MSPs

PSRJ	400 MHz flux (mJy)	46 MHz flux $\alpha = -3.5$, (Jy)	GP flux $\beta = 5$, (MJy)
J1959+2048	20.0	39	3.9
J1518+0205B	0.5	.970	.097

on occasion far stronger than this which have yet to be detected, as was the case with the pulsars B1937+21 and B0531+21 (see Section 2.1.4). Table 6.4 also considers the possible GP flux using $\beta = 5$, ($S_{GP} = S_{46} \cdot 10^{\beta}$ where S_{GP} is the giant pulse flux and S_{46} is the 46 MHz flux).

Examining Table 6.4, GPs from PSR J1959+2048 would be detectable with β slightly less than 5, assuming pulse durations ≥ 20 ms. GPs from J1518+0205B, however, would still be undetectable with the current PLFM sensitivity.

As many of the MSPs do not have a listed 400 MHz flux, it is useful to determine a flux density necessary to have GPs which are detectable by the PLFM instrument. For this measurement, we will use a detectable flux limit at 46 MHz equal to 1 MJy. In this case, a 46 MHz mean pulse flux of 10 Jy would allow very strong GPs with $\beta = 5$ to be detectable.

Every non-MSP pulsar in Tables 6.2 and 6.3 is expected to have a low-frequency spectral turnover above ~ 107 MHz ($P_{0,max} = 1.36$ s). While the possibility of GPs from these other pulsars detectable by the current PLFM instrument isn't null, we feel source localization is necessary to make any kind of associations. This will be regarded as a requirement for an expanded PLFM instrument.

6.2.4 Pulse Train Detection at DM~ 52.1 pc cm^{-3}

Perhaps the most interesting of the detections seen in Figure 6.6 are those occurring near DM= 52.1 pc cm^{-3} since these are seen to be more frequent than pulses occurring at other DMs. Most promising is the peak in the top middle panel of Figure 6.6, reproduced in Figure 6.8. For Figures 6.8 - 6.15, we have dedispersed the acquisitions on a finer than optimal DM grid in steps of 0.1 pc cm^{-3} to show slight variations.

No glitches (see Section 6.1.1) occurred in this range of dispersion measures ($\sim 50 - 53$ pc cm^{-3}), so this is ruled out as the source of the pulses. Figure 6.9 shows individual detections above 5σ for dispersion measures between 51.7 and 52.7 pc cm^{-3}. Figure 6.10 shows the dedispersed time series for the observation at DM= 52.1 pc cm^{-3}. Examining the time series, the interference due to the police radio at ~ 1020 and ~ 1040 s can be seen. In addition, there are five distinct detections, four of which exceed 5σ. Although the pulses are

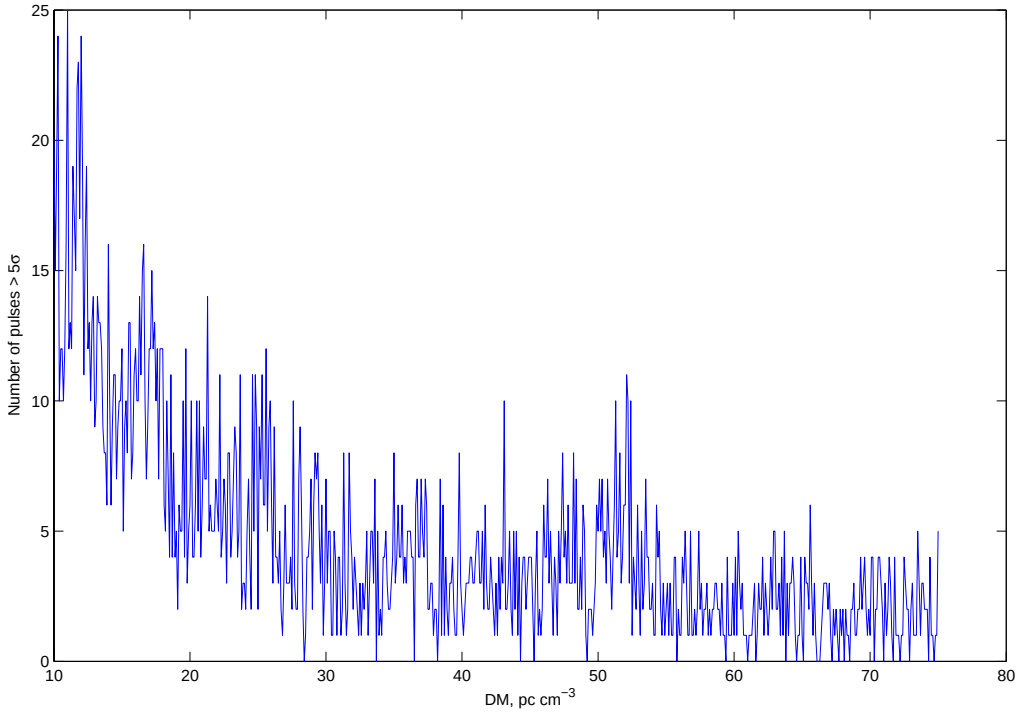

Figure 6.8: Plot of dispersion measure vs. number of pulses with a greater than 5σ detection

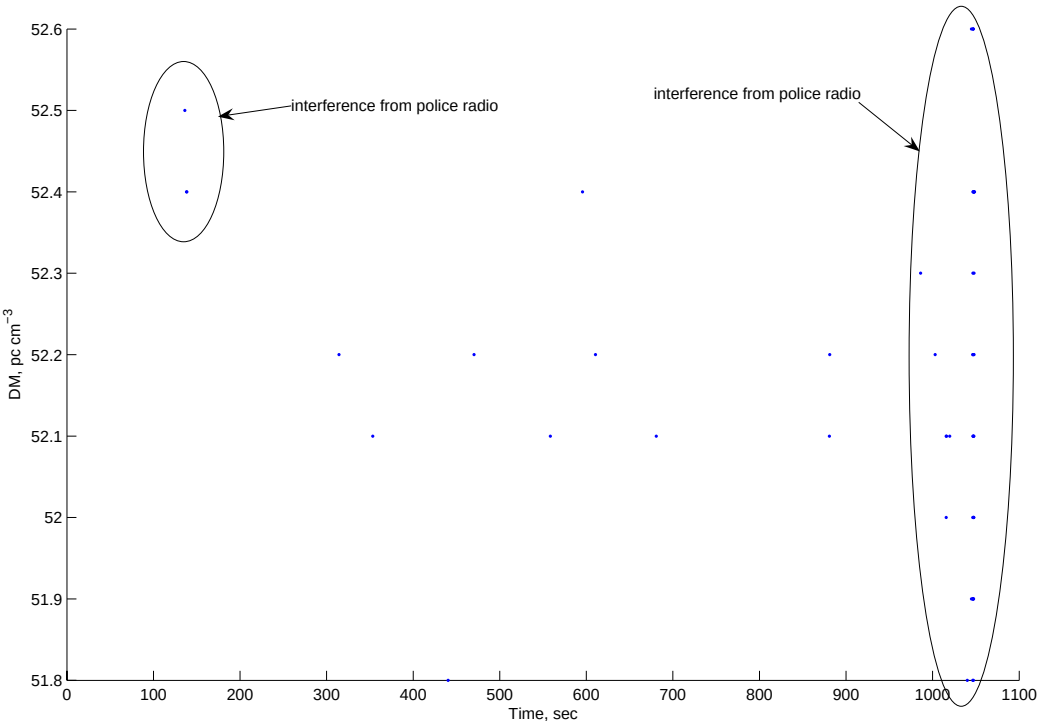

Figure 6.9: Time vs. DM zoomed in showing individual detections $> 5\sigma$

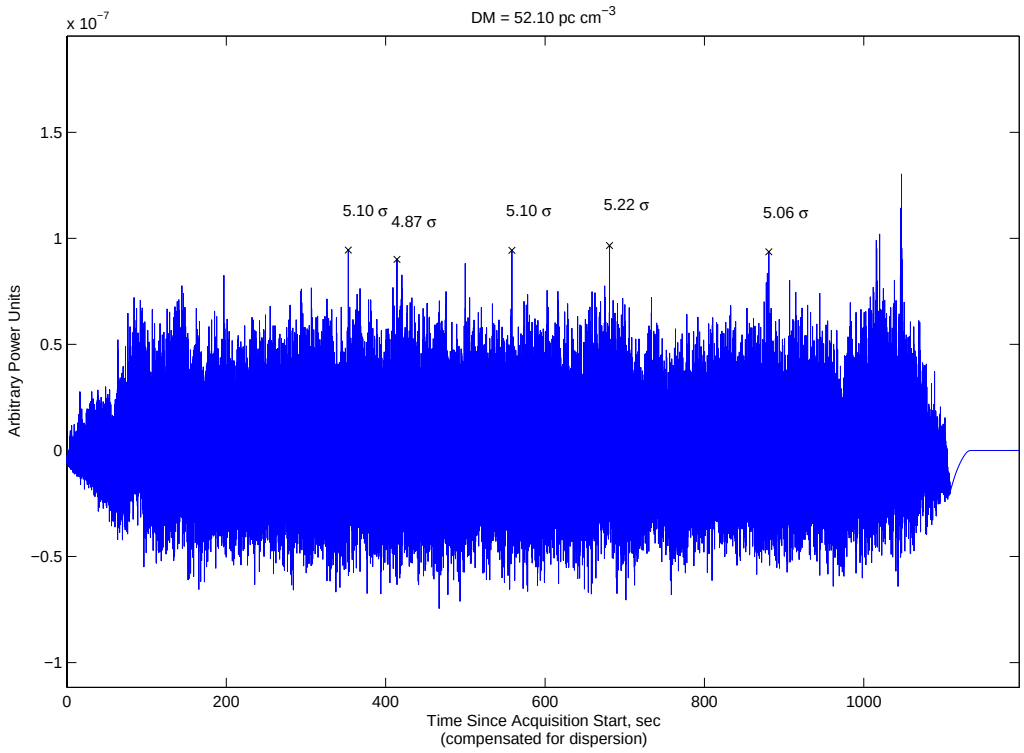

Figure 6.10: Dedispersed time series for DM= 52.1 pc cm^{-3}

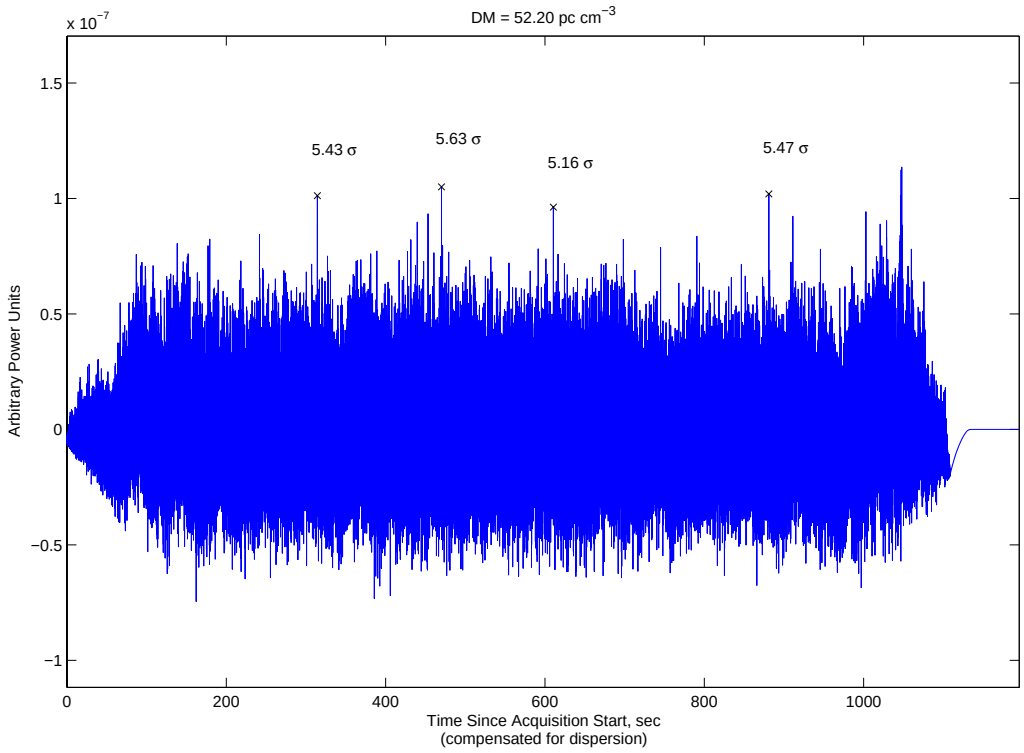

Figure 6.11: Dedispersed time series for DM= 52.2 pc cm^{-3}

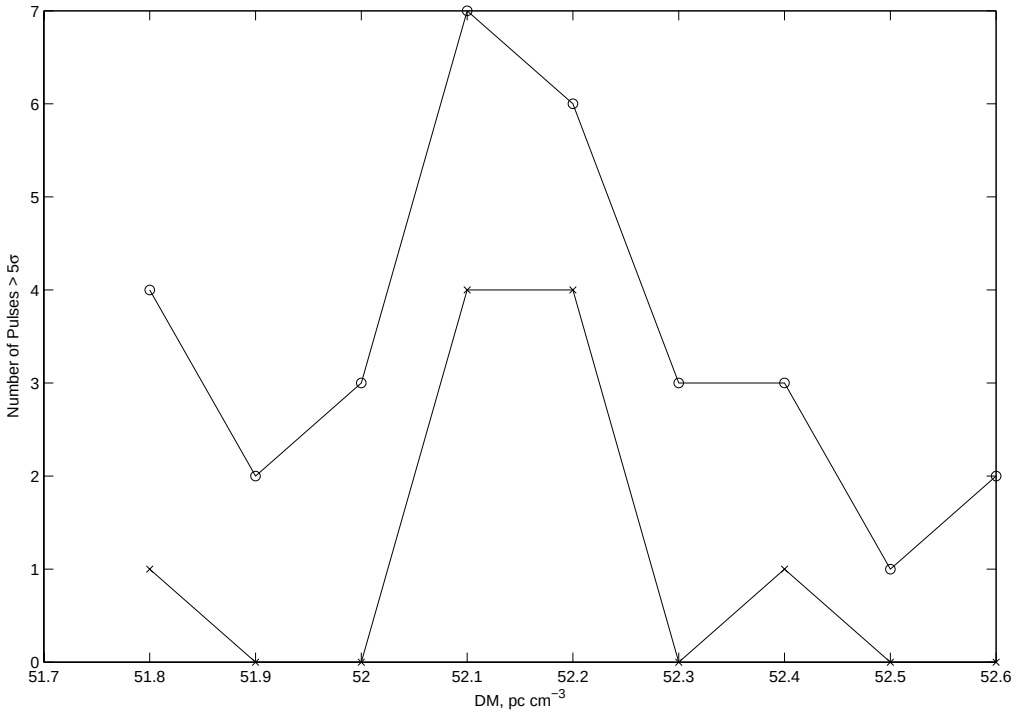

Figure 6.12: Dispersion measure vs. number of pulses for DM= 51.7 to 52.7 pc cm^{-3}

individually $< 6.5\sigma$, their apparent clustering in time may be significant.

Further evidence that this event may be significant is an excess of pulses at DM = 52.2 pc cm^{-3} as well, as seen in Figure 6.12. Figure 6.11 shows the dedispersed time series for DM= 52.2 pc cm^{-3}. Negating the contribution of the state police radio to the excess pulses, 4 pulses greater than 5σ are also evident at DM = 52.2 pc cm^{-3} . While these detections can not be correlated with any sources above the horizon at the time of observation, this is certainly an interesting phenomenon which should be noted.

6.2.5 Pulse Train Detection at DM$\sim$ 43.1 pc cm^{-3}

Figure 6.8 shows a narrow peak at DM= 43.1 pc cm^{-3}. No glitches occurred in this DM range, so this is ruled out as a source of the detections. The dedispersed time series is shown in Figure 6.13. The first marked detection at $\sim$ 135 seconds is due to strong RFI, while the remaining detections cannot be easily ruled out as due to interference. Figures 6.14 shows DM vs. time for DMs between 42.8 and 43.4 pc cm^{-3} , and 6.15 shows the number of excess pulses at DM = 43.1 pc cm^{-3} . One possible source of the frequent pulses is PSR J1650-1654

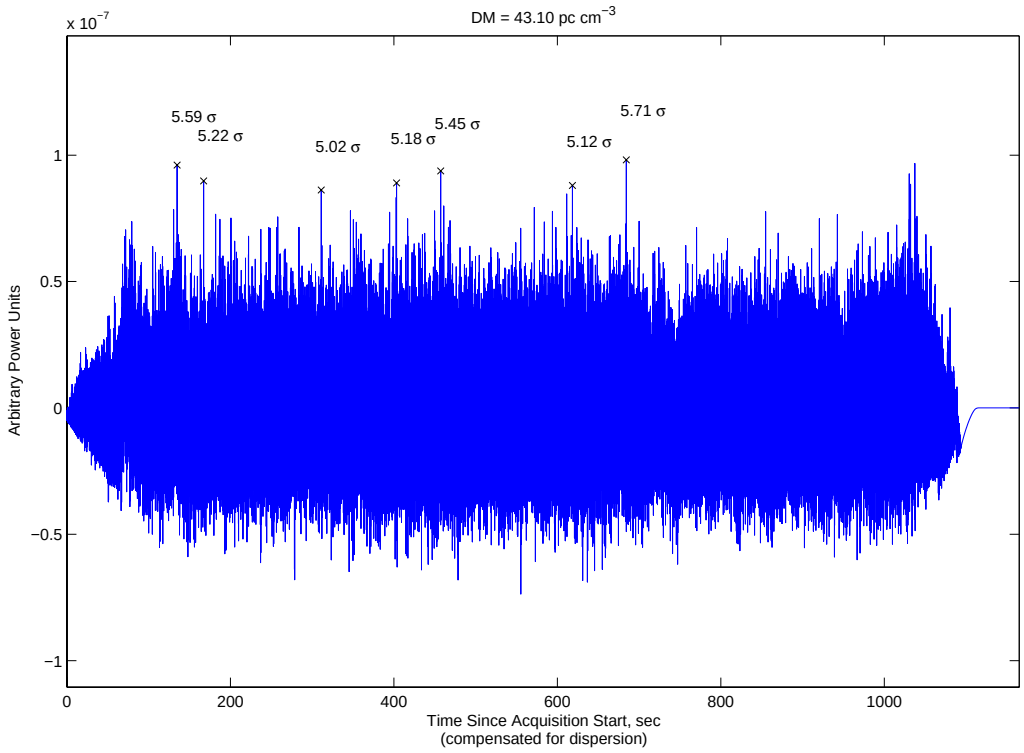

Figure 6.13: Dedispersed time series for DM= 43.1 pc cm^{-3}

[39], with DM= 43.25 pc cm^{-3} . This pulsar was located at an elevation of 34.2° from the horizon at the time of observation, still within the 3 dB beamwidth points. With a period of $\sim$ 1.75 s, a low-frequency spectral turnover is expected at $\sim$ 98 MHz. An estimated 400 MHz flux of 13 mJy would indicate a 46 MHz flux on the order of $\sim$ 1 Jy, slightly lower assuming a spectral turnover. While this flux is well below the PLFM sensitivity, the possibility of the detection of GPs cannot be ruled out. Again, expanded future experiments will be able to further investigate this apparent clustering of detections.

6.3 Summary

A pilot survey at PARI has been conducted, demonstrating the operation of the designed receiver and data analysis algorithms. The detection of 9 dispersed pulses has shown the need for improved RFI mitigation techniques in order to be more confident about ruling this out as a source of the detections. Apparent clusterings of dispersed pulses have been seen at 3 dispersion measures; DM = 43.1, 52.1, and 52.2 pc cm^{-3} ; and these are perhaps the most interesting of the detections made during the experiment. It is desired that future

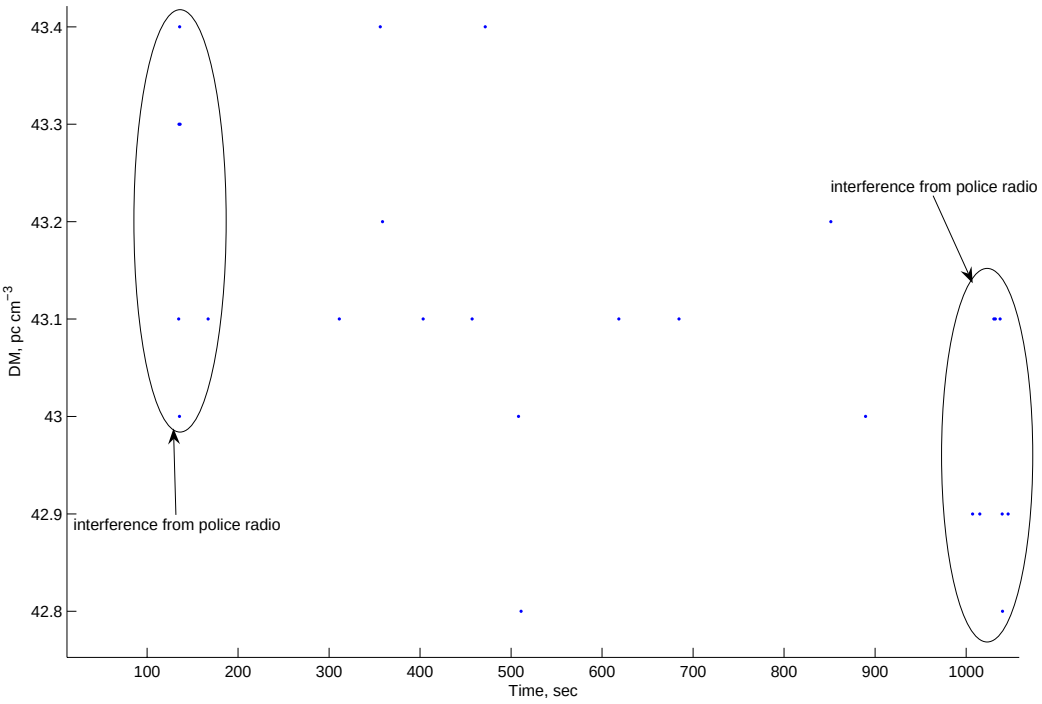

Figure 6.14: Time vs. DM showing clustering of detections at DM= 43.1 pc cm^{-3}

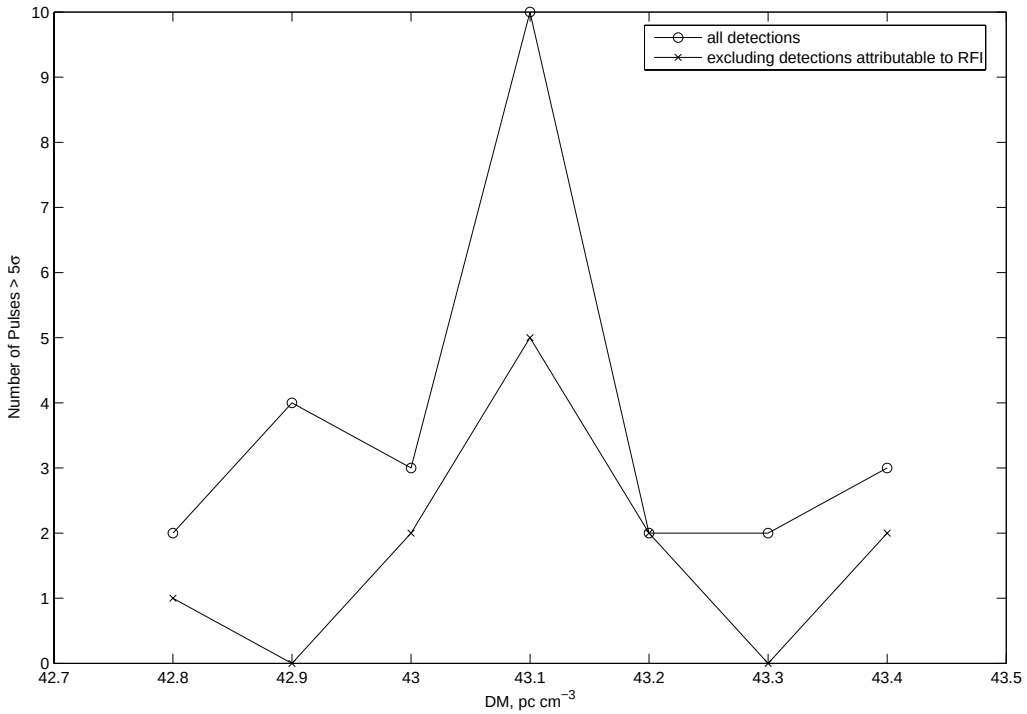

Figure 6.15: Dispersion measure vs. number of pulses for DM= 42.8 to 43.4 pc cm^{-3}

experiments will be able to follow-up on these, quite possibly astrophysical, phenomena.

Chapter 7

Conclusions

This thesis describes the development and first use of a low frequency astronomical transient search instrument. A pilot survey consisting of a single 20 min observation demonstrated the operation of the RFI mitigation, dedispersion, and pulse detection algorithms. The detection of 9 transients above 6.5σ and detected pulse trains at DM= 52.1, 52.2, and 43.1 pc cm^{-3} were considered, showing the possible scientific payoff of a low-sensitivity all-sky monitor. Future observations with an all-sky monitor will be necessary to determine the possibility of an astrophysical source at these dispersion measures. All detections are unverifiable without source localization and future observations, however they demonstrate the necessity for future studies to further expand this parameter space in terms of sensitivity and stability. Source localization will be able to pinpoint any detected source of emission. It has become apparent that one of the most important parts of a low-frequency survey is the ability to discimrinate against RFI, as this was one of the limiting factors in our experiment. It has been noted that most (if not all) of our detections can probably be attributed to RFI.

Improvements to future experiments are many. First, increased observing time is a necessity. Even during our short observation, some interesting detections were made. Future observations at the experiment site will be able to further explore the exciting possibilities of an all-sky monitor. Next, increased sensitivity would be useful. An immediate and dramatic improvement in sensitivity could be obtained by implementing continuous (duty cycle $\sim 100\%$) acquisitions, improved from the current $\sim 0.15\%$. Further significant improvement would require multiple antennas, as this would vastly increase sensitivity while providing the ability to localize sources and improve the ability to make associations. While calibration wasn't entirely necessary with the use of a single antenna, future studies may include phased arrays, which demand the need for calibration. The Crab pulsar offers an excellent possibility for this, though our sensitivity would have detected only a few of its giant pulses, probably not enough for calibration.

For this thesis, we have developed a transient search instrument which served to 'scratch the surface' on the possibilities for an all-sky monitor. A wide-bandwidth receiver with high

frequency resolution was traded off for one with increased time resolution, while sensitivity was traded off for increased sky coverage. We have demonstrated the instrument's operation with an observation made at PARI, making use of RFI mitigation and dedispersion algorithms. A handful of possible astrophysical detections were obtained, though clearly improved RFI mitigation routines must be employed in future experiments. An expanded PLFM survey is planned, utilizing 12 dual-polarized dipoles at the same site, where the limitations determined in this thesis will be addressed.

Appendix A

Galactic Background Intensity

Galactic noise can be described in terms of its intensity, I_ν, having units W m^{-2} Hz^{-1} sr^{-1}, integrated over the antenna pattern [27]. The Galactic noise intensity is quantified by Cane in [40] based on observations of the Galactic polar regions at 5.2, 9.0, 15.6, and 23.0 MHz. Her measurements indicate the following relationship between frequency and intensity:

$$I_\nu = I_g \nu^{-0.52} \frac{1 - e^{-\tau(\nu)}}{\tau(\nu)} + I_{eg} \nu^{-0.80} e^{-\tau(\nu)} \text{ W m}^{-2} \text{ Hz}^{-1} \text{ sr}^{-1} \tag{A.1}$$

where $I_g = 2.48 \times 10^{-20}$, $I_{eg} = 1.06 \times 10^{-20}$, $\tau(\nu) = 5.0\nu^{-2.1}$, and ν is in MHz. In A.1, the first term is due to the noise contribution by the Galaxy while the second term is due to extragalactic noise, assumed to be spatially uniform [27]. The spectrum turns over at about 3 MHz, and a high frequency approximation is given by (A.2) as in [27]. The expressions (A.1) and (A.2) are shown in Figure A.1.

$$I_\nu \approx I_g \nu^{-0.52} + I_{eg} \nu^{-0.80} \text{ W m}^{-2} \text{ Hz}^{-1} \text{ sr}^{-1} \tag{A.2}$$

The power spectral density of the Galactic noise can be found by integrating intensity over the antenna pattern, as in (A.3).

$$S_a = \frac{1}{2} \int I_\nu A_e \, d\Omega \tag{A.3}$$

where A_e is the effective antenna aperture, and the $\frac{1}{2}$ accounts for the fact that the single-polarization antenna receives only about one half the unpolarized Galactic noise. Considering the antenna used here has a very broad beamwidth, and making the assumption that the antenna gain is very small at and below the horizon (verified in [27]), (A.3) can be reduced to (A.4) [27].

$$S_a \approx \frac{1}{2} I_\nu A_e \Omega \tag{A.4}$$

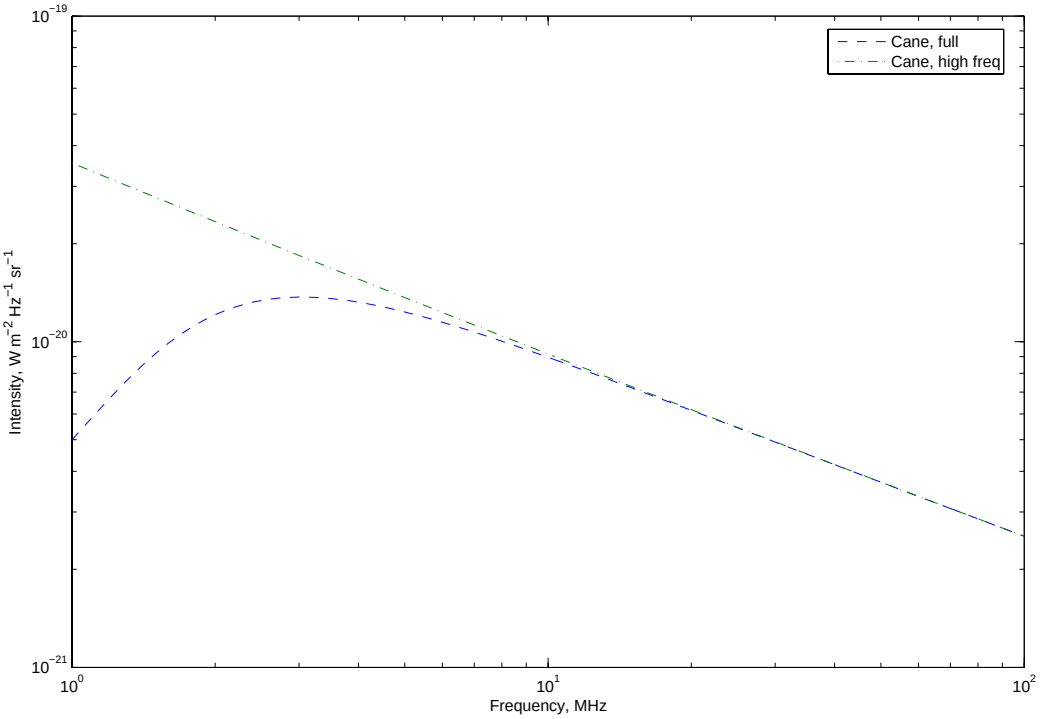

Figure A.1: Galactic noise intensity as given by [40] and [27]

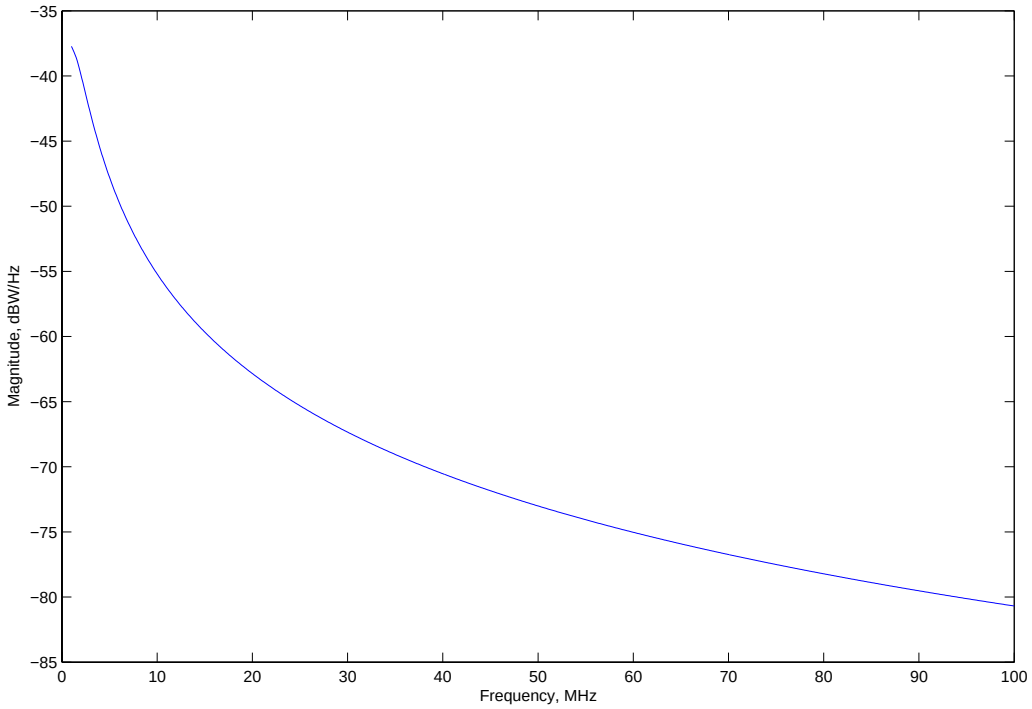

Figure A.2: Power spectral density of Galactic Background Noise referenced to the Antenna Terminals

where Ω is beam solid angle. The diurnal variation in I_ν caused by different regions of the galaxy intercepting the antenna beam yields as much uncertainty in (A.3) as the approximation used to obtain (A.4) [27], so it is not an unreasonable estimate.

Using the antenna parameters in Section 3.2.1 for A_e and Ω, we obtain the power spectral density of the Galactic noise, as seen at the antenna terminals (Figure A.2).

Appendix B

Dispersion Theory

In this appendix, we attempt to understand the dispersion of EM radiation as it travels through the ISM. The ISM consists mainly of ionized hydrogen, free electrons, and mostly immobile positive ions. Propagation through this medium introduces a time delay between high and low frequencies and is well understood. The problem of dispersion is worked out in many textbooks and is included here for completeness.

Beginning with Maxwell's equations, as in [21], we attempt to find the speed at which EM radiation propagates through the ISM plasma.

$$\begin{aligned} \vec{\nabla} \cdot \vec{E} &= \rho \\ \vec{\nabla} \times \vec{E} &= \frac{-1}{c} \frac{\partial \vec{B}}{\partial t} \\ \vec{\nabla} \cdot \vec{B} &= 0 \\ \vec{\nabla} \times \vec{B} &= \frac{4\pi}{c} \vec{J} + \frac{1}{c} \frac{\partial \vec{E}}{\partial t} \end{aligned} \tag{B.1}$$

Assuming the spacetime dependence $e^{-j(-\vec{k}\cdot\vec{x}+\omega t)}$ for $\vec{E}$ and $\vec{B}$, all the derivatives may be eliminated, i.e. $\partial/\partial t \rightarrow -j\omega$, $\vec{\nabla}\times \rightarrow j\vec{k}\times$, and $\vec{\nabla}\cdot \rightarrow j\vec{k}\cdot$.

While the current density, $\vec{J}$, in B.1 must be obtained, we neglect the source term ρ as the plasma is electrically neutral overall. As in [21], we assume that the positive charges are essentially immobile due to their mass and consider only negative charges. Ignoring magnetic force and applying Newton's Second Law to an electron, we obtain

$$m\vec{a} = -e\vec{E} \ . \tag{B.2}$$

We obtain the electron's velocity and acceleration by assuming its position is given by $\vec{x} = \vec{x_o} e^{-j\omega t}$.

$$\vec{v} = -j\omega\vec{x} \tag{B.3}$$

$$\vec{a} = -\omega^2\vec{x} \tag{B.4}$$

Substituting (B.4) into (B.2), we find

$$-\omega^2 m\vec{x} = -e\vec{E} \tag{B.5}$$

Again as in [21] we assume the plasma is ohmic, such that $\vec{J} = \sigma\vec{E}$, where the current is given by

$$\vec{J} = -ne\vec{v} \ . \tag{B.6}$$

In B.6, n is free electron density, $-e$ is electron charge, and $\vec{v}$ is electron velocity. Substituting (B.3) and (B.5) into (B.6) gives

$$\vec{J} = \frac{jne^2}{m\omega}\vec{E} \ , \tag{B.7}$$

so that

$$\sigma = \frac{jne^2}{m\omega} \ . \tag{B.8}$$

We can now rewrite the curl equations in (B.1), obtaining

$$j\vec{k} \times \vec{E} = \frac{j\omega}{c}\vec{B} \tag{B.9}$$

$$j\vec{k} \times \vec{B} = \left(\frac{4\pi\sigma}{c} - \frac{j\omega}{c}\right)\vec{E} \ . \tag{B.10}$$

Taking $\vec{k}\times$ (B.9) and substituting in (B.10) gives

$$\begin{aligned} -k^2\vec{E} &= \frac{\omega}{c}k \times \vec{B} \\ -k^2\vec{E} &= \frac{\omega}{c}\left(\frac{4\pi\sigma}{jc}\vec{E} - \frac{\omega}{c}\vec{E}\right) \\ k^2 &= \left(\frac{\omega^2}{c^2} - \frac{4\pi ne^2}{mc^2}\right) \end{aligned} \tag{B.11}$$

As in [21], we now define a plasma frequency, ω_p.

$$\omega_p^2 \equiv \frac{4\pi ne^2}{m} \ , \tag{B.12}$$

which reduces (B.11) to

$$k^2 = \frac{\omega^2}{c^2}\left(1 - \frac{\omega_p^2}{\omega^2}\right) \ . \tag{B.13}$$

Let us now define the group velocity, in order to compare the rates at which different frequencies propagate.

$$v_{gr} \equiv \frac{d\omega}{dk} = c\left(1 - \frac{\omega_p^2}{\omega^2}\right)^{1/2} \ . \tag{B.14}$$

Balsano ([21]) gives the time it takes for radiation to reach an observer as

$$t = \int_0^L \frac{dz}{v_{gr}} \ . \tag{B.15}$$

The integral is to allow for changes in the electron density along the line of sight. If we assume $\omega^2 >> \omega_p^2$, we can expand $1/v_{gr}$.

$$\begin{aligned} t &\approx \int_0^L \frac{dz}{c}\left(1 + \frac{\omega_p^2}{2\omega^2}\right) \\ &= \frac{L}{c} + \frac{1}{2c\omega^2}\int_0^L \omega_p^2\, dz \\ &= t_o + \frac{2\pi e^2}{mc\omega^2}\int_0^L n\, dz \ . \end{aligned} \tag{B.16}$$

The second term in B.16 is the interesting quantity, the frequency dependence of arrival times of the radio emission [21].

$$\Delta t = \frac{2\pi e^2}{mc\omega^2}\int_0^L n\, dz \tag{B.17}$$

with $\Delta t = t - t_o$. Now we introduce dispersion measure

$$\mathrm{DM} \ = \int_0^L \ \mathrm{n}_e(\mathrm{z}) \ \mathrm{dz}, \tag{B.18}$$

and dispersion constant,

$$\alpha_d = \frac{2\pi mc}{e^2} = 2.4 \times 10^{-16} \text{ pc cm}^{-3} \text{ sec.} \tag{B.19}$$

We also switch from angular frequency in rad/sec to a frequency in Hz, such that (B.17) becomes

$$\Delta t = \frac{\mathrm{DM}}{\alpha_d \nu^2} \ . \tag{B.20}$$

So, time delay due to dispersion goes as $1/\nu^2$.

Appendix C

System Components Configuration

This appendix provides some additional details on the system components and their configuration. A simplified block diagram of the receiver unit is shown in Figure C.1.

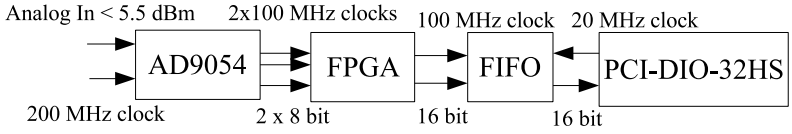

Figure C.1: Block diagram of ADC to PC, taken from [30]

C.1 PCI-DIO32HS PC Card

The data acquisition card used in the PC is the National Instruments PCI-DIO-32HS DAQ card and is listed in Table C.2 as (8). This card allows for multiple data transfer rates, with speeds limited to 13.3 MB/sec for pattern I/O and 76 MB/sec in burst mode [41]. Handshaking on the PCI-DIO-32HS is full, two-way and allows for six different timing protocols. Choosing the desired protocol determines the timing of the ACK signals sent to the peripheral device as well as the timing of the REQ signals expected from the peripheral device [41]. The handshaking protocol used for this experiment is burst mode, which provides for control of the PCLK (input/output) signal line, as well as the ACK and REQ lines. The PCLK line is a 20 MHz clock output from the DIO-32HS and is used in our system as an asynchronous sample clock for the capture device [30]. Each cycle, the DIO board applies a signal to ACK if it is available for transfer, and the peripheral device applies a signal to REQ if it is available for transfer. If both devices have indicated a transfer, a single data point is latched [41]. One of the limiting factors in the data rate is the signal clock used for handshaking. The 20 MHz PCLK output from the DIO-32HS will limit transfer rates to twenty MSPS. This transfer rate could be further degraded by a long data cable; however, for this experiment, a two foot cable was used. According to the datasheet of the DIO-32HS, for cables under one meter, the acquisition board can support transfer rates up to twenty MSPS in burst handshake mode [41]. Thus our cable is short enough to not add significant data rate limitations.

C.2 AD9054 Evaluation Board

The A/D evaluation board is built around the Analog Devices AD9054A analog to digital converter, and is listed in Table C.2 as (1). The board comes shipped with the following configuration [42]:

- DC Coupled Analog Input
- Differential Clock Input
- Internal Voltage Reference, $V_{ref} = 2.5V$

Some of these initial settings can be changed by using the jumpers on the evaluation board (Figure C.2, Table C.1); however, changing from a differential clock input to a single-ended clock input requires the following changes to the board [42]:

- Removal of the chip resistor, R11
- Insertion of a 0.1 μF ceramic capacitor, C5

The power for the board comes from a +/- 5V/3A Condor power supply (listed in Table C.2 as (7)). The evaluation board draws 300 mA at 5V and 142 mA at -5V.

C.2.1 Desired Configuration

In order to obtain the desired mode of operation, the evaluation board was changed from its initial configuration. The first problem was a large DC offset when initially installed at the PARI site. It was determined this was due to the building ground and the antenna ground floating with respect to each other, and thus AC coupling was considered as an alternative. It is known that this will affect the low frequency performance of the receiver; however, it was determined that the low cutoff frequency, somewhere below 1 MHz, was below the lowest frequency of interest, 3 MHz.. AC coupling was then determined to be acceptable. Configuration of the board in this mode required only a change in jumper settings, shown in Table C.1 below. The evaluation board makes use of a reference voltage which can be either internally or externally generated. An external V_{ref} (up to 2.5 +/- 0.25 V) can be input to the circuit board via the power connector [42]. An external V_{ref} provides the designer with better accuracy and an increased analog input range (1.024 +/- 10% V_{pp}). The internal V_{ref} is set to 2.5 V and can supply up to several mA to additional loads [42]. Without the need for additional accuracy in the reference voltage or the ability to drive multiple loads, the internal reference voltage option was chosen. Setting the evaluation board in this mode of operation requires jumper S102.

There are two modes of operation for applying a clock signal to the evaluation board. These depend on the polarity of the clock signal, and are referred to as single ended or differential ENCODE input. Use in differential input mode requires a positive clock signal on the ENC connector to the board and its complement clock signal on the $\overline{ENC}$ connector. For this experiment, we used a single ended ENCODE input, and thus only the ENC connector was used.

The evaluation board provides for the ability to operate in 'Single Port' or 'Dual Port' data output modes. When operating in single port mode, the ADC produces a sample on each clock edge, and the sample is available on the output pins after four clock cycles. In this mode, 100 MSPS is the recommended maximum data conversion rate. When operating in dual port mode, as was chosen for this experiment, the ADC produces a sample on each clock

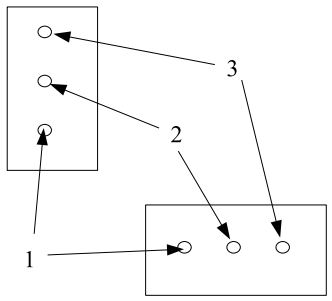

Figure C.2: Jumper Pin Designations

Table C.1: Jumper settings used for AD9054 Evaluation Board, *Pins:* indicates the pins which are to be jumpered together.

Jumper	**Use**	**Pins**	**Effect**
S101	AC/DC Coupling	2,3	AC Coupling
S102	Voltage Reference	2,3	Internal V_{ref}
S103	AC/DC Coupling	2,3	AC Coupling
S104	Data Output Mode	2,3	Dual - Channel
S105	Invert Latch Clocks	2,3	
S106	Data Output Mode	2,3	Dual - Channel
S107	Data Output Mode	2,3	Dual - Channel

edge, and the samples are alternately available on buses A and B after five clock cycles. This makes the data rate at either port half the ENCODE rate. Use in dual port mode requires a synchronizing positive-going pulse on the DS pin after power up before the digital data will be valid; however, once synchronized, pulses on DS have no effect on the output data. This is convenient in that it allows automatic synchronization by pulsing DS at half the ENCODE rate. Upon synchonizing the ADC, the odd samples will be available on port A and the even samples will be available on port B or vice versa. Setting the evaluation board to operate in dual port mode requires setting jumpers S104, S106, and S107.

C.3 IDT72V295 FIFO Buffer and Altera ACEX FPGA

In order to obtain data from the A/D converter, the DIO-32HS is connected via a SCSI3 pin replicator cable (listed in Table C.2 as (4)) to the FPGA/FIFO printed circuit board. This

PCB consists of the Altera FPGA (listed as (2)), the IDT FIFO (listed as (3)), the JTAG programming connection (listed as (6)), and is connected to the AD9054 Evaluation Board using a C37 DRPF interconnect [42]. Also included on this circuit board are LED status lights, indicating when the FPGA is programmed and ready for operation. The data capture circuit board were designed and fabricated by Grant Hampson at Ohio State University [30].

C.3.1 Altera's Acex Field Programmable Gate Array

All digital logic is implemented on the 144 pin Acex FPGA. We use the ByteBlasterMV programming cable (listed as (5)) to program the FPGA. The programming cable plugs into the PC's LPT (parallel) port and connects to the JTAG connection on the FIFO/FPGA circuit board. Altera's Quartus II software was used to write the HDL code as well as load the software.

C.3.2 IDT's First-In-First-Out Data Buffer

The buffer used to hold data before transfer to the PC is a 64 pin IDT 256k x 18-bit FIFO. Two data throughput modes of operation are possible: First Word Fall Through, FWFT, and IDT Standard mode [43]. The FWFT mode causes the first data word to be available on the output pins as soon as it is written to the FIFO. This allows for cascades of buffers if more data capacity is required [43]. The IDT standard mode, used in this experiment, requires a read operation before the first word is available on the output pins [43].

Table C.2: Parts Listing for PLFM Experiment and Receiver

	Part	Manufacturer	Part Number	Use
1	AD9054 Evaluation Board	Analog Devices	AD9054A/PCB	A/D Converter
2	Acex FPGA	Altera	EP1K30TC144-3	FPGA Logic
3	FIFO	Integrated Device Technology	72V2105	Data Buffer
4	SCSI3 pin replicator cable		C68-MF24	Capture Board to PC
5	ByteBlaster MV Cable	Altera	E152747	FPGA Programming
6	JTAG Connector	Altera		FPGA Programming
7	+/- 5V 3A Power Supply	Condor	HBB55-3/OVP-A+	5V Power Supply
8	200 MHz Synthesizer	Synthesis Microwave Corp	SMC-OPL-S-200	Clock
9	PCI-DIO-32HS	National Instruments	321464A-01	PC Data Acq. Board
10	Personal Computer	Emachines	AMD Athlon 1.53 GHz	Data Capture/Storage
			128 MB RAM	
11	LabWindows/CVI	National Instruments	Ver. 7.0.0	Interface PCI-DIO-32HS
12	Quartus II Web Edition	Altera	Ver. 4.0	HDL Programming
13	MATLAB	MathWorks	Ver. 6.5 R13	Data Analysis/Reduction

Table C.3: Parts Listing for PLFM Experiment and Receiver *(cont.)*

	Part	**Manufacturer**	**Part Number**	**Use**
14	Gain Controller	Mini-Circuits	ZFAT-4816	AGC
15	High Pass Filter	Mini-Circuits	SHP-50	Anti-Aliasing Filter
16	Low Pass Filter	Mini-Circuits	SLP-50	Anti-Aliasing Filter
17	2×21 dB Amplifiers	Mini-Circuits	ZFL-2500VH	High Power Amplifier
18	Arbitrary Function Generator	Stanford Research Systems	DS345	Clock Reference Tone
19	Regulated Power Supply	Radio Shack	22-504	13.8 V Power Supply

Appendix D

Computer Code

D.1 Capture Board FPGA Software

```
-- Interface between AD9054 Prototype Board and PCI-DIO-32HS
-- Grant Hampson 18 Feb 2002
SUBDESIGN ad9054proto
(
dra, -- clock from AD9054 development board for Data bus A
drb, -- clock from AD9054 development board for Data bus B
busa[7..0], -- Data bus A from AD9054 development board
busb[7..0], -- Data bus B from AD9054 development board
fifo_full, -- fifo status lines
fifo_empty,
pclk, -- clock from PCI-DIO-32HS interface
ack, -- indicates start of transfer/transfer possible
dioa[7..0], -- data bus A from PCI-DIO32HS interface
diob[7..0] -- data bus B from PCI-DIO32HS interface
:INPUT;
adc_reset, -- reset line for AD9054 development board
fifo_data[15..0], -- data for the output 256k fifo
fifo_wen, -- FIFO controls
fifo_wclk,
fifo_mrs,
fifo_rclk,
fifo_ren,
led[5..0], -- Six status LEDs 100/200,RAW,FS/4,FFT,FILTER,FPGA
req -- tell PCI-DIO32HS that FIFO is ready
:OUTPUT;
```

```
)
VARIABLE
busa_in_reg[7..0] : DFF; -- first input registers
busb_in_reg[7..0] : DFF;
busa_syncreg[7..0] : DFF; -- synchronisation register
busa_reg[7..0] : DFF; -- data is synchronised now
busb_reg[7..0] : DFF;
BEGIN
--
-- Write to FIFO with 100MHz input
--
busa_in_reg[].clk = !dra; -- Both buses directly into registers
busa_in_reg[7..0].d = busa[0..7];
busb_in_reg[].clk = !drb;
busb_in_reg[7..0].d = busb[0..7];
busa_syncreg[].clk = !dra; -- dra 100MHz clock arrives first
9
busa_syncreg[].d = busa_in_reg[].q;
busa_reg[].clk = !drb; -- same clock since data is synchronised now
busb_reg[].clk = !drb;
busa_reg[].d = busa_syncreg[].q;
busb_reg[].d = busb_in_reg[].q;
--
-- ADC controls
--
adc_reset = GND;
--
-- FIFO controls
--
fifo_data[15..8] = busa_reg[].q; -- First sample is high byte
fifo_data[7..0] = busb_reg[].q; -- Second sample is low byte
fifo_wen = GND; -- always writing to PC
fifo_wclk = drb;
req = VCC; -- ask to transmit to PC
fifo_mrs = diob[0]; -- PC can reset the FIFO before reading
fifo_rclk = pclk; -- PC clock (20MHz)
fifo_ren = !ack; -- stops FIFO read when PC stops reading
--
-- status leds
--
led[5..0] = VCC; -- nothing to monitor
END;
```

D.2 Capture Time Series Software

```
/* Third Revision PARI Field Code
captures just time series data
and stores to file
October 6, 2004 */

//includes
#include <utility.h>
#include <analysis.h>
#include <dataacq.h>
#include <formatio.h>
#include <ansi_c.h>

//macro defines
#define FS 200
#define SAMPLES 16384
#define TINY (1e-20)
#define TRUE 1
#define FALSE 0
#define NO_WAIT 0
#define PCI_DIO_32HS 1
#define NULL_PLOT_HANDLE -1

// globals
static double xreal[SAMPLES];
static short iBuf[SAMPLES];

//setup ad9054 eval board
void setup_ad9054()
{
short iBoardType;

Init_DA_Brds (PCI_DIO_32HS,&iBoardType); // set up the PCI-DIO-32HS board

DIG_Grp_Config(PCI_DIO_32HS,1,2,2,0); // group1:16-bit,ports C&D, input

DIG_Grp_Mode(PCI_DIO_32HS,1,3,0,0,0,0); /* group1:burst handshake
  REQ ACK active high
  100ns PCLK */

DIG_Block_PG_Config(PCI_DIO_32HS,1,0,1,1,25,0); // disable pat gen

DIG_Line_Config(PCI_DIO_32HS,1,0,1); // port B bit-0 is an output: LED1 on board

} /* void setup_ad9054() */

// get system time
void GetDateTime(char *acDateTime)
{
int iMo, iDy, iYr, iHr, iMi, iSe;
GetSystemDate (&iMo, &iDy, &iYr);
GetSystemTime (&iHr, &iMi, &iSe);
sprintf(acDateTime, "%02d%02d%02d_%02d%02d%02d", iYr-2000,iMo,iDy,iHr,iMi,iSe);
return;
} /* void GetDateTime() */

// get data samples for one window
void get_raw_data(int inte)
{
int i;
int numsamples=16384;
char rawsample, acFilename[256], acDTG[256];
char testfile[256];
FILE *filepntr;
long nRemaining;
double *real_ptr, *imag_ptr;
short *short_ptr;

DIG_Out_Line (PCI_DIO_32HS, 1, 0, 0); // resets FIFO
Delay(0.001);
DIG_Out_Line (PCI_DIO_32HS, 1, 0, 1);   // starts capturing data

GetDateTime(acDTG);

DIG_Block_In (PCI_DIO_32HS, 1, iBuf, (numsamples/2)+2); // reads in 1 block = 16 bits
nRemaining=1;
while(nRemaining>0) DIG_Block_Check (PCI_DIO_32HS, 1, &nRemaining);

real_ptr=&xreal[0];
short_ptr=&iBuf[2];  // skip the first two samples of the FIFO

for (i=0; i<numsamples/2; i++)
{
rawsample = ((*short_ptr) >> 8) - 127;  // signed binary -> result is digital amplitude
```

```
*real_ptr++=(double)rawsample;
rawsample=((*short_ptr++) & 0x00FF) - 127; // mask to rearrange word
*real_ptr++=(double)rawsample;
}  /* for (i=0;i<numsamples/2;i++) */

sprintf(acFilename,"raw_data\\%s_%d.dat",acDTG,(int)inte);
ArrayToFile (acFilename, xreal, VAL_DOUBLE,numsamples,
1,VAL_GROUPS_TOGETHER,VAL_GROUPS_AS_COLUMNS,VAL_CONST_WIDTH,10,
VAL_BINARY,VAL_TRUNCATE);

return;

} /* void get_raw_data() */


void main(void)
{
int numsamples=16384, i, numint=1;
long int num_files=0;
char sampstring[100], acFilename[256], acDTG[256], stat[256];
int iControlID, bRun=TRUE;
FILE *filepntr;

setup_ad9054();

//main control program
while (bRun)
{

num_files++;

if (num_files>5000) num_files=0;

get_raw_data(num_files);

} /* if (bRun) */

Delay(0.1);  // 'stop PC polling so hard'

}  /* void main(void) */
```

D.3 Capture Spectra Software

```
/* Third Revision PARI Field Code
   Derek Wilson October 6, 2004
   revised from Grant Hampson's
   'PCI-DIO-32HS interface to Proc8 board'
   code from 5 December 2001 */

//includes
#include <utility.h>
#include <analysis.h>
#include <dataacq.h>
#include <formatio.h>
#include <ansi_c.h>
#include <userint.h>

#include "eval_board.h"

//macro defines
#define FS 200
#define SAMPLES 16384
#define TINY (1e-20)
#define TRUE 1
#define FALSE 0
#define NO_WAIT 0
#define PCI_DIO_32HS 1
#define NULL_PLOT_HANDLE -1
#define maxclips 1638  // 10% of samples
#define minclips 14747 // 90% of samples + 1
#define mincwindows 5
#define maxcwindows 5

// globals
static double xreal[SAMPLES];
static double ximag[SAMPLES];
static double power_intg[SAMPLES];
static short iBuf[SAMPLES];
static int portNumber=0x378;
//static int clippedwindow;
//static int unclippedwindow;
//static int curlevel;
```

```
//LabWindows/CVI GUI stuff
static int hpMain;

//setup ad9054 eval board
void setup_ad9054()
{
short iBoardType;

Init_DA_Brds (PCI_DIO_32HS,&iBoardType); // set up the PCI-DIO-32HS board

DIG_Grp_Config(PCI_DIO_32HS,1,2,2,0); // group1:16-bit,ports C&D, input

DIG_Grp_Mode(PCI_DIO_32HS,1,3,0,0,0,0); /* group1:burst handshake
  REQ ACK active high
  100ns PCLK */

DIG_Block_PG_Config(PCI_DIO_32HS,1,0,1,1,25,0); // disable pat gen

DIG_Line_Config(PCI_DIO_32HS,1,0,1); // port B bit-0 is an output: LED1 on board

} /* void setup_ad9054() */

// get system time
void GetDateTime(char *acDateTime)
{
int iMo, iDy, iYr, iHr, iMi, iSe;
GetSystemDate (&iMo, &iDy, &iYr);
GetSystemTime (&iHr, &iMi, &iSe);
sprintf(acDateTime, "%02d%02d%02d_%02d%02d%02d", iYr-2000,iMo,iDy,iHr,iMi,iSe);
return;
} /* void GetDateTime() */

void GainControl(int *currentlevel,int whichway)
{
if (whichway==0) *currentlevel=*currentlevel-1;
if (whichway==1) *currentlevel=*currentlevel+1;

if (*currentlevel<0) *currentlevel=0;
if (*currentlevel>7) *currentlevel=7;

outp(portNumber, (char) *currentlevel);
}


// get data samples for one window
void get_raw_data(int numsamples, int inte, int integrate, int wtfr,int *cw, int *ucw, int *cl)
{
long int clips=0, noclips=0;
int i;
char rawsample, acFilename[256], acDTG[256];
char testfile[256];
FILE *filepntr;
long nRemaining;
double *real_ptr, *imag_ptr;
short *short_ptr;
double t0,t1;

DIG_Out_Line (PCI_DIO_32HS, 1, 0, 0); // resets FIFO
Delay(0.001);
DIG_Out_Line (PCI_DIO_32HS, 1, 0, 1);   // starts capturing data

GetDateTime(acDTG);

DIG_Block_In (PCI_DIO_32HS, 1, iBuf, (numsamples/2)+2); // reads in 1 block = 16 bits
nRemaining=1;
while(nRemaining>0) DIG_Block_Check (PCI_DIO_32HS, 1, &nRemaining);

real_ptr=&xreal[0];
short_ptr=&iBuf[2];  // skip the first two samples of the FIFO

for (i=0; i<numsamples/2; i++)
{
rawsample = ((*short_ptr) >> 8) - 127;  // unsigned binary -> result is digital amplitude
*real_ptr++=(double)rawsample;
rawsample=((*short_ptr++) & 0x00FF) - 127; // mask to rearrange word
*real_ptr++=(double)rawsample;
}  /* for (i=0;i<numsamples/2;i++) */

if (inte==integrate) // if this is the last window of data to be acquired, plot raw data
{
  DeleteGraphPlot(hpMain, MAIN_GRAPH_RAW, NULL_PLOT_HANDLE,
  VAL_IMMEDIATE_DRAW);
PlotWaveform(hpMain, MAIN_GRAPH_RAW, xreal, numsamples,
 VAL_DOUBLE,1.0, 0.0, 0.0, 1, VAL_THIN_LINE,
 VAL_NO_POINT, VAL_SOLID, 1, VAL_BLUE);
```

```
} /* if (inte==integrate) */

for (i=0; i<numsamples; i++)
{
if (abs(xreal[i])>75) clips++;
if (abs(xreal[i])<75) noclips++;
}

if (noclips>minclips) (*ucw)++;

if (*ucw>mincwindows & *cl>0)
{
GainControl(cl,0); // 0 if attenuation needs to decrease (gain needs to increase)
*ucw=0;
}

if (clips>maxclips) (*cw)++;

if (*cw>maxcwindows & *cl<7)
{
GainControl(cl,1); // 1 if attenuation needs to increase (gain needs to decrease)
*cw=0;
}

if (wtfr==TRUE) // write to file
{
sprintf(acFilename,"raw_data\\%d_%s_%d.dat",*cl,acDTG,(int)inte);
ArrayToFile (acFilename, xreal, VAL_DOUBLE,numsamples,
1,VAL_GROUPS_TOGETHER,VAL_GROUPS_AS_COLUMNS,VAL_CONST_WIDTH,
10,VAL_BINARY,VAL_TRUNCATE);
} /* if (wtf) */
} /* void get_raw_data() */

// do fft and compute integration power
void do_raw_fft(int numsamples, double inte, double integrate, int wtff,
int wtfi, int *cl)
{
int i;
char acFilename[256],acDTG[256];
FILE *filepntr;
double real, imag, abspower;
double startfreq=0.0;
double stepfreq=FS/((double)numsamples);
double t0,t1;

GetDateTime(acDTG);

// SetCtrlVal(hpMain,MAIN_STATUS,"Computing FFT");

TriWin(xreal, numsamples); // always use triangular window on data

// t0=Timer();
ReFFT(xreal, ximag, numsamples);  // fft: xreal is input and output real, ximag is output imag
// t1=Timer();
// SetCtrlVal(hpMain,MAIN_TTP,(t1-t0)*1000);

// compute power in fft sample by sample
for (i=0;i<numsamples;i++)
{
real=xreal[i];
imag=ximag[i];
abspower=(real*real+imag*imag) /
 (((double)numsamples)*((double)numsamples));
xreal[i]=10.0*log10(abspower+TINY);

power_intg[i] = power_intg[i] + abspower; // compute integration
} /* for (i=0;i<numsamples;i++) */

DeleteGraphPlot(hpMain, MAIN_GRAPH_INST, NULL_PLOT_HANDLE,
VAL_IMMEDIATE_DRAW);
PlotWaveform (hpMain, MAIN_GRAPH_INST, xreal, numsamples, VAL_DOUBLE,
1.0, 0.0, startfreq, stepfreq, VAL_THIN_LINE, VAL_NO_POINT,
VAL_SOLID, 1, VAL_RED);

// SetCtrlVal(hpMain,MAIN_STATUS," ");

if (wtff==TRUE) // write instantaneous spectrum to file
{
// SetCtrlVal(hpMain,MAIN_STATUS,"Writing Instantaneous Spectrum");
//sprintf(acFilename,"raw_data\\%s.dat",acDTG);
//filepntr=fopen(acFilename,"w");
//for (i=1; i<numsamples; i++)
// fprintf(filepntr,"%f\n",xreal[i]);
//fclose(filepntr);
sprintf(acFilename,"fft_data\\%d_%s_%d.dat",*cl,acDTG,(int)inte);
ArrayToFile (acFilename, xreal, VAL_DOUBLE,numsamples,
1,VAL_GROUPS_TOGETHER,VAL_GROUPS_AS_COLUMNS,VAL_CONST_WIDTH,
```

```
10,VAL_BINARY,VAL_TRUNCATE);
// SetCtrlVal(hpMain,MAIN_STATUS," ");
} /* if (wtff==TRUE) */

if (inte==integrate) //if this is the last integration, wtf and plot
{
for (i=0;i<numsamples;i++)
{
power_intg[i]=power_intg[i]/integrate;
power_intg[i]=10.0*log10(power_intg[i]+TINY);
} /* for (i=0;i<numsamples;i++) */

DeleteGraphPlot(hpMain, MAIN_GRAPH_FFT, NULL_PLOT_HANDLE,
VAL_IMMEDIATE_DRAW);
PlotWaveform (hpMain, MAIN_GRAPH_FFT, power_intg, numsamples,
VAL_DOUBLE,1.0, 0.0, startfreq, stepfreq, VAL_THIN_LINE,
VAL_NO_POINT, VAL_SOLID, 1, VAL_BLUE);

if (wtfi==TRUE)
{
// SetCtrlVal(hpMain,MAIN_STATUS,"Writing Integrated Spectrum");
//sprintf(acFilename,"int_data\\%s.dat",acDTG);
//filepntr=fopen(acFilename,"w");
//for (i=1; i<numsamples; i++)
// fprintf(filepntr,"%f\n",power_intg[i]);
//fclose(filepntr);
sprintf(acFilename,"int_data\\%d_%s_%d.dat",*cl,acDTG,(int)inte);
ArrayToFile (acFilename, power_intg, VAL_DOUBLE,numsamples,
1,VAL_GROUPS_TOGETHER,VAL_GROUPS_AS_COLUMNS,VAL_CONST_WIDTH,
10,VAL_BINARY,VAL_TRUNCATE);
// SetCtrlVal(hpMain,MAIN_STATUS," ");
} /* if (wtfi==TRUE) */
} /* if (inte==integrate) */

} /* void do_raw_fft() */

void main(void)
{
int ns, numsamples, i, numint, wtfr,wtff,wtfi,do_one;
int clippedwindow=0, unclippedwindow=0, curlevel=0;
int *cw=&clippedwindow, *ucw=&unclippedwindow, *cl=&curlevel;
long int num_files=0;
char sampstring[100], acFilename[256], acDTG[256], stat[256];
int iControlID, hHandle, bQuit=FALSE, bRun=FALSE, bReset=FALSE;
FILE *filepntr;
double startfreq=0.0;
double stepfreq=FS/((double)numsamples);
double t2,t3;

// LabWindows GUI stuff
hpMain=LoadPanel(0, "eval_board.uir", MAIN);
DisplayPanel(hpMain);
setup_ad9054();
outp(portNumber, (char) 0);

// gets current control values and does main control program
while (GetUserEvent(NO_WAIT, &hHandle, &iControlID) || !bQuit)
{
if (hHandle==MAIN)
{
GetCtrlVal(hpMain, MAIN_WRITETOFILE_RAW, &wtfr); // write raw data?

GetCtrlVal(hpMain, MAIN_WRITETOFILE_FFT, &wtff); // write inst. spectrum?

GetCtrlVal(hpMain, MAIN_WRITETOFILE_INT, &wtfi); // write integrated spectrum?

GetCtrlVal(hpMain, MAIN_NUMBERSAMPLES, &ns); // number of samples per acquisition?
numsamples=(int)pow(2,ns);

GetCtrlVal(hpMain, MAIN_INTEGRATIONS, sampstring); // number of integrations?
numint=atoi(sampstring);


switch (iControlID)
{
case MAIN_QUIT:
 bQuit=TRUE;
   break;

case MAIN_GET_DATA:
  GetCtrlVal(hpMain,MAIN_GET_DATA, &bRun);
  break;

case MAIN_RESET:
 bReset=TRUE;
 break;
```

```
} // switch
} //if (hhandle==MAIN)

//if reset is pressed, delete old files
if (bReset)
{
SetCtrlVal(hpMain,MAIN_STATUS,"Resetting...");
SetCtrlVal(hpMain,MAIN_TTA,0.0);
SetCtrlVal(hpMain,MAIN_TTP,0.0);
SetCtrlVal(hpMain,MAIN_TTI,0.0);

bRun=FALSE;
SetCtrlVal(hpMain,MAIN_GET_DATA,bRun);
bReset=FALSE;
sprintf(acFilename,"raw_data\\*.*");  DeleteFile(acFilename);
sprintf(acFilename,"int_data\\*.*");  DeleteFile(acFilename);
sprintf(acFilename,"fft_data\\*.*");  DeleteFile(acFilename);

num_files=0;
clippedwindow=0;
unclippedwindow=0;
curlevel=0;

SetCtrlVal(hpMain,MAIN_STATUS," ");

}

//main control program
if (bRun)
{

for (i=0; i<numsamples;i++) power_intg[i]=0.0; //set initial power of this integration to zero

// do integration
t2=Timer();

num_files++;

//sprintf(stat,"Running...%d",num_files);
//SetCtrlVal(hpMain,MAIN_STATUS,stat);

for (i=1;i<=numint; i++)
{
get_raw_data(numsamples,i,numint,wtfr,cw,ucw,cl);

do_raw_fft(numsamples,i,numint,wtff,wtfi,cl);

} /* for (i=1;i<=numint; i++) */
t3=Timer();

sprintf(stat,"cw=%d, ucw=%d, cl=%d",*cw,*ucw,*cl);
SetCtrlVal(hpMain,MAIN_STATUS,stat);

SetCtrlVal(hpMain,MAIN_TTI,(t3-t2));

} /* if (bRun) */

//SetCtrlVal(hpMain,MAIN_STATUS," ");


Delay(0.1);  // 'stop PC polling so hard'

} /* while GetUserEvent */

}  /* void main(void) */
```

D.4 Data Analysis Software

```
% function sp_mat=post_processing(intmat,sigma,sigma2)

sigma=9;sigma2=6;

% data post processing script
%
% function sp_mat=post_processing(intmat,sigma,sigma2,mab)
%
% 1.) performs deep integration to determine
%     estimate of total power in a spectrum
%
% 2.) excises RFI which is 'sigma' standard deviations
%     above mean of each spectrum
%
```

```
% 3.) obtains an estimate of the baseline based on
%     spectra which has been excised of RFI once
%
% 4.) excises RFI which is 'sigma2' standard deviations
%     above baseline
%
% 5.) obtains a better estimate of the baseline based on
%     spectra which has been excised of RFI twice
%
% 6.) performs normalization of each spectrum based on
%     total power obtained in part 1
%
% 7.) removes baseline from each spectrum
%
% the script runs on a matrix, named 'intmat', whose rows
% are consecutive spectra and columns are frequency bins
%
% the script creates a matrix which has rows of spectra
% which are clean of any RFI (which is not too complex)
% and contain no instrumentation artifacts (i.e. greatly
% varying mean due to FFT or baseline ripple due to
% reflections inside the receiver)

%close all

%disp(sprintf('\n*****************************************'))

% figure;fig1=gcf;
% figure;fig2=gcf;
% figure;fig3=gcf;
% figure;fig4=gcf;
mait=1;
mab=25;
[NF,NS]=size(intmat);
f=37:18/NS:55-18/NS;
sp_mat=intmat; %sp_mat is output matrix
%sigma=6; %1st excision threshold
%sigma2=2; %2nd excision threshold
%mab=25; %number of elements to take at a time to perform moving avg

%disp('Performing deep integration 1...')
di1=sum(sp_mat(:,:)./NF);
di=di1;
% figure;plot(f,10.*log10(di));
% figure(fig1);plot(f,10.*log10(di));drawnow

%disp('Performing 1st RFI excision...')
[sp_mat,ind,pct_blanked]=rfi_removal(sp_mat,sigma);
disp(sprintf('%2.2f percent bins blanked',pct_blanked*100))

%disp('Performing deep integration 2...')
di2=sum(sp_mat(:,:)./NF);
di=di2;
% figure;plot(f,10.*log10(di));
% figure(fig2);hold on;plot(f,10.*log10(deepint),'g');drawnow

%disp('Obtaining baseline estimate...')
[sp_mat,bl_est]=baseline_est_and_removal(sp_mat,di,mab,mait,0);
% figure(fig2);hold on;plot(f,10.*log10(bl_est),'g');

%disp('Performing 2nd RFI excision...')
[sp_mat,ind2,pct_blanked]=rfi_removal(sp_mat,sigma2);
disp(sprintf('%2.2f percent bins blanked',pct_blanked*100))

%disp('Performing deep integration 3...')
di3=sum(sp_mat(:,:)./NF);
di=di3;
int_tot_power=sum(di);
% figure;plot(f,10.*log10(di));
% figure(fig3);hold on;plot(f,10.*log10(deepint),'c');drawnow

%disp('Performing deep integration 4...')
%di4=sum(sp_mat(:,:)./NF);
%di=di4;
% figure;plot(f,10.*log10(di));
% figure(fig1);hold on;plot(f,10.*log10(deepint),'r');drawnow

%disp('Obtaining baseline estimate and removing...')
[sp_mat,bl_est]=baseline_est_and_removal(sp_mat,di,mab,mait,1);
% figure(fig4);hold on;plot(f,10.*log10(bl_est),'k')

%disp('Normalizing spectrum powers...')
sp_mat=normalize_spectra(sp_mat,int_tot_power); %uncomment before dedispersing

%disp('Performing deep integration 5...')
di5=sum(sp_mat(:,:)./NF);
di=di5;
```

```
% figure;plot(f,10.*log10(di));
% figure(fig1);hold on;plot(f,10.*log10(deepint),'k');drawnow

% figure(fig1);hold on;plot(f(ind),10.*log10(deepint(ind)),'kx',f(ind2),10.*log10(deepint(ind2)),'ko')
% figure(fig3);imagesc(f,1:NF,10.*log10(sp_mat));caxis([-90.5 -87.5]);set(gca,'YDir','normal')



function [out_mat,b_estimate]=baseline_est_and_removal(in_mat,integrated_deeply,mab,iterations,remove)
%this function estimates and removes the baseline

[NF,NS]=size(in_mat);
out_mat=in_mat;

b_estimate=integrated_deeply;
for k=1:iterations
    b_estimate=mov_avg(b_estimate,mab);
end

if remove==1
for nf=1:NF
    mn=mean(in_mat(nf,:));
    out_mat(nf,:)=1./b_estimate.*in_mat(nf,:);
    out_mat(nf,:)=mn/mean(out_mat(nf,:)).*out_mat(nf,:);
end
end



function [out_mat,indeces,pct_blanked]=rfi_removal(in_mat,sigma)
%this function performs RFI mitigation
%it simply steps through each file in the input matrix and
%sets to the mean each bin greater than some sigma above

[NF,NS]=size(in_mat);
out_mat=in_mat;

pct_blanked=0;
for nf=1:NF
    mn=mean(in_mat(nf,80:140));
    sd=std(in_mat(nf,80:140));

    indeces=find(in_mat(nf,:)>sigma*sd+mn);
    out_mat(nf,indeces)=mn;
    pct_blanked=pct_blanked+length(indeces)/NS;
end

pct_blanked=pct_blanked./NF;



function [ts]=dedisperse_spectral_mat(sp_mat,sp_times,DM)

%function [ts,dm_check]=dedisperse_spectral_mat(sp_mat,sp_times,DM)
%ts=dedispersed time vector
%sp_mat=matrix of spectra: each row is a spectrum
%sp_times=vector of times for each spectrum (length = # of rows in sp_mat)
%DM=dispersion measure to check

[NF,NS]=size(sp_mat);
FS=200e6;
ns=16384;
f0=55e6;
f1=37e6;
alpha_d=2.41e-16;
tf=0.1;
%f0_index=ceil(f0/(FS/2)*ns/2);
%f1_index=floor(f1/(FS/2)*ns/2);
f0_index=1;
f1_index=NS;
file_0=1;
file_end=NF;
freq_vector=f1:(f0-f1)/NS:f0-(f0-f1)/NS; %in Hz
df=(freq_vector(NS)-freq_vector(1)+1)/NS;

%disp('Getting file times...')
%sp_times=sp_times-sp_times(1);
currenttime=sp_times;
%disp('Running for requested DMs...')

dm=DM;
delta_t=dm/alpha_d*(1/(f1^2)-1/(f0^2));

%time resolution given by Cordes and McLaughlin, "Searches for Fast Radio Transients"
% tau_d=10.^(-3.72+0.422*log10(DM)+0.937*(log10(DM))^2-4.4*log10(0.046));
%broadening due to multipath scattering, empirical fit by Cordes
%and Lazio (2002) (in microseconds)
```

```
% dt_DMmin=sqrt(8.3*DM*0.046^(-3)); %in microseconds
%(.046=46 MHz in GHz is center observing frequency)
% dt_o=sqrt(2*dt_DMmin^2+tau_d^2); % optimal time resolution
%   for dedispersed time series
% dt=dt_o./1e6; %dt in seconds

tchange=2*dm*df./((freq_vector).^3.*alpha_d);
tc(1)=tchange(1);
for k=2:length(tchange)
    tc(k)=tc(k-1)+tchange(k);
end

%time resolution I decided upon
% dt=delta_t/(NS-1);
% dt=tc(1);
% while tf<dt
%     dt=dt-tf;
% end
dt=delta_t/(ns/2);

start_time=currenttime(file_0);
last_time=currenttime(file_end);
end_time=last_time+2*tc(length(tc));
time_vec_out=start_time:dt:end_time+2*dt; %vector containing the times
% of the corresponding elements in ts
time_vec=time_vec_out-time_vec_out(1);
currenttime=currenttime-currenttime(1);
bound_vec=[start_time,start_time+dt/2:dt:end_time+2*dt];
%vector containing the threshold times (if below threshold, goes in 1
%bin of ts, if above, goes in next bin of ts, etc...)
ts=zeros(1,length(time_vec)); %dedispersed time domain vector
bv=bound_vec-bound_vec(1);
%matout=zeros(floor(length(ts)/3),NS);
for k=1:NS
%     start_index=1; %indicates place in time_vector
%     while tc(k)>=bv(start_index) %find the element in the 'ts' vector
%  whose time corresponds to the first element in 'time_vector'
%         start_index=start_index+1;
%     end %while file_times(1)>=bound_vec(start_index)
%     indeces(k)=start_index;
    ind=find(tc(k)<bv);
    indeces(k)=ind(1)+1;
end
indeces=indeces-indeces(1);

for k=1:NF
    ind=find(currenttime(k)<bv);
    s_index(k)=ind(1);
end

nf_index=0;
filecnt=0;

for nf=1:NS
    x=zeros(NF,1);

%         if rem(nf,1000)==0
%             disp(sprintf('Running file %d out of %d',nf,NF))
%         end

    filecnt=filecnt+1;

    x=sp_mat(:,nf);

    if dm>0
        ts(s_index+indeces(nf))=ts(s_index+indeces(nf))+x.';
%        if rem(nf,3)==0
%            matout(s_index+indeces(nf),nf)=x.';
%        end
    elseif dm==0 %dm=0 doesn't run properly in the above algorithm
%    because of 'time_vec=start_time:dt2:end_time' since dt2=0
        ts=zeros(1,NF);
        ts=ts+x.';
    end

end %for nf=1:NF (file_0:1:file_end)


%tsdir='C:\Documents and Settings\Derek Wilson\Desktop\Data\ded_ts';
%tsfn=sprintf('%s\\dm_%2.2f.txt',tsdir,dm);
%tsfid=fopen(tsfn,'w');
%fprintf(tsfid,'%2.4f\n',ts.*1e9);
%fclose(tsfid);



%Pulse detection algorithm
```

```
%places all detections in a matrix called 'detmat'
% clear all;
% close all;

fdir='C:\Documents and Settings\Derek Wilson\Desktop\dedisperse_ts';
flist = dir(fdir);
flist = flist(3:max(size(flist))); % trim entries '.' and '..'

NF = max(size(flist));
dm=zeros(1,NF);
detcheck=2.9:0.1:100.1;
% detcheck=2.875:0.25:10.125; %1st bin is 2.875 to 3.125 sigmas above mean
sigmastep=detcheck(2)-detcheck(1);
detmat=zeros(length(detcheck),NF);
pctdone='';
cntfiles=0;
for nf = NF:-1:1
    %disp(sprintf('File %d out of %d',nf,NF))
    filename = sprintf('%s\\%s',fdir,flist(nf).name); %file to be
    %loaded into matrix
%     fid = fopen(filename,'r'); % open file for reading
%
%     [x,Mr] = fread(fid,[1 inf],'float');
%
%     fclose(fid);
%
%     max_x(nf)=max(x);
%
    dm(nf)=str2num(flist(nf).name(4:length(flist(nf).name)-4));

    cntfiles=cntfiles+1;
%     if  cntfiles/NF>(1/47)
%         clc
%         pctdone=strcat(pctdone,'*');
%         cntfiles=0;
%         disp(pctdone)
%     end

end % nf
disp('Obtained DMs and sorted...')
disp('Obtaining detection matrix...')
%pctdone=strcat(pctdone,'\n');
% mn=mean(max_x);
% sigma=std(max_x);
dm_sorted=sort(dm);
% dm_run=dm_sorted;
for dm=dm_run(length(dm_run):-1:1)
    nf=find(dm_sorted==dm)
%     if rem(nf,100)==0
        disp(sprintf('Running dm = %.2f',dm));
%     end
    filename=sprintf('%s\\dm_%.2f.txt',fdir,dm);
%     fid=fopen(filename,'r');
%     [x,Mr]=fread(fid,[1 inf],'float');
%     fclose(fid);

    x=importdata(filename)./1e9;
    x=x.';
    xma=mov_avg_ts(x,500);
    x=x-xma;

    mn=mean(x);
    sd=std(x);

    % countdown to when it's finished - a full row of stars = 100% done
    cntfiles=cntfiles+1;
%     if  cntfiles/NF>(1/47)
%         clc
%         pctdone=strcat(pctdone,'*');
%         cntfiles=0;
%         disp(sprintf(pctdone))
%     end

    detvec=(x-mn)./sd;

    detmat(:,nf)=histc(detvec,[-inf,3:0.1:100,inf]);

end % nf


function meen=mov_avg_ts(x,pts)
%calculates moving average for dedispersed time series
B=ones(pts,1)/pts;
meen=filter(B,1,x);
%meen=meen.';
meen=[meen(floor(pts/2):length(meen)),zeros(1,floor(pts/2)-1)];
```

Bibliography

[1] J. M. Cordes and M. A. McLaughlin. Searches for Fast Radio Transients. *Astrophysical Journal*, 596:1142–1154, October 2003.

[2] M. J. Rees. A better way of searching for black-hole explosions. *Nature*, 266:333–+, March 1977.

[3] S. A. Colgate. Electromagnetic pulse from supernovae. *Astrophysical Journal*, 198:439–445, June 1975.

[4] V. V. Usov and J. I. Katz. Low frequency radio pulses from gamma-ray bursts? *Astronomy and Astrophysics*, 364:655–659, December 2000.

[5] B. M. S. Hansen and M. Lyutikov. Radio and X-ray signatures of merging neutron stars. *Monthly Notices of the Royal Astronomical Society*, 322:695–701, April 2001.

[6] T. H. Hankins, J. S. Kern, J. C. Weatherall, and J. A. Eilek. Nanosecond radio bursts from strong plasma turbulence in the Crab pulsar. *Nature*, 422:141–143, March 2003.

[7] A. Sagiv and E. Waxman. Collective Processes in Relativistic Plasma and Their Implications for Gamma-Ray Burst Afterglows. *Astrophysical Journal*, 574:861–872, August 2002.

[8] D. N. Page and S. W. Hawking. Gamma rays from primordial black holes. *Astrophysical Journal*, 206:1–7, May 1976.

[9] D. H. Staelin and E. C. Reifenstein. Pulsating radio sources near the Crab Nebula. *Science*, 162:1481–1483, 1968.

[10] I. Cognard, J. A. Shrauner, J. H. Taylor, and S. E. Thorsett. Giant Radio Pulses from a Millisecond Pulsar. *Astrophysical Journal Letters*, 457:L81+, February 1996.

[11] R. W. Romani and S. Johnston. Giant Pulses from the Millisecond Pulsar B1821-24. *Astrophysical Journal Letters*, 557:L93–L96, August 2001.

[12] S. Johnston and R. W. Romani. Giant Pulses from PSR B0540-69 in the Large Magellanic Cloud. *Astrophysical Journal Letters*, 590:L95–L98, June 2003.

[13] A. D. Kuzmin and A. A. Ershov. Giant pulses in pulsar PSR B0031-07. *Astronomy and Astrophysics*, 427:575–579, November 2004.

[14] A. A. Ershov and A. D. Kuzmin. Detection of Giant Pulses from the Pulsar PSR B1112+50. *Astronomy Letters*, 29:91–95, February 2003.

[15] W. Lewandowski, A. Wolszczan, G. Feiler, M. Konacki, and T. Sołtysiński. Arecibo Timing and Single-Pulse Observations of Eighteen Pulsars. *Astrophysical Journal*, 600:905–913, January 2004.

[16] B. C. Joshi, M. Kramer, A. G. Lyne, M. A. McLaughlin, and I. H. Stairs. Giant Pulses in Millisecond Pulsars. In *IAU Symposium*, pages 319–+, 2004.

[17] H. S. Knight, M. Bailes, R. N. Manchester, and S. M. Ord. A Search for Giant Pulses from Millisecond Pulsars. *Astrophysical Journal*, 625:951–956, June 2005.

[18] J. M. Cordes, T. J. W. Lazio, and M. A. McLaughlin. The dynamic radio sky. *New Astronomy Review*, 48:1459–1472, December 2004.

[19] V. A. Soglasnov, M. V. Popov, N. Bartel, W. Cannon, A. Y. Novikov, V. I. Kondratiev, and V. I. Altunin. Giant Pulses from PSR B1937+21 with Widths $\leq$ 15 Nanoseconds and $T_b \geq 5{\times}10^{39}$ K, the Highest Brightness Temperature Observed in the Universe. *Astrophysical Journal*, 616:439–451, November 2004.

[20] C. A. Katz, J. N. Hewitt, B. E. Corey, and C. B. Moore. A Survey for Transient Astronomical Radio Emission at 611 MHz. *Publications of the Astronomical Society of the Pacific*, 115:675–687, June 2003.

[21] R. J. Balsano. *A search for radio emission coincident with gamma-ray bursts*. PhD thesis, Princeton University, 1999.

[22] S. W. Ellingson. Introduction to special section on Mitigation of Radio Frequency Interference in Radio Astronomy. *Radio Sci.*, 5, 2005. doi:10.1029/2005RS003268.

[23] A. G. Lyne and F. Graham-Smith. *Pulsar Astronomy*. Number 31 in Cambridge Astrophysics. Cambridge University Press, second edition, 1998.

[24] J. M. Cordes. NE2001: A New Model for the Galactic Electron Density and its Fluctuations. In *ASP Conf. Ser. 317: Milky Way Surveys: The Structure and Evolution of our Galaxy*, pages 211–+, June 2004.

[25] Warren Stutzman and Gary Thiele. *Antenna Theory and Design*. John Wiley and Sons, Inc., 1998.

[26] K. P. Stewart, B. C. Hicks, P. S. Ray, P. C. Crane, N. E. Kassim, R. F. Bradley, and W. C. Erickson. LOFAR antenna development and initial observations of solar bursts. *Planetary and Space Science*, 52:1351–1355, December 2004.

[27] S. W. Ellingson. Antennas for the Next Generation of Low-Frequency Radio Telescopes. *IEEE Transactions on Antennas and Propagation*, 2005.

[28] S. W. Ellingson and T.C. Kramer. Sensitivity and Bandwidth of Low Gain Antennas Below 100 MHz. In *IEEE International Antennas and Propagation Symposium*, 2005.

[29] Mini-Circuits. *Low Power Broadband Linear Amplifiers*. www.mini-circuits.com.

[30] G. Hampson. AD9054 Prototype Evaluation. Developed at the Ohio State University, *http://esto.nasa.gov/programs/iip/*, March 2002.

[31] T. H. Hankins and B. J. Rickett. Pulsar signal processing. In *Methods in Computational Physics. Volume 14 - Radio astronomy*, pages 55–129, 1975.

[32] D. C. Backer, M. R. Dexter, A. Zepka, D. Ng, D. J. Werthimer, P. S. Ray, and R. S. Foster. A Programmable 36-MHz Digital Filter Bank for Radio Science. *Publications of the Astronomical Society of the Pacific*, 109:61–68, January 1997.

[33] M. A. McLaughlin and J. M. Cordes. Searches for Giant Pulses from Extragalactic Pulsars. *Astrophysical Journal*, 596:982–996, October 2003.

[34] P. Mészáros and M. J. Rees. Gamma-Ray Bursts as X-Ray Depth Gauges of the Universe. *Astrophysical Journal*, 591:L91–L94, July 2003.

[35] R. N. Manchester, G. B. Hobbs, A. Teoh, and M. Hobbs. The Australia Telescope National Facility Pulsar Catalogue. *Astronomical Journal*, 129:1993–2006, April 2005.

[36] V. M. Malofeev and I. F. Malov. Average pulsar spectra and their interpretation. *Astronomicheskii Zhurnal*, 57:90–106, February 1980.

[37] A. D. Kuzmin and B. Y. Losovsky. No low-frequency turn-over in the spectra of millisecond pulsars. *Astronomy and Astrophysics*, 368:230–238, March 2001.

[38] M. Kramer, K. M. Xilouris, D. R. Lorimer, O. Doroshenko, A. Jessner, R. Wielebinski, A. Wolszczan, and F. Camilo. The Characteristics of Millisecond Pulsar Emission. I. Spectra, Pulse Shapes, and the Beaming Fraction. *Astrophysical Journal*, 501:270–+, July 1998.

[39] R. N. Manchester, A. G. Lyne, N. D'Amico, M. Bailes, S. Johnston, D. R. Lorimer, P. A. Harrison, L. Nicastro, and J. F. Bell. The Parkes southern pulsar survey - I. Observing and data analysis systems and initial results. *Monthly Notices of the Royal Astronomical Society*, 279:1235–1250, April 1996.

[40] H. V. Cane. Spectra of the non-thermal radio radiation from the galactic polar regions. *Monthly Notices of the Royal Astronomical Society*, 189:465–478, November 1979.

[41] National Instruments Corporation. *AT/PCI-DIO-32HS User Manual*, 1997.

[42] Analog Devices. *8-bit, 200 MSPS A/D Converter AD9054A (Datasheet)*, d edition. www.analog.com.

[43] IDT. *3.3 Volt High Density CMOS Supersync FIFO, IDT72V295, (Datasheet)*, 1991.